Universität Rostock

Traditio et Innovatio

Multilayer graphene in the interplay with different photocatalyst architectures for the hydrogen evolution reaction

Dissertation

zur Erlangung des akademischen Grades
doctor rerum naturalium (Dr. rer. nat.)
an der Mathematisch-Naturwissenschaftlichen Fakultät
der Universität Rostock

vorgelegt von
Rafael Oliveira da Silva, geb. am 14.03.1982 in São Paulo, Brasilien
aus Rostock

Rostock, 26.02.2016

Reviewers:

1. Prof. Dr. Johannes Gerardus de Vries

Leibniz-Institut für Katalyse e.V. an der Universität Rostock

2. Prof. Dr. Joachim Wagner

Institut für Chemie, Universität Rostock

Thesis Submission: 26.02.2016
Date of Defence: 28.06.2016

Declaration

I hereby declare that the work described in this thesis entitled, "Multilayer graphene in the interplay with different photocatalyst architectures and co-catalyst for the hydrogen evolution reaction" is original work undertaken by myself to receive the doctoral degree, at Leibniz Institute for Catalysis, Rostock, Germany under the guidance of my supervisor Prof. Dr. Johannes Gerardus de Vries (Head of Department "Catalysis with Renewable resources") and Dr. Sebastian Wohlrab (Group leader "Inorganic Functional Materials"). I further declare that either wholly or in part of this thesis have been submitted for the award of any other degree or qualification in any other university, institute or college of advanced education.
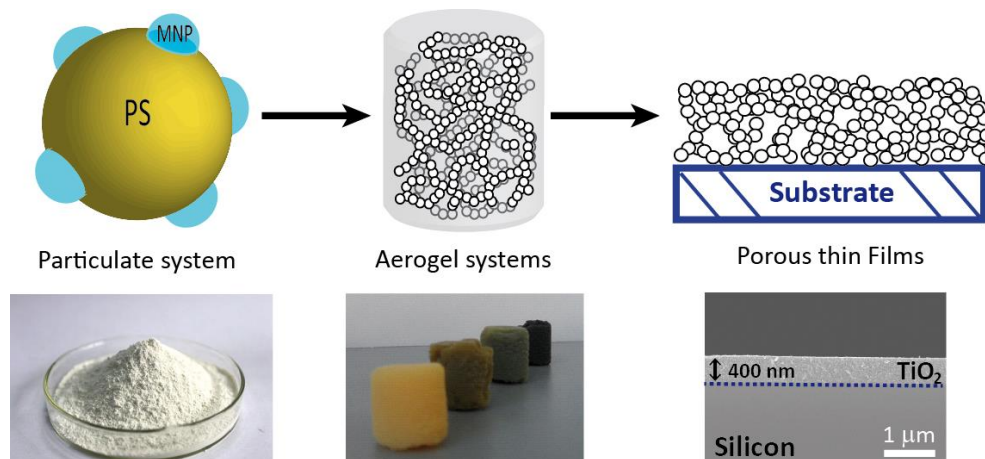
Rostock, 26.02.2016

Rafael Oliveira da Silva

"Man's mind, once stretched by a new idea, never regains its original dimensions."

<u>Oliver Wendell Holmes</u>, (1809 - 1894)

Quod scripsi, scripsi

Graphical Abstract

| Particulate system | Aerogel systems | Porous thin Films |

Abstract

Catalysis is a key technology that may enable the solar fuel generation. In particular, heterogeneous catalytic systems either employing photocatalysts or (photo)electrode materials have been developed during the last decades to achieve reductive and oxidative multi-electron reactions to convert water into H_2 (fuel) and O_2. In this work, the interplay of chemically produced graphene and its derivatives with semiconducting nanoparticles and derived architectures are investigated. As a result of its exceptional conductivity properties it is believed that graphene might enhance the separation of charge carriers, consequently increasing photocatalytic performances.

It has been revealed that catalytic properties of heterogeneous photocatalysts are strongly influenced by two geometrical parameters: size and shape. Hence, the ability to control and manipulate the nanocrystals size and shape is advantageous to tune the physical and chemical properties of photocatalysts. In this manner, it was demonstrated by comparative study on $Au/NaTaO_3$ that employing an exotemplate synthesis method for the semiconductor leads to superior photocatalytic performance in combination with graphene additives compared to materials obtained by the established solid-state reaction. This was mainly done through reducing the particle size and increasing the surface area. Additionally, *in situ* EPR spectroscopy was applied to the photosemiconductor systems together with multi-layer graphene to understand the interaction between both materials.

Moreover, inspired by the strategy developed by Niederberger based on the self-assembly and in the oriented attachment mechanism to convert preformed functionalized TiO_2 particles into a mesoporous network system it was possible to obtain aerogel co-loaded with metallic nanoparticles

and graphene as additive. These multicomponent aerogels with control over particle size, surface area and pore structure showed high photocatalytic activity. This architecture is responsible for the enhancement of the photocatalytic activity, which reached a maximum H_2 production rate of 12 mmol $H_2\ g^{-1}\ h^{-1}$ for the TiO_2 aerogel with a Pt content of 0.4 wt%. However, addition of graphene showed no significant improvement of the photocatalytiv activity since the carbon material was sterically shielded from the semiconductor and charges could not have been separated

Finally, several obtained lyogels (stage before achieving the dry aerogels) incorporated with co-catalysts and/or additives could be employed to prepare porous electrodes by spin coating. The electrocatalytic HER activities of the 1.0-Pt/TiO_2 and 1.0-Pt/TiO_2/m-rGO were tested and compared with a commercial benchmark material containing 10 wt. % Pt on carbon support. Although the produced electrodes resulted in inferior activity compared to the benchmark material, the cyclic voltammetry curves exhibited significant improvement of density current for the porous TiO_2 electrodes at overpotential of 0.2 V (vs. RHE) in combination with graphene. The Pt/TiO_2/m-rGO (m-rGO = multilayer reduced graphene oxide) exhibited nearly 3 times more active than the 1.0-Pt/TiO_2 electrode.

Kurzfassung

Katalyse könnte die Schlüsseltechnologie für die solare Treibstofferzeugung werden. Heterogene Systeme mit entsprechenden Photokatalysatoren oder Photoelektroden wurden bereits in den letzten Dekaden entwickelt, um die reduktive und oxidative Multi-Elektronenreaktionen zur Umwandlung von Wasser zu H_2 (Treibstoff) und O_2 zu ermöglichen. In dieser Arbeit wurde speziell das Zusammenspiel zwischen Graphen bzw. dessen Abkömmlingen und Halbleitern bzw. davon abgeleiteten Strukturen untersucht. Als Resultat seiner außergewöhnlichen Leitfähigkeit wird angenommen, dass Graphen die Trennung von Ladungsträgern verbessert und somit die photokatalytische Leistungsfähigkeit des Gesamtsystems.

Es ist bekannt, dass die katalytischen Eigenschaften eines heterogenen Photokatalysators deutlich von zwei geometrischen Parametern abhängen, nämlich der Größe und der Form. Kristallitgrößen und –formen zu manipulieren ist somit essentiell, um physikalische sowie chemische Eigenschaften der Photokatalysatoren zu manipulieren. Auf diese Weise wurde in einer systematischen Studie an $Au/NaTaO_3$ belegt, dass eine Exotemplat-Synthese des Halbleiters zu überlegenen photokatalytischen Eigenschaften in Kombination mit Graphen-Additiven führt im Vergleich zu konventionell, über die Festphasenreaktion hergestellten Halbleitern. Hauptsächlich kann dies auf die deutlich reduzierte Partikelgröße des Halbleiters und somit der vergrößerten Oberfläche zurückgeführt werden. Zusätzlich konnte mittels *in situ* EPR Spektroskopie die zugrunde liegenden Wechselwirkungen zwischen beiden Materialien aufgeklärt werden.

Weiterhin, inspiriert durch eine Syntheseroute von Niederberger, wurde die Selbstanordnung und orientierte Verknüpfung von vorgefertigten und funktionalisierten TiO_2 Partikeln genutzt, um mesoporöse Netzwerksysteme aufzubauen und damit Aerogele zu erzeugen. Diese können zusätzlich mit Co-Katalysatoren sowie Graphen beladen werden. Diese Multikomponenten-Aerogele, mit kontrollierter Partikelgröße, Oberfläche und Porenstruktur, zeigten hohe photokatalytische Aktivität. So konnten an einem TiO_2-Aerogel mit nur 0.4 % Pt bis zu 12 mmol H_2 g^{-1} h^{-1} erzeugt werden. Die Zugabe von Graphen zu dieser Struktur konnte jedoch die photokatalytische Aktivität nicht erhöhen, da in dieser Architektur das kohlenstoffhaltige Material sterisch vom Halbleiter abgeschirmt war und Ladungsträger nicht separiert werden konnten.

Letztlich wurden mit Additiven beladene Lyogele (Gele gefüllt mit Lösungsmittel) genutzt, um poröse Elektroden durch Spincoating herzustellen. Die elektrokatalytische Aktivität für die Wasserstofferzeugung der so hergestellten, mit 1.0 % Pt beladenen TiO_2-bzw. TiO_2/m-rGO-Filme (m-rGO = multilayer reduced graphene oxide) wurde getestet und mit einer kommerziellen Referenz verglichen (10 wt. % Pt auf Kohlenstoff). Obwohl die Leistung der so erzeugten Elektroden in vergleichbar schlechteren Aktivitäten resultierten, belegte die zyklische Voltammetrie eine signifikante

Verbesserung der Stromdichte für poröse TiO_2 -Elektroden bei einer Überspannung von 0.2 V (vs. RHE) in Kombination mit Graphen. Das Pt/TiO_2/m-rGO zeigte so bis zu 3 mal höhere Aktivitäten als 1.0-Pt/TiO_2 Elektroden.

Contents

Acknowledgments

Scientific Publications

T. Meyer∗, J.B. Priebe∗, R.O. da Silva∗, T. Peppel, H. Junge, M. Beller, A. Brückner, and S. Wohlrab, "Advanced Charge Utilization from NaTaO3 Photocatalysts by Multilayer Reduced Graphene Oxide", *Chem. Mater.* **26**, 4705–4711 (2014).
(∗ These authors contributed equally.)

R. O da Silva, F. J. Heiligtag, M. Karnahl, H. Junge, M. Niederberger, and S. Wohlrab, Design of multicomponent aerogels and their performance in photocatalytic hydrogen production. *Catal.Today* **2015,** *246*, 101-107.

R. O da Silva, S. Skruszewicz, M. Zabel, J. Tiggesbäumker, H. Junge and S. Wohlrab, co-assembly of Laser ablated nanoparticles and TiO_2 nanoparticles into multicomponent aerogels and their performance in photocatalytic hydrogen production, in preparation. 2016.

Presentations at Conferences

Oral Presentations:

1. R. O. da Silva; Multicomponent 3D Aerogels: Characterization and photocatalytic properties,
 Catalysis for Sustainable Synthesis (CaSuS), Rostock - Germany, 16 – 18, September 2013.

2. S. Skruszewicz, R. O. da Silva, R. Irsig, M. Karnahl, I. Barke, J. Tiggesbäumker, K. H. Meiwes-Broer; Efficient photocatalytic hydrogen production using metal nanoparticles created by femtosecond laser ablation, Light 2 Hydrogen Symposium "Sustainable Hydrogen and Fuels - Status and Perspectives", Rostock – Germany, 14 - 16 May 2014.

3. R. O. da Silva, M. Karhnal, F. J. Heiligtag and S. Wohlrab; Multicomponent 3D Aerogels: Characterization and their photo-catalytic properties, PREPA 11, Louvain la Neuve - Belgium, 6 -10, July 2014.

4. R. O. da Silva, M. Karnahl, S. Skruszewicz, F. J. Heiligtag, S. Wohlrab; Multicomponent aerogels (TiO_2-Rh/Pt/Ir-rGO) for enhanced photocatalytic water splitting, 6th FEZA Conference, Leipzig – Germany, 8 - 11, September 2014.

5. R. O. da Silva, F. J. Heiligtag, M. Karhnal, Henrik Junge, Markus Niederberger and S. Wohlrab; Design of Multicomponent Aerogel Catalysts and their performance in photocatalytic Hydrogen Production, 17th Norddeutsches Doktorandenkolloquium, Rostock, Germany, 11- 12, September 2014.

6. <u>R. O. da Silva</u>, F. J. Heiligtag, M. Karhnal, Henrik Junge, Markus Niederberger and S. Wohlrab; Design of Multicomponent Aerogel Catalysts and their performance in photocatalytic Hydrogen Production, XVII Workshop über die Charakterisierung von feinteiligen und porösen Festkörpern, Bad Soden / Ts., Germany, 11 – 12, November 2014

7. R. O. da Silva, S. Kreft, <u>S. Wohlrab</u>; Porous materials in photocatalytic hydrogen generation Advanced Micro- and Mesoporous Materials 2015, Burgas, Bulgarien, 06-09, September 2015.

Posters:

1. <u>R. O. da Silva</u>, M. Karhnal, S. Skruszewicz and S. Wohlrab, Enhanced hydrogen generation from multicomponent aerogels loaded with laser ablated metallic nanoparticles (Rh, Pt, Ir), 47th Jahrestreffen Deutscher Katalytiker, Weimar, Germany, March 12 – 14, 2014

2. <u>R. O. da Silva</u>, F. J. Heiligtag, M. Karhnal, Henrik Junge, Markus Niederberger and S. Wohlrab, Design of Multicomponent Aerogel Catalysts and their performance in photocatalytic Hydrogen Production, XVII Workshop über die Charakterisierung von feinteiligen und porösen Festkörpern, Bad Soden / Ts., Germany, November 11 – 12, 2014

3. <u>S. Skruszewicz</u>, R. O. da Silva, R. Irsig, M. Karnahl, <u>I. Barke</u>, J. Tiggesbäumker, K. H. Meiwes-Broer; Efficient photocatalytic hydrogen production using metal nanoparticles created by femtosecond laser ablation, Light 2 Hydrogen Symposium "Sustainable Hydrogen and Fuels - Status and Perspectives", Berlin – Germany, 2014.

List of Tables

List of Figures

List of Acronyms and abbreviations

a.u.	Arbitrary units
AM 1.5G	Air Mass 1.5 Global
AFM	Atomic Force microscopy
ATR	Attenuated Total Reflexion
BET	Brunauer-Emmet-Teller method
BJH	Barrett-Joyner-Halenda method
CB	Conduction band
CV	Cyclic Voltammetry
DMF	Dimethylformamide
DLS	Dynamic Light Scattering
ECSA	Electrochemical Surface Area
EM	Exotemplate Method
EA	Elemental Analysis
EELS	Electron Energy Loss Spectroscopy
E$_g$	Band Gap
EPR	Electron Paramagnetic Resonance
FTIR	Fourier Transform Infrared
GC	Gas Chromatography
GO	Graphene Oxide
HAADF	High-Angle Annular Dark Field
HER	Hydrogen Evolution Reaction
ICDD	International Centre for Diffraction Data
ICP	Inductively Coupled Plasma
LASIS	Laser Ablation Synthesis in Solution
MNP	Metallic Nanoparticle
m-rGO	Multilayer reduced graphene oxide
MeOH	Methanol
NC	Nanocrystal
NP	Nanoparticle
PDF	Powder Diffraction File
PEC	Photoelectrochemical
PS	Photosemiconductor
RDE	Rotating Disk Electrode
RGO	Reduced Graphene Oxide
RHE	Reference Hydrogen Electrode
SC	Semiconductor
SEM	Scanning Electron Microscopy
STH	Solar-to-hydrogen conversion
SSR	Solid-State Reaction
TCD	Thermal Conductivity Detector

TEM	Transmission Electron Microscopy
HRTEM	High-Resolution Transmission Electron Microscopy
UV-vis	Ultraviolet-visible
VB	Valence Band
wt.%	Weight percentage
XPS	X-ray Photoelectron Spectroscopy
XRD	X-ray Diffraction

Name: Rafael Oliveira da Silva
Geburtsdatum: 14.03.1982
Geburtsort: São Paulo, Brasilien
Nationalität: Brasilianisch
Geschlecht: männlich
Familienstand: ledig

Education/Bildung

2011.04 - present, Inorganic Functional Materials group at Leibniz-Institute for Catalysis at Univ. Rostock, **PhD Promotors: Prof. Johannes Gerardus de Vries and Dr. Sebastian Wohlrab**

2009.11 - 2010.11, Multifunctional Materials Lab. – Dept. of Materials at Swiss Federal Institute of Technology in Zurich (ETHZ), **Supervisor: Prof. Markus Niederberger**

2007.03 - 2008.11, Chemistry Dept. – Federal University of Sao Carlos (UFSCAR), Major: Physical-Chemistry. **Master Promotor: Prof. Emerson Rodrigues de Camargo and Prof. Edson Roberto Leite**

2003.03 - 2006.12, Chemistry Dept. – Federal University of Sao Carlos (UFSCAR), **Bachelor.**

# 1.	Introduction:

## 1.1	Scope of the work

The objective of the work was study the structure-activity relationship of new heterogeneous photocatalysts and to provide insights into the nanostructured systems which combine (i) a photosemiconductor (PS) with (ii) a co-catalyst and/or (iii) additives such as chemically synthesized graphene for photocatalytic applications. Chapters 1 and 2 introduce the work and provide important background. The investigated multicomponent photocatalysts were used for the light-driven splitting of water to yield hydrogen (H_2) as described in chapter 3 and 4. In particular, chapter 3 describes the synthesis and processing of a multicomponent particulate suspension composed of 3 distinct species, which enhanced the photocatalytic activity as a result of the interplay between the 3 components. A different approach was used in chapter 4 to convert a particulate system into a mesoporous system with control over particle size, surface area and pore structure by employing self-assembly together with a non-hydrolytic sol gel route to enhance the photocatalytic properties by mesostructuring. Furthermore, it was aimed that the controlled mesoporous structure, an aerogel, has to be extended to different compositions including the addition of additives or co-catalysts which potentially could enhance photocatalysis. In the chapter 5, several obtained lyo-gels (stage before achieving the dry aerogels) including co-catalysts and/or additives could be coated on substrates to prepare porous thin xerogel films by spin coating. The films were tested in hydrogen evolution reactions (HER) to demonstrate the effect of the co-catalyst and multilayer reduced graphene oxide as an additive. Finally, the summary and outlook of this work is presented in chapter 6.

The results demonstrated the flexibility of the processing method to obtain mesoporous monoliths or films from particles and showed the advantage of such structures compared to suspended particulate systems in catalytic hydrogen production. However, it was also found the role of graphene is rather case sensitive.

## 1.2	Energy scenario challenges

The energy that powers our lives is so essential that its access is taken for granted. A myriad of activities are done like: eating, heating or cooling down our houses or offices, while driving or being driven, access to clean water, medicine, electricity to power our appliances and so forth without thinking about it. However, the time to reflect about powering the planet and whether energy sustainability is achievable at such huge demands has already come!

As world population continues to grow and the limited amount of fossil fuels begins to decline, it may not be possible to power and fuel the planet's energy demand only by using fossil fuels. Moreover, despite the fact the world is consuming valuable and strategic resources that cannot be replaced in foreseeable time, the use and combustion of fossil fuels is associated with air quality deterioration, oil

spills, water pollution and massive release of greenhouse gases such CO_2 and NO_x, which contributes to increased global warming and consequently the rise of the sea level.[1] Figure 1.1 illustrates the growing energy demand from 1965 until 2014. In 2014 the total world energy consumption reached an astonishing 151 PWh (151×10^{15} Wh). For the mentioned period the world energy consumption rose nearly 375% in 50 years. To give a glimpse of the size of this consumption, the amount of energy consumed in 2014 is equivalent to the energy output of nearly 32000 Rostock power plants† (based on bituminous coal) or more than 5220 Fukushima's nuclear plants before the disaster‡ or simply 1720 Itaipu Dam's with a flooded area of 1350 km^2 for each dam§.

Figure 1.1(b) illustrates that the production and use of renewable resources achieved a growth of nearly 370% from 2005 to 2014, however even assuming a continuous growth, would mean that renewable energy will be responsible for only 8% of the total energy mix without considering hydro power by 2035.[2] (Hydro power was excluded because its potential growth is nearly saturated and the aforementioned report does not include hydro power in the renewable technologies.) Nowadays, nearly 86% of the world's energy consumption comes from fossil fuels, roughly divided in equal parts of oil, coal and natural gas as depicted in Figure 1.2, while nuclear power accounted for 4.4%, hydro power for 7% and renewable sources such as solar, wind, geothermal, biomass and biofuels accounted for 2.4%. Taking into account the relatively low prices and abundance of fossil fuels in comparison with the relatively high cost of renewable technologies it is highly likely that fossil fuels are going to play a major role in the energy matrix for the next decades.

The future challenges to reduce our fossil fuel dependence and mitigate CO_2 emissions require large scale and efficient methods to convert renewable raw materials into useful fuels and chemicals to achieve environmental and energetic sustainability. Therefore, pursuing renewable energy sources is of utmost importance to replace fossil fuels which should be saved for more sophisticated applications such as for fine chemicals (polymers and pharmaceuticals) which have their basis in smaller and simpler organic molecules derived from petroleum. In this respect, one possible and promising strategy is to efficiently obtain light-driven splitting of water to generate hydrogen and oxygen for harvesting and storing the sunlight energy into chemical bonds. So, water could be used to replace fossil fuels as the primary resource of hydrogen with the advantages of being clean, abundant and renewable, besides to not contribute with greenhouse gases emissions. In contrast to available resources such as fossil fuels, hydrogen has to be produced, making it an energy carrier and not a proper fuel.

---

† Kraftwerks und Netzgesellschaft mbH (KNG) annual power generation (2014): 4.84 TWh.
‡ Fukushima Daiichi annual power generation (2011): 28.89 TWh.
§ Itaipu Binacional annual power generation (2014): 87.8 TWh.
Power generation values were obtained from the official websites: KNG, Tepco and Itaipu Binacional, respectively.
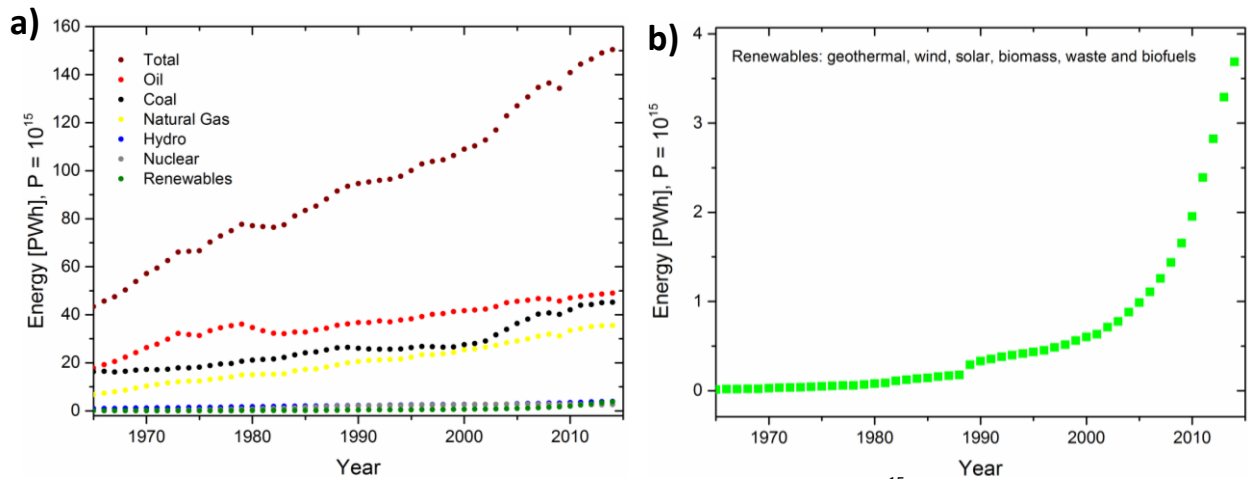
Figure 1.1 (a) World energy primary consumption from 1965 to 2014 in (1x10^{15} Watt-hours). (b) World energy renewable energy consumption evolution from 1965 to 2014. Renewable energy here refers to geothermal, wind, solar, biomass, waste and biofuels. Biofuels started to count from 1989.[3]
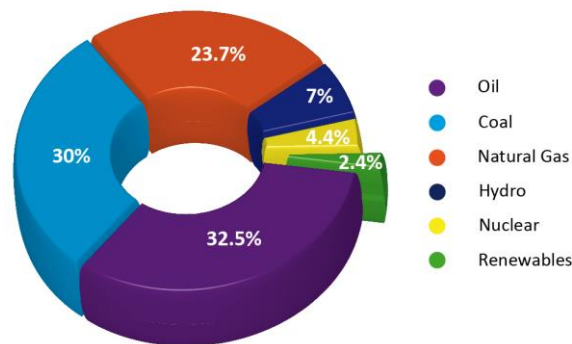
Figure 1.2 World energy consumption in 2014, after compilation from BP Statistical Review of World Energy and International Energy Agency (IEA) Key World Energy Statistics. [3] Petawatt-hour (PWh) = 1 x 10^{15} Wh.

There are a number of ways to achieve solar hydrogen production such as: (i) the well-established water electrolysis using renewable power sources such as solar cells, wind turbines, geothermal or hydraulic power; (ii) reforming of biomass and (iii) artificial photosynthesis which can be divided into photocatalytic particulate[**] process or by photoelectrochemical (PEC) water splitting.

The atmosphere of earth is mainly composed of nitrogen gas (78%), oxygen (21%), argon (0.93%), and carbon dioxide (0.04%) and traces of several other gases. Plants and some bacteria release oxygen through a process called photosynthesis.[4] Photosynthesis is a relatively low efficient method of converting solar energy into chemical energy[††] in the form of sugars (glucose, fructose, etc.) according to the reaction in equation 1.1.[5] Therefore, photosynthesis is the process whereby green plants produce fuel to supply themselves.

[**] System composed only by powder material that can be suspended in a liquid solution.

[††] Photosynthesis is about one order of magnitude lower than existing solar-photovoltaic and solar thermal technologies.

$$6\,CO_2 \; + \; 12\,H_2O \quad \xrightarrow{\text{sunlight}} \quad C_6H_{12}O_6 \; + \; 6\,O_2 \; + \; 6\,H_2O \tag{1.1}$$
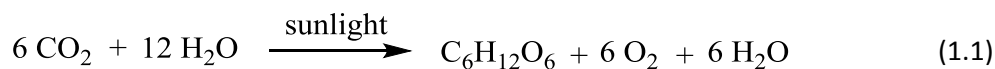
In this context, understanding how nature is able to convert sunlight to drive the synthesis of sophisticated molecules to store chemical energy may help researchers to develop bioinspired photocatalysts. Thus, one of the most exciting options is the solar hydrogen concept better known as artificial photosynthesis, where molecular hydrogen and oxygen can be produced by harvesting the sunlight and converting water to fuel, as can be summarized by (Eq. 1.2).[6] Molecular hydrogen (H_2) represents stored energy in the form of H-H chemical bonds and is being considered as a clean energy carrier because when combined with oxygen, the stored chemical energy can be released generating water as the reaction product. Additionally, hydrogen can be easily converted into electricity by the aid of fuel cells without releasing harmful byproducts to the environment.[7] Artificial photosynthesis may be an efficient solution for alleviating the adverse effects of burning fossil fuels and the rising CO_2 levels in the atmosphere.[1] Our living planet is already covered with photosynthetic units that have served us well as producers of food and fuel. Accordingly, making artificial systems that can mimic natural photosynthesis in a more sustainable and efficient way is a fascinating scientific challenge.[5]

1.3 Fuels and chemicals from renewable hydrogen

Artificial photosynthesis is a method to convert raw materials such as water and CO_2 into fuels like hydrogen (H_2), carbon monoxide (CO) and hydrocarbons[‡‡] by utilizing the power of sunlight in combination with a photocatalyst.[6e] The energy provided by UV-vis light is typical in the range of 1 - 4 eV or $100 - 300$ kJ/mol, which suffices to provide the minimum energy requirements for the water splitting reaction (Eq. 1.2), (2.46 eV or 237 kJ/mol).[8] The advantage of producing hydrogen as fuel is its high energy density which can in principle be stored and used in transportation and electricity generation using fuel cells, internal combustion engines or turbines, releasing water as a main by-product.

$$2H_2O \; + \; \text{sunlight} \quad \xrightarrow{\text{[photocatalyst]}} \quad 2H_2 \; + \; O_2 \qquad \Delta G = 237 \text{ kJ/mol} \tag{1.2}$$
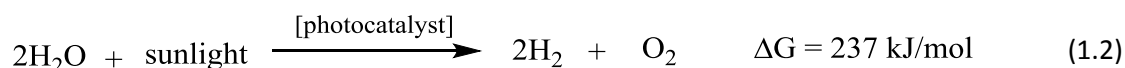
The implementation of such a "hydrogen economy" requires improvements and advances not just in the field of photocatalytic water splitting, but also in hydrogen storage and safety.[9] While, hydrogen has a high energy density from the gravimetric point of view (1 kg of hydrogen is equivalent to 2.64 kg of diesel), the volumetric energy density is rather low (1 liter of diesel is equivalent to 20 L of hydrogen (200 bar).[9,10]

[‡‡] CO_2 and H_2 (syngas) can be converted into liquid hydrocarbon fuels (i.e. methanol, diesel) by employing Fischer-Tropsch process.

Thus, to meet the demand for various applications it is still necessary to find out other suitable ways of storing H_2 instead of in its pristine form under high pressure containers (200-700 bar) or liquid cryo-storage[§§]. Another promising approach is to store hydrogen by forming new chemical bonds. This can be in the form of metal hydrides like MgH_2 and $LiBH_4$ or even combining H_2 with abundant resources like N_2, CO_2 and O_2 for instance.[10,11]

By combining H_2 with N_2 one can obtain ammonia as shown in eq. 1.3, or by reacting with CO_2 it is possible to generate methanol as indicated in eq. 1.4.[12,13] Renewable energy driven water splitting could provide an alternative hydrogen source for ammonia and methanol synthesis with the advantage of releasing no CO_2 into the atmosphere. Nowadays, the Haber-Bosch process hydrogenates over 120 million metric tons of nitrogen to produce ammonia for fertilizers (eq. 1.3). However, the H_2 consumed in the Haber-Bosch process is produced mainly by steam reforming or coal gasification and consumes up to 5% of the world's natural gas production liberating large amounts of CO_2 to the environment.[14] Although, methanol is currently synthesized from syngas using non-renewable sources such as natural gas, naphtha or coal over heterogeneous catalysts[15] the direct synthesis of methanol from carbon dioxide and hydrogen has been proposed in response to reduce CO_2 levels in the atmosphere besides reaching CO_2 neutral production.[13,16] In 2007, a company in Reykjavik – Iceland, demonstrated the feasibility of the conversion of CO_2 from geothermal or industrial emissions and hydrogen produced from renewable energy toward methanol.[17] The pilot plant production with a capacity of 5 million liters/year is already suppling renewable methanol to fuel cars or used for blends with gasoline according to EU standards.[***]

$$N_2 \ + \ 3H_2 \ \longrightarrow \ 2NH_3 \qquad\qquad (1.3)$$

$$CO_2 \ + \ 3H_2 \ \longrightarrow \ CH_3OH \ + \ H_2O \qquad (1.4)$$
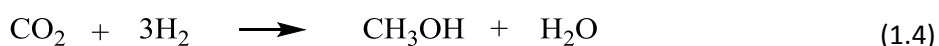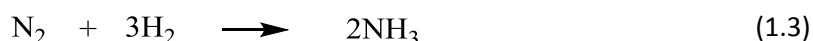
Therefore, the conversion of solar energy into hydrogen and its storage through generating new chemical bonds appears to be a very attractive approach towards reducing the dependence on fossil fuels.

1.4   Design and developing materials for heterogeneous photocatalysis

Heterogeneous catalysis is of paramount significance for the modern society as it is part of the basis of modern chemical industry. A multitude of products and molecular building blocks are manufactured from using petroleum and natural gas as feedstock by employing solid catalysts. The list of manufactured products is large such as: fuels, fertilizers, flagrances, flavours, polymers, fabrics and pharmaceuticals.

[§§] Mainly because of safety and high cost issues, respectively.
[***] Carbon Recycling International (CRI): 1st renewable methanol fuel station in the world for electric cars (www.carbonrecycling.is).

Additionally, several commodities precursors are also produced by employing catalysts like: ammonia, ethylene, benzene, toluene, xylene and terephtalic acid and other several monomers for the polymer industry, for instance.[18-20]

Heterogeneous (photo)catalysis is driven by the catalyst surface, i.e. size, area, local composition and morphology including the ability to transfer charges. It has been revealed that physical properties of nanocrystals are strongly influenced by two geometrical parameters: size and shape. Hence, the ability to control and manipulate the nanocrystals size and shape is advantageous to tune the physical and chemical properties of (photo)catalysts. For instance, it has been reported both experimentally[21] and theoretically[22] that the electronic band of a crystal is gradually quantized as its geometric size is reduced, resulting in an increase in the band-gap energy. Likewise, the properties of a crystal are also influenced by its shape, as demonstrated by the catalytic reaction between hexacyanoferrate (III) and thiosulfate ions using tetrahedral, cubic and quasi-spherical platinum nanocrystals.[23] The chemical growth of nanomaterials in liquid media commonly involves the process of precipitation of a solid phase from solution. Thus, the understanding of process and parameters controlling the precipitation is a key to achieve customized size and shapes. Roughly, the growth process can be divided in 3 stages: (i) generation of nuclei, (ii) evolution of nuclei into seeds, (iii) growth of seeds into nanocrystals.[24,25] Therefore, monodisperse colloids are produced by one single and short time nucleation event followed by slower growth on the existing nuclei.[25] The sol-gel method can be used to obtain monodisperse colloids by making use of coordinating solvents (alkylphosphines, surfactants and organic ligands), which bind to the surface of nanocrystals. The role of the coordinating solvent is to stabilize the nanocrystals in solution and slow the mass diffusion rate to the nanocrystals, resulting in smaller average crystal size.[26,27] The customized shape of nanocrystals has been widely studied for several different morphologies.[25,28,29] These basic building blocks have unique geometries and properties and can be used further as components in more complex nanostructures. If the assembly of several components, each with different geometries can be controlled, the construction of novel nanostructures may be possible. Therefore, the anisotropic growth of nanocrystals is promoted by three main shape-controlling mechanisms: (i) seed-mediated solution-liquid-solid growth, (ii) shape transformation through oriented attachment, and (iii) kinetically induced anisotropic growth. The kinetically induced anisotropic growth can be used as a good example to demonstrate the shape control. This mechanism growth is very effective to produce different shapes of nanocrystals from molecular precursors, because the surface energy of the nanocrystals can be tuned by introducing surfactants that adsorb onto surfaces of growing crystallites. When surfactants or organic ligands stabilize a certain surface by "selective adhesion", the growth rate difference between different crystallographic directions can be accentuated.[29,30]

Photocatalysis has its roots in the beginning of the 20th century in the Soviet Union and Europe registering an exponential growth from 1970 in the field of heterogeneous photocatalysis regarding

environmental remediation.[31] In particular, photocatalysis has been the focus of intense research in recent years because of alarming energy scenarios and the urgency to reduce our carbon footprint. The number of scientific reports on this topic exceeded 8700 just in 2014.[†††] The amount of solar energy reaching Earth's surface exceeds the human demand for energy;[6c] the challenge is to collect, convert and store this diffuse and intermittent source of energy efficiently. The growing interest is based on the possibility of converting the free and abundant sunlight energy into chemical energy, to oxidize or reduce materials or to obtain useful materials such as hydrocarbons,[32,33] hydrogen and oxygen[34,35] as well as for environmental remediation[36] and water treatment.[37] In this context, the development of new heterogeneous photocatalysts for H_2 generation is highly desired. However, the design of photocatalysts for H_2 evolution requires a series of features such as: i) semiconductor materials able to utilize sunlight effectively with a suitable band gap in the range of 2.4 eV including band gap engineering through ion or anion doping; ii) photostability over longer period of time and no degradation or deactivation during reaction cycles; iii) charge carrier dynamics and the need to form long-living separated charges to drive the multi-electron reduction of water; iv) optical absorption as fundamental factor for photocatalytic activity that is closely related to the crystal structure, morphology, exposed facets and pore structure of the photo-semiconductor and v) all of the above at low cost.

Synthetic methodologies are fundamental to tailor and develop photocatalysts features beyond tuning the particle size, surface area, crystalline phase and exposed facets. One feasible and promising direction in inorganic and materials chemistry synthesis and design of photocatalysts is to exploit the structural dimensionality to build more sophisticated architectures than those that are currently known, such as decorated-, encapsulated- and heterojunctions-structures for instance. Structural dimensionality is an additional feature that can provide a convenient way to tune the photocatalytic properties by confining electrons into zero-, one-, two- dimensions or delocalizing them into three dimensions.[38,39] Therefore, designing nanostructure architectures with different morphologies and properties is the subject of extensive research. Attention is focused on photocatalysts based on metal oxides, in particular TiO_2[40] materials that include nanospheres (0-D),[41] -wires, -rods, -tubes and ribbons (1-D),[42] nanosheets, -platelets and -disks (2-D)[43] and mesoporous structures or interconnected architecture (3-D)[44,45] as illustrated in Fig. 1.3. These materials possess novel physical and chemical properties that are completely different from those observed in bulk materials.[39]

Several techniques have been developed to produce 0-D, 1-D, 2-D and 3-D nanostructures, however one must consider which methodologies are prone to bring all those geometries and dimensions together either in one single structure or in a hybrid structures. There are several designs used as photocatalysts reported in the literature such as mesoporous-, decorated-, encapsulated- and multi-junction-structures either for particulate or thin film photoelectrodes as shown in Fig. 1.4.

[†††] Number of publications with topic keywords of "photocatal*" using Web of Science database, researched in June, 2015.
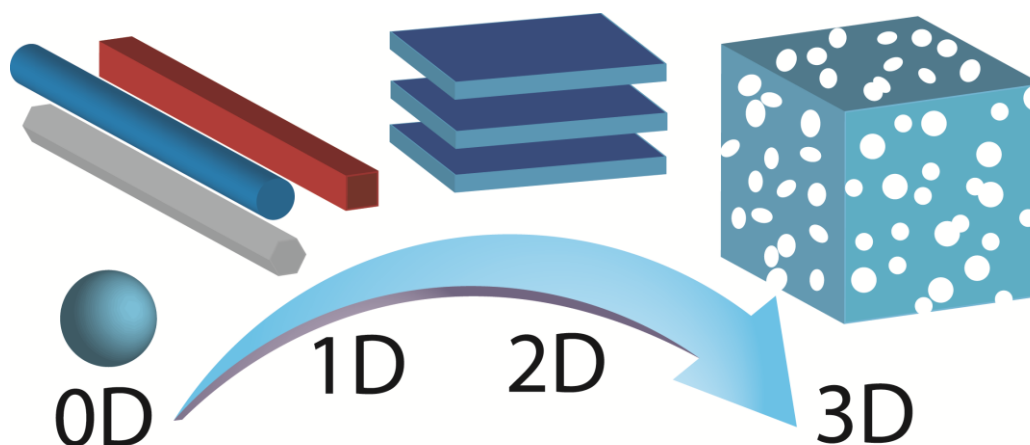
Figure 1.3 Schematic illustration of structural dimensionality of materials. In 0-D the electrons are confined into all dimensions, while 1-D and 2-D electrons are confined into one or two dimensions, respectively. Finally in 3-D electrons are delocalized. This Figure was adapted from Ref. 39.

In general, all these structures can be synthesized using wet chemical processes, with the exception of thin films employed as electrodes that are more likely to be produced by physical- or chemical- vapor deposition[46] and sputtering[47] due to the superior homogeneity and reproducibility. The mesoporous materials are characterized by the presence of pores in the range of 2-50 nm diameter and are prepared conventionally by using templating agents (polymers, co-polymers, surfactants etc.) which are incorporated into a material and later removed or destroyed, leaving pores whose nature and degree of connectivity are driven by the templating agent.[48] Template-free methods are also available to prepare mesoporous materials, however this kind of approach is restricted to few compositions and is based on sol-gel chemistry.[49]

The decorated configuration consists of a photocatalyst as the main component (mostly over 98 wt.%) decorated with smaller noble metals or transition-metals (preferentially as nanoparticles) employed as co-catalyst, usually obtained by wet routes like sol immobilization followed by reduction,[50] wet impregnation[51] or *in situ* photodeposition.[52,53] Similarly, to the impregnation and photodeposition methods other modifications can be introduced in order to prevent the water splitting back reaction by adding a protective layer or by encapsulating the co-catalyst, the current method is commonly known as core-shell method. This method consist of encapsulating the core (usually a metal nanoparticle) with a resistant metal oxide thin layer (Cr_2O_3, SiO_2 for instance) designated shell as reported by Domen et al..[54] An incremental modification was later reported by the same group regarding the use of a core/shell structure to spatially separate the co-catalyst sites for hydrogen (inner part of the spheres) and oxygen evolution (outer surface of the sphere) avoiding in this way the undesired water splitting back reaction.[55]

The scarcity of single photo-semiconductors (PS) that can be used for efficient solar water splitting have stimulated the combination of two or multiple semiconductors with different band gaps in order to absorb a larger fraction of the solar spectrum, and in addition to provide the necessary band-edge energy

levels to obtain overall water splitting. In this respect, the synthesis of heterojunctions for particulate systems are based on sol-gel routes and are usually restricted to the combination of two photosemiconductors such as Bi_2S_3/TiO_2,[56] CdS/TiO_2,[56] Cu_2O/TiO_2,[57] WO_3/TiO_2,[58] $BiVO_4/TiO_2$,[59] α-Fe_2O_3, WO_3 and CdS deposited on ZnO[60] for instance. Additionally, photo-semiconductors (PS1, PS2 as depicted in Fig. 1.4) mediated conductive layers were also considered as a promising configuration for water splitting devices, i.e. the conductive layer acts as the shuttle for the charge transfer between the two components and may also act as support for proton reduction, as a result of synergy provided between different photo-semiconductors coupled with a conductive layer such as reduced graphene oxide.[61,62,64] This mediated conductive layer obtained by simple mixing of the single components under hydrothermal conditions to achieve close effective contact between the components resulted in satisfactory photoactivities.[61,62] The same approach used for producing heterojunctions in particulate system can be extended for the preparation of (photo)electrodes or PEC devices. Briefly, PEC water splitting devices, which use solar energy to convert water into hydrogen and oxygen, can be configured as: (i) photoanode + photocathode, and (ii) tandem cell absorber + electrocatalyst. These photoelectrodes are feasible to be prepared as double or triple heterojunction (also called multi-junction as illustrated in Fig. 1.4) systems as reported by several groups.[63] Several examples of multi-junctions were published recently by Fan et al. on the fabrication of a ternary TiO_2/reduced graphene oxide (RGO)/Cu_2O heterostructure by using a RGO layer between TiO_2 and Cu_2O, which exhibited significant photocurrent improvement compared to the pristine TiO_2.[64] Huang et al. also fabricated a ternary photoelectrode made of $Cu_2O/CuO/TiO_2$ nanowire arrays on Au substrates. The Cu_2O layer on CuO/TiO_2 was found to prevent the photo-corrosion and enhanced the overall photocurrent of CuO.[65] Shankar and Cho et al. reported on a hierarchically branched TiO_2 nanorod structure (1-D oriented) that can be used as model for efficient photoelectrochemical hydrogen production which offers a large contact area with the electrolyte, excellent light absorption and a highly conductive pathway for charge carrier collection. The thin films were prepared by screen printing of commercial TiO_2 nanoparticles onto conductive substrates followed by calcination in air (also illustrated in Fig. 1.4).[66,67]

In the coming decades, more advances are expected in the areas of materials and inorganic synthesis. Another important feature that has to be considered in designing effective photocatalysts is based on the understanding of kinetics and mechanisms. Hence, time resolved spectroscopy, *in situ* characterization, and theoretical and computational studies, in particular of more complex catalysts and architectures may contribute to the development of efficient photocatalysts or photoelectrodes configurations.
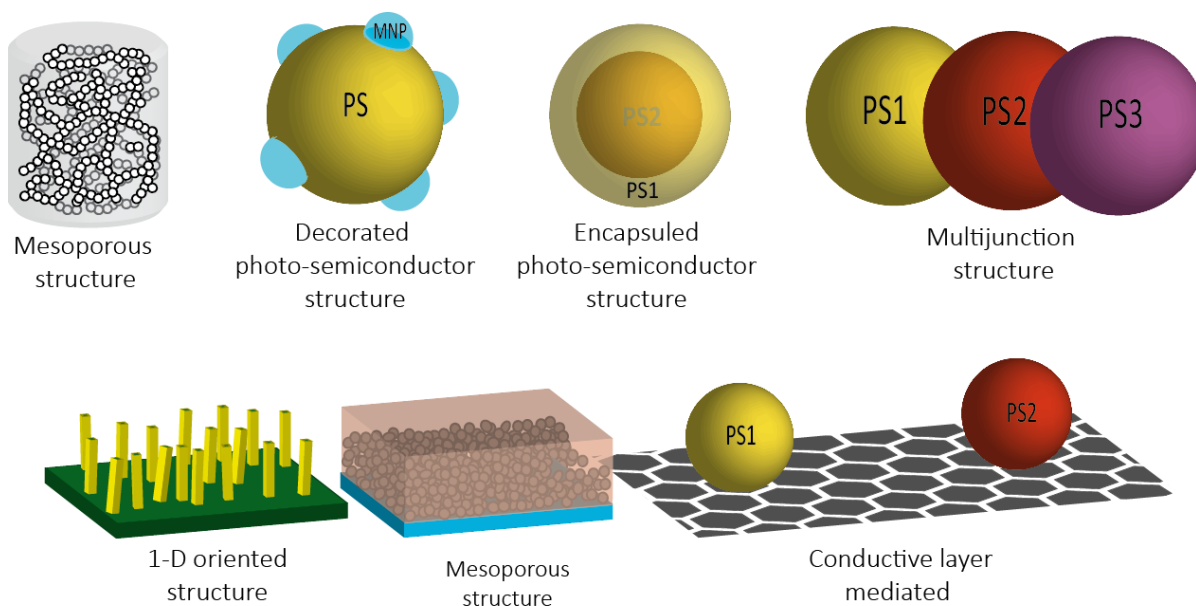
Figure 1.4 Schematic illustration of the different kinds of structures and configurations used to achieve improved charge separation. (Legend: PS = photo-semiconductor, MNP = metallic nanoparticle).

1.5 Nanoparticle self-assembly to achieve new mesoscopic and macroscopic architectures for catalysis

The ability to design inorganic materials into 1-, 2-, and 3 dimensions at the nanoscale using self-assembly may play a vital role in advancing the fields of (photo)catalysis, environmental remediation and energy conversion. Within the field of nanotechnology, NP are ideal building blocks for the fabrication of superstructures.[68] In this respect, self-assembly of nanoparticles has been identified as an important process where the building blocks spontaneously organize into ordered structures by thermodynamic and other constraints. However, in order to successfully exploit nanoparticle self-assembly in technological applications and to ensure efficient scale-up, a high level of direction and control is required. The appealing feature to use NP as building blocks relies on their unprecedented physical and chemical properties compared to the corresponding bulk material. Gold, for instance can illustrate these unprecedented properties very well: bulk gold is yellow, shiny, melts around 1337 K and it is one of the least reactive elements. While colloidal gold with 10 nm sizes appears red in aqueous solution, its melting temperature decreases significantly as the size goes down and it becomes catalytically active.[69] The activity is so much enhanced that gold NP are excellent catalysts for CO oxidation, olefin hydrogenation and redox reactions.[70] The interaction between nanoparticulate building blocks as consequence of their spatial arrangement can result in novel and unique properties that are not found in the individual components. Hence the challenge in materials chemistry is to combine the size effects to induce properties that supersede those of the single units.[71]

Several strategies are known to assemble NP into superstructures, however most of them result in arrangements with just a few micrometers range order.[72] Therefore, the development of assembly methods that can provide ordered structures over longer distance (i.e. centimeters) is of fundamental importance to obtain the aforementioned collective properties in macroscopic materials. One very insightful approach was developed by Niederberger et al. which consists of an anisotropic "polymerization" of TiO_2 nanocrystals into wires and further modification to obtain macroscopic 3D networks.[73,74] The polymerization approach based on solution chemistry exploits the fact that TiO_2 nanoparticles spontaneously grow by the oriented attachment mechanism.[‡‡‡] In detail, ligands that can selectively attach on specific surface facets steer the anisotropic growth of the nanostructure.[75] For example, nanopowders composed of surface-functionalized anatase crystals self-organize into different structures upon redispersion in water. Previous reports suggested that the obtained anisotropic structure is a consequence of the ligand functionality and also to the water-promoted desorption of the organic ligands from the {001} facets of the crystalline building blocks, in addition to the selective replacement of water on these crystal facets. Both processes induce the preferred attachment of the titania nanoparticles along the [001] direction as shown in Fig. 1.5.[73a,73b]
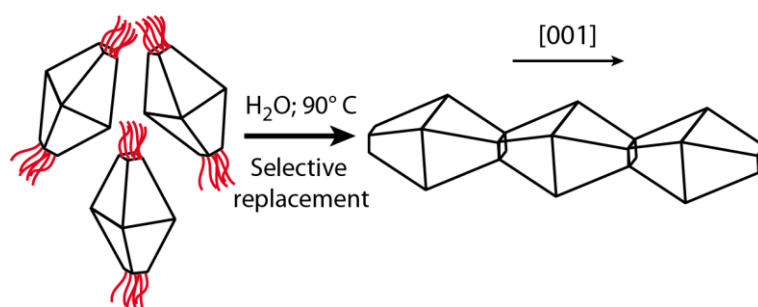
Figure 1.5 Proposed mechanism for the anisotropic growth of TiO_2 into wires. TiO_2 nanocrystals are functionalized with amino compound ($NH_2C(CH_2OH)_3$) subsequently the powder is dispersed in water and heated up for a couple of minutes to 90°C to induce the selective replacement of the amino compound until gelation takes place.

Thus, the method demonstrated the feasibility of the self-assembly approach to obtain macroscopic structures with several centimeters in length, by using titania anatase nanocrystals (in the range of 2-3 nm) as building blocks. Although the macroscopic structure i.e. the mesoporous crystalline aerogel obtained is still primitive regarding its counterparts produced by molecular self-assembly or nanofabrication[76] it signifies a breakthrough in controlling nanocrystals organization and spatial arrangement over the centimeters range. In addition it provides a new method to obtain architectural design of catalysts at multiple scales, as illustrated by Fig. 1.5.[74, 77]

[‡‡‡] Interaction and aggregation along specific crystallographic directions to form 1-D nano-wires or nano-rods to 2 or 3-D superstructures.

1.6   References

1.   Mauna Loa Observatory, Hawaii. 2013.
2.   BP Energy Outlook 2035. 2015.
3.   (a) BP Statistical Review of World Energy. 2015, *64*, 48; (b) IEA, *Key World Energy Statistics 2014*. OECD Publishing.
4.   Whitmarsh, J.; Govindjee, The Photosynthetic Process. In *Concepts in Photobiology*, Singhal, G. S.; Renger, G.; Sopory, S. K.; Irrgang, K. D.; Govindjee, Eds. Springer Netherlands: 1999; pp 11-51.
5.   Listorti, A.; Durrant, J.; Barber, J., Artificial photosynthesis: Solar to fuel. *Nat Mater* 2009, *8* (12), 929-930.
6.   (a) Turner, J. A., A realizable renewable energy future. *Science* 1999, *285* (5428), 687-689; (b) Turner, J. A., Sustainable hydrogen production. *Science* 2004, *305* (5686), 972-974; (c) Lewis, N. S.; Nocera, D. G., Powering the planet: Chemical challenges in solar energy utilization. *Proc. Natl. Acad. Sci. U. S. A.* 2006, *103* (43), 15729-15735; (d) Navarro Yerga, R. M.; Alvarez Galvan, M. C.; del Valle, F.; Villoria de la Mano, J. A.; Fierro, J. L. G., Water Splitting on Semiconductor Catalysts under Visible-Light Irradiation. *Chemsuschem* 2009, *2* (6), 471-485; (e) Kim, D.; Sakimoto, K. K.; Hong, D.; Yang, P., Artificial Photosynthesis for Sustainable Fuel and Chemical Production. *Angewandte Chemie International Edition* 2015, *54* (11), 3259-3266.
7.   Hirose, K., Hydrogen as a fuel for today and tomorrow: expectations for advanced hydrogen storage materials/systems research. *Faraday Discuss* 2011, *151*, 11-18.
8.   Osterloh, F. E., Inorganic materials as catalysts for photochemical splitting of water. *Chem. Mat.* 2008, *20* (1), 35-54.
9.   Edwards, P. P.; Kuznetsov, V. L.; David, W. I. F., Hydrogen energy. *Philos. Trans. R. Soc. A-Math. Phys. Eng. Sci.* 2007, *365* (1853), 1043-1056.
10.   Klell, M., Storage of Hydrogen in the Pure Form. In *Handbook of Hydrogen Storage*, Wiley-VCH Verlag GmbH & Co. KGaA: 2010; pp 1-37.
11.   Huot, J., Metal Hydrides. In *Handbook of Hydrogen Storage*, Wiley-VCH Verlag GmbH & Co. KGaA: 2010; pp 81-116.
12.   Hirano, M.; Akano, T.; Imai, T.; Kuroda, K., Methanol synthesis from carbon dioxide on $CuO-ZnO-Al_2O_3$ catalysts. In *Advances in Chemical Conversions for Mitigating Carbon Dioxide*, Inui, T.; Anpo, M.; Izui, K.; Yanagida, S.; Yamaguchi, T., Eds. 1998; Vol. 114, pp 545-548.
13.   Ganesh, I., Conversion of carbon dioxide into methanol - a potential liquid fuel: Fundamental challenges and opportunities (a review). *Renewable & Sustainable Energy Reviews* 2014, *31*, 221-257.
14.   Rockstrom, J.; Steffen, W.; Noone, K.; Persson, A.; Chapin, F. S.; Lambin, E. F.; Lenton, T. M.; Scheffer, M.; Folke, C.; Schellnhuber, H. J.; Nykvist, B.; de Wit, C. A.; Hughes, T.; van der Leeuw, S.; Rodhe, H.; Sorlin, S.; Snyder, P. K.; Costanza, R.; Svedin, U.; Falkenmark, M.; Karlberg, L.; Corell, R. W.; Fabry, V. J.; Hansen, J.; Walker, B.; Liverman, D.; Richardson, K.; Crutzen, P.; Foley, J. A., A safe operating space for humanity. *Nature* 2009, *461* (7263), 472-475.
15.   Bradford, M. C. J.; Vannice, M. A., CO_2 reforming of CH_4. *Catal. Rev.-Sci. Eng.* 1999, *41* (1), 1-42.
16.   Rodemerck, U.; Holeňa, M.; Wagner, E.; Smejkal, Q.; Barkschat, A.; Baerns, M., Catalyst Development for CO_2 Hydrogenation to Fuels. *ChemCatChem* 2013, *5* (7), 1948-1955.
17.   Arthur M. Shulenberger, F. R. J., Oddur Ingolfsson, Kim-Chinh Tran Process for producing liquid fuel from carbon dioxide and water US 20070244208 A1, 2007.
18.   (a) Lloyd, L., Industrial Catalysts. In *Handbook of Industrial Catalysts*, Springer US: 2011; pp 1-22; (b) Lloyd, L., Catalytic Cracking Catalysts. In *Handbook of Industrial Catalysts*, Springer US: 2011; pp 169-210; (c) Lloyd, L., Refinery Catalysts. In *Handbook of Industrial Catalysts*, Springer US: 2011; pp 211-260; (d) Lloyd, L., Petrochemical Catalysts. In *Handbook of Industrial Catalysts*, Springer US: 2011; pp 261-310; (e) Lloyd, L., Olefin Polymerization Catalysts. In *Handbook of Industrial Catalysts*, Springer US: 2011; pp 311-350; (f) Lloyd, L., Ammonia and Methanol Synthesis. In *Handbook of Industrial Catalysts*, Springer US: 2011; pp 397-437.
19.   Chapuis, C.; Jacoby, D., Catalysis in the preparation of fragrances and flavours. *Applied Catalysis a-General* 2001, *221* (1-2), 93-117.
20.   Juan, J. B.-S.; Raghunath, V. C.; Bala, S., Design of Heterogeneous Catalysts for Fuels and Chemicals Processing: An Overview. In *Novel Materials for Catalysis and Fuels Processing*, American Chemical Society: 2013; Vol. 1132, pp 3-68.
21.   Li, L.-s.; Hu, J.; Yang, W.; Alivisatos, A. P., Band Gap Variation of Size- and Shape-Controlled Colloidal CdSe Quantum Rods. *Nano Lett* 2001, *1* (7), 349-351.
22.   Hu, J.; Li, L.-s.; Yang, W.; Manna, L.; Wang, L.-w.; Alivisatos, A. P., Linearly Polarized Emission from Colloidal Semiconductor Quantum Rods. *Science* 2001, *292* (5524), 2060-2063.
23.   Narayanan, R.; El-Sayed, M. A., Shape-Dependent Catalytic Activity of Platinum Nanoparticles in Colloidal Solution. *Nano Lett* 2004, *4* (7), 1343-1348.

24.   LaMer, V. K.; Dinegar, R. H., Theory, Production and Mechanism of Formation of Monodispersed Hydrosols. *J. Am. Chem. Soc.* 1950, *72* (11), 4847-4854.

25.   Burda, C.; Chen, X.; Narayanan, R.; El-Sayed, M. A., Chemistry and Properties of Nanocrystals of Different Shapes. *Chem. Rev.* 2005, *105* (4), 1025-1102.

26.   Murray, C. B.; Norris, D. J.; Bawendi, M. G., Synthesis and characterization of nearly monodisperse CdE (E = sulfur, selenium, tellurium) semiconductor nanocrystallites. *J. Am. Chem. Soc.* 1993, *115* (19), 8706-8715.

27.   Hyeon, T.; Chung, Y.; Park, J.; Lee, S. S.; Kim, Y.-W.; Park, B. H., Synthesis of Highly Crystalline and Monodisperse Cobalt Ferrite Nanocrystals. *The Journal of Physical Chemistry B* 2002, *106* (27), 6831-6833.

28.   Xia, Y.; Xiong, Y.; Lim, B.; Skrabalak, S. E., Shape-Controlled Synthesis of Metal Nanocrystals: Simple Chemistry Meets Complex Physics? *Angewandte Chemie International Edition* 2009, *48* (1), 60-103.

29.   Jun, Y.-w.; Choi, J.-s.; Cheon, J., Shape Control of Semiconductor and Metal Oxide Nanocrystals through Nonhydrolytic Colloidal Routes. *Angewandte Chemie International Edition* 2006, *45* (21), 3414-3439.

30.   Joo, J.; Kwon, S. G.; Yu, J. H.; Hyeon, T., Synthesis of ZnO Nanocrystals with Cone, Hexagonal Cone, and Rod Shapes via Non-Hydrolytic Ester Elimination Sol–Gel Reactions. *Adv. Mater.* 2005, *17* (15), 1873-1877.

31.   Serpone, N.; Emeline, A. V.; Horikoshi, S.; Kuznetsov, V. N.; Ryabchuk, V. K., On the genesis of heterogeneous photocatalysis: a brief historical perspective in the period 1910 to the mid-1980s. *Photochemical & Photobiological Sciences* 2012, *11* (7), 1121-1150.

32.   Varghese, O. K.; Paulose, M.; LaTempa, T. J.; Grimes, C. A., High-Rate Solar Photocatalytic Conversion of CO_2 and Water Vapor to Hydrocarbon Fuels. *Nano Lett* 2009, *9* (2), 731-737.

33.   Dimitrijevic, N. M.; Vijayan, B. K.; Poluektov, O. G.; Rajh, T.; Gray, K. A.; He, H.; Zapol, P., Role of Water and Carbonates in Photocatalytic Transformation of CO_2 to CH_4 on Titania. *J. Am. Chem. Soc.* 2011, *133* (11), 3964-3971.

34.   Kudo, A.; Miseki, Y., Heterogeneous photocatalyst materials for water splitting. *Chem. Soc. Rev.* 2009, *38* (1), 253-278.

35.   Maeda, K.; Domen, K., New non-oxide photocatalysts designed for overall water splitting under visible light. *J. Phys. Chem. C* 2007, *111* (22), 7851-7861.

36.   Caballero, L.; Whitehead, K. A.; Allen, N. S.; Verran, J., Inactivation of Escherichia coli on immobilized TiO_2 using fluorescent light. *Journal of Photochemistry and Photobiology a-Chemistry* 2009, *202* (2-3), 92-98.

37.   McCullagh, C.; Robertson, J. M. C.; Bahnemann, D. W.; Robertson, P. K. J., The application of TiO_2 photocatalysis for disinfection of water contaminated with pathogenic micro-organisms: a review. *Research on Chemical Intermediates* 2007, *33* (3-5), 359-375.

38.   Tiwari, J. N.; Tiwari, R. N.; Kim, K. S., Zero-dimensional, one-dimensional, two-dimensional and three-dimensional nanostructured materials for advanced electrochemical energy devices. *Prog. Mater. Sci.* 2012, *57* (4), 724-803.

39.   Nakata, K.; Fujishima, A., TiO_2 photocatalysis: Design and applications. *Journal of Photochemistry and Photobiology C-Photochemistry Reviews* 2012, *13* (3), 169-189.

40.   (a) Hoffmann, M. R.; Martin, S. T.; Choi, W. Y.; Bahnemann, D. W., Environmental applications of semiconductor photocatalysis *Chem. Rev.* 1995, *95* (1), 69-96; (b) Linsebigler, A. L.; Lu, G.; Yates, J. T., Photocatalysis on TiO_2 Surfaces: Principles, Mechanisms, and Selected Results. *Chem. Rev.* 1995, *95* (3), 735-758; (c) Chen, X.; Mao, S. S., Titanium dioxide nanomaterials: Synthesis, properties, modifications, and applications. *Chem. Rev.* 2007, *107* (7), 2891-2959; (d) Chen, H.; Nanayakkara, C. E.; Grassian, V. H., Titanium Dioxide Photocatalysis in Atmospheric Chemistry. *Chem. Rev.* 2012, *112* (11), 5919-5948; (e) Kamat, P. V., TiO_2 Nanostructures: Recent Physical Chemistry Advances. *J. Phys. Chem. C* 2012, *116* (22), 11849-11851; (f) Chen, X.; Selloni, A., Introduction: Titanium Dioxide (TiO_2) Nanomaterials. *Chem. Rev.* 2014, *114* (19), 9281-9282.

41.   Cargnello, M.; Gordon, T. R.; Murray, C. B., Solution-Phase Synthesis of Titanium Dioxide Nanoparticles and Nanocrystals. *Chem. Rev.* 2014, *114* (19), 9319-9345.

42.   Wang, X.; Li, Z.; Shi, J.; Yu, Y., One-Dimensional Titanium Dioxide Nanomaterials: Nanowires, Nanorods, and Nanobelts. *Chem. Rev.* 2014, *114* (19), 9346-9384.

43.   Wang, L.; Sasaki, T., Titanium Oxide Nanosheets: Graphene Analogues with Versatile Functionalities. *Chem. Rev.* 2014, *114* (19), 9455-9486.

44.   Rolison, D. R., Catalytic nanoarchitectures - The importance of nothing and the unimportance of periodicity. *Science* 2003, *299* (5613), 1698-1701.

45.   Fattakhova-Rohlfing, D.; Zaleska, A.; Bein, T., Three-Dimensional Titanium Dioxide Nanomaterials. *Chem. Rev.* 2014, *114* (19), 9487-9558.

46.   (a) Murakami, T. N.; Kijitori, Y.; Kawashima, N.; Miyasaka, T., Low temperature preparation of mesoporous TiO2 films for efficient dye-sensitized photoelectrode by chemical vapor deposition combined with UV light irradiation. *Journal of Photochemistry and Photobiology a-Chemistry* 2004, *164* (1-3), 187-191; (b) Le Formal, F.; Graetzel, M.; Sivula, K., Controlling Photoactivity in Ultrathin Hematite Films for Solar Water-Splitting. *Adv. Funct. Mater.* 2010, *20* (7), 1099-1107.

47.   (a) Glasscock, J. A.; Barnes, P. R. F.; Plumb, I. C.; Savvides, N., Enhancement of photoelectrochemical hydrogen production from hematite thin films by the introduction of Ti and Si. *J. Phys. Chem. C* 2007, *111* (44), 16477-16488; (b) Seger, B.; Pedersen, T.; Laursen, A. B.; Vesborg, P. C. K.; Hansen, O.; Chorkendorff, I., Using TiO_2 as a Conductive Protective Layer for Photocathodic H_2 Evolution. *J. Am. Chem. Soc.* 2013, *135* (3), 1057-1064.

48.   (a) Taguchi, A.; Schüth, F., Ordered mesoporous materials in catalysis. *Microporous and Mesoporous Materials* 2005, *77* (1), 1-45; (b) Ismail, A. A.; Bahnemann, D. W., Mesoporous titania photocatalysts: preparation, characterization and reaction mechanisms. *J. Mater. Chem.* 2011, *21* (32), 11686-11707.

49.   (a) Yu, J. G.; Su, Y. R.; Cheng, B., Template-Free Fabrication and Enhanced Photocatalytic Activity of Hierarchical Macro-/Mesoporous Titania. *Adv. Funct. Mater.* 2007, *17* (12), 1984-1990; (b) Yu, C. C.; Zhang, L. X.; Shi, J. L.; Zhao, J. J.; Gao, J. H.; Yan, D. S., A simple template-free strategy to synthesize nanoporous manganese and nickel oxides with narrow pore size distribution, and their electrochemical properties. *Adv. Funct. Mater.* 2008, *18* (10), 1544-1554.

50.   (a) Dimitratos, N.; Lopez-Sanchez, J. A.; Morgan, D.; Carley, A.; Prati, L.; Hutchings, G. J., Solvent free liquid phase oxidation of benzyl alcohol using Au supported catalysts prepared using a sol immobilization technique. *Catal. Today* 2007, *122* (3–4), 317-324; (b) Priebe, J. B.; Karnahl, M.; Junge, H.; Beller, M.; Hollmann, D.; Brückner, A., Water Reduction with Visible Light: Synergy between Optical Transitions and Electron Transfer in Au-TiO2 Catalysts Visualized by In situ EPR Spectroscopy. *Angewandte Chemie International Edition* 2013, *52* (43), 11420-11424.

51.   (a) Li, W. C.; Comotti, M.; Schuth, F., Highly reproducible syntheses of active Au/TiO_2 catalysts for CO oxidation by deposition-precipitation or impregnation. *J Catal* 2006, *237* (1), 190-196; (b) Zhong, D. K.; Cornuz, M.; Sivula, K.; Graetzel, M.; Gamelin, D. R., Photo-assisted electrodeposition of cobalt-phosphate (Co-Pi) catalyst on hematite photoanodes for solar water oxidation. *Energy Environ. Sci.* 2011, *4* (5), 1759-1764.

52.   Kraeutler, B.; Bard, A. J., Heterogeneous photocatalytic preparation of supported catalysts. Photodeposition of platinum on titanium dioxide powder and other substrates. *J. Am. Chem. Soc.* 1978, *100* (13), 4317-4318.

53.   Meyer, T.; Priebe, J. B.; da Silva, R. O.; Peppel, T.; Junge, H.; Beller, M.; Brueckner, A.; Wohlrab, S., Advanced Charge Utilization from $NaTaO_3$ Photocatalysts by Multilayer Reduced Graphene Oxide. *Chem. Mat.* 2014, *26* (16), 4705-4711.

54.   Maeda, K.; Teramura, K.; Lu, D.; Saito, N.; Inoue, Y.; Domen, K., Noble-Metal/Cr_2O_3 Core/Shell Nanoparticles as a Cocatalyst for Photocatalytic Overall Water Splitting. *Angewandte Chemie International Edition* 2006, *45* (46), 7806-7809.

55.   Wang, D.; Hisatomi, T.; Takata, T.; Pan, C.; Katayama, M.; Kubota, J.; Domen, K., Core/Shell Photocatalyst with Spatially Separated Co-Catalysts for Efficient Reduction and Oxidation of Water. *Angewandte Chemie International Edition* 2013, *52* (43), 11252-11256.

56.   Bessekhouad, Y.; Robert, D.; Weber, J., Bi_2S_3/TiO_2 and CdS/TiO_2 heterojunctions as an available configuration for photocatalytic degradation of organic pollutant. *Journal of Photochemistry and Photobiology a-Chemistry* 2004, *163* (3), 569-580.

57.   Besskhouad, Y.; Robert, D.; Weber, J. V., Photocatalytic activity of CU_2O/TiO_2, Bi_2O_3/TiO_2 and $ZnMn_2O_4/TiO_2$ heterojunctions. *Catal. Today* 2005, *101* (3-4), 315-321.

58.   Leghari, S. A. K.; Sajjad, S.; Chen, F.; Zhang, J., WO_3/TiO_2 composite with morphology change via hydrothermal template-free route as an efficient visible light photocatalyst. *Chemical Engineering Journal* 2011, *166* (3), 906-915.

59.   Zalfani, M.; van der Schueren, B.; Hu, Z.-Y.; Rooke, J. C.; Bourguiga, R.; Wu, M.; Li, Y.; Van Tendeloo, G.; Su, B.-L., Novel 3DOM $BiVO_4/TiO_2$ nanocomposites for highly enhanced photocatalytic activity. *Journal of Materials Chemistry A* 2015, *3* (42), 21244-21256.

60.   Sakthivel, S.; Geissen, S. U.; Bahnemann, D. W.; Murugesan, V.; Vogelpohl, A., Enhancement of photocatalytic activity by semiconductor heterojunctions: α-Fe_2O_3, WO_3 and CdS deposited on ZnO. *Journal of Photochemistry and Photobiology A: Chemistry* 2002, *148* (1–3), 283-293.

61.   Xiang, Q.; Yu, J.; Jaroniec, M., Synergetic Effect of MoS_2 and Graphene as Cocatalysts for Enhanced Photocatalytic H_2 Production Activity of TiO_2 Nanoparticles. *J. Am. Chem. Soc.* 2012, *134* (15), 6575-6578.

62.   Huang, C.; Li, C.; Shi, G., Graphene based catalysts. *Energy Environ. Sci.* 2012, *5* (10), 8848-8868.

63.   (a) Reece, S. Y.; Hamel, J. A.; Sung, K.; Jarvi, T. D.; Esswein, A. J.; Pijpers, J. J. H.; Nocera, D. G., Wireless Solar Water Splitting Using Silicon-Based Semiconductors and Earth-Abundant Catalysts. *Science* 2011, *334* (6056), 645-648; (b) Brillet, J.; Yum, J. H.; Cornuz, M.; Hisatomi, T.; Solarska, R.; Augustynski, J.; Graetzel, M.; Sivula, K., Highly efficient water splitting by a dual-absorber tandem cell. *Nat. Photonics* 2012, *6* (12), 823-827; (c) Osterloh, F. E., Inorganic nanostructures for photoelectrochemical and photocatalytic water splitting. *Chem. Soc. Rev.* 2013, *42* (6), 2294-2320; (d) Hisatomi, T.; Kubota, J.; Domen, K., Recent advances in semiconductors for photocatalytic and photoelectrochemical water splitting. *Chem. Soc. Rev.* 2014, *43* (22), 7520-7535.

64.   Fan, W.; Yu, X.; Lu, H.-C.; Bai, H.; Zhang, C.; Shi, W., Fabrication of $TiO_2/RGO/Cu_2O$ heterostructure for photoelectrochemical hydrogen production. *Applied Catalysis B: Environmental* 2016, *181*, 7-15.

14

65.   Yang, J.; Walczak, K.; Anzenberg, E.; Toma, F. M.; Yuan, G.; Beeman, J.; Schwartzberg, A.; Lin, Y.; Hettick, M.; Javey, A.; Ager, J. W.; Yano, J.; Frei, H.; Sharp, I. D., Efficient and Sustained Photoelectrochemical Water Oxidation by Cobalt Oxide/Silicon Photoanodes with Nanotextured Interfaces. *J. Am. Chem. Soc.* 2014, *136* (17), 6191-6194.

66.   Shankar, K.; Basham, J. I.; Allam, N. K.; Varghese, O. K.; Mor, G. K.; Feng, X. J.; Paulose, M.; Seabold, J. A.; Choi, K. S.; Grimes, C. A., Recent Advances in the Use of TiO_2 Nanotube and Nanowire Arrays for Oxidative Photoelectrochemistry. *J. Phys. Chem. C* 2009, *113* (16), 6327-6359.

67.   Cho, I. S.; Chen, Z.; Forman, A. J.; Kim, D. R.; Rao, P. M.; Jaramillo, T. F.; Zheng, X., Branched TiO_2 Nanorods for Photoelectrochemical Hydrogen Production. *Nano Lett* 2011, *11* (11), 4978-4984.

68.   (a) Talapin, D. V.; Lee, J. S.; Kovalenko, M. V.; Shevchenko, E. V., Prospects of Colloidal Nanocrystals for Electronic and Optoelectronic Applications. *Chem. Rev.* 2010, *110* (1), 389-458; (b) Antonietti, M.; Niederberger, M.; Smarsly, B., Self-assembly in inorganic and hybrid systems: beyond the molecular scale. *Dalton Trans.* 2008, (1), 18-24.

69.   Roduner, E., Size matters: why nanomaterials are different. *Chem. Soc. Rev.* 2006, *35* (7), 583-592.

70.   (a) Haruta, M.; Kobayashi, T.; Sano, H.; Yamada, N., Novel gold catalysts for the oxidation of carbon monoxide at a temperature far below 0 degrees C. *Chemistry Letters* 1987, (2), 405-408; (b) Hashmi, A. S. K.; Hutchings, G. J., Gold catalysis. *Angew. Chem.-Int. Edit.* 2006, *45* (47), 7896-7936; (c) Hutchings, G. J., Catalysis by gold. *Catal. Today* 2005, *100* (1-2), 55-61.

71.   Pileni, M. P., Nanocrystal self-assemblies: Fabrication and collective properties. *Journal of Physical Chemistry B* 2001, *105* (17), 3358-3371.

72.   Rogach, A. L.; Talapin, D. V.; Shevchenko, E. V.; Kornowski, A.; Haase, M.; Weller, H., Organization of matter on different size scales: Monodisperse nanocrystals and their superstructures. *Adv. Funct. Mater.* 2002, *12* (10), 653-664.

73.   (a) Polleux, J.; Pinna, N.; Antonietti, M.; Niederberger, M., Ligand-directed assembly of preformed titania nanocrystals into highly anisotropic nanostructures. *Adv. Mater.* 2004, *16* (5), 436-+; (b) Polleux, J.; Pinna, N.; Antonietti, M.; Hess, C.; Wild, U.; Schlogl, R.; Niederberger, M., Ligand functionality as a versatile tool to control the assembly behavior of preformed titania nanocrystals. *Chem.-Eur. J.* 2005, *11* (12), 3541-3551.

74.   da Silva, R. O.; Heiligtag, F. J.; Karnahl, M.; Junge, H.; Niederberger, M.; Wohlrab, S., Design of multicomponent aerogels and their performance in photocatalytic hydrogen production. *Catal. Today* 2015, *246*, 101-107.

75.   Dalmaschio, C. J.; Ribeiro, C.; Leite, E. R., Impact of the colloidal state on the oriented attachment growth mechanism. *Nanoscale* 2010, *2* (11), 2336-2345.

76.   (a) Whitesides, G. M.; Boncheva, M., Beyond molecules: Self-assembly of mesoscopic and macroscopic components. *Proc. Natl. Acad. Sci. U. S. A.* 2002, *99* (8), 4769-4774; (b) Gates, B. D.; Xu, Q. B.; Stewart, M.; Ryan, D.; Willson, C. G.; Whitesides, G. M., New approaches to nanofabrication: Molding, printing, and other techniques. *Chem. Rev.* 2005, *105* (4), 1171-1196.

77.   Heiligtag, F. J.; Rossell, M. D.; Suess, M. J.; Niederberger, M., Template-free co-assembly of preformed Au and TiO_2 nanoparticles into multicomponent 3D aerogels. *J. Mater. Chem.* 2011, *21* (42), 16893-16899.

2. General principles for photocatalysis based on semiconductors systems

2.1. Scope of this chapter

In this chapter the aim is to provide a critical overview analysis in terms of sunlight conversion efficiency to guide the design of semiconductors. Herein, the principles for the development and progress of photocatalysts and photoelectrodes will be described and illustrated. This includes the latest solid materials (e.g. metal oxide based systems, oxynitrides, oxysulfides) and molecular or sensitization approaches which have been used to achieve or which contributed for the understanding and advance of this challenging research field. The critical assessment in terms of efficiency will be illustrated by the use of three different design strategies employing photocatalysts[*] and photoelectrodes for solar fuel production namely (i) particulate or colloidal semiconductors (ii) Z-scheme[†] configuration and (iii) photoelectrochemical (PEC) cells, with focus on water reduction reaction, i.e. the hydrogen evolution reaction (HER).

2.2 Efficiency assessment for solar energy conversion and photocatalyst design

The theoretical limit for the efficiency of p-n junction solar converters were elaborated by Shockley and Queisser in 1961, based on the ideal photovoltaic cell concept.[1a] Their calculation reached a maximum efficiency of 30% for a single junction solar cell. The updated maximum efficiency is 33%. The analysis of sunlight composition shows the following: UV – 5% ($\lambda < 400$ nm), visible – 43% ($400 < \lambda < 800$ nm), and infrared – 52% ($800 < \lambda < 2500$ nm). Therefore, a semiconductor having a bandgap of λ_g can absorb photons only with wavelengths shorter than λ_g, whereas longer wavelengths are not absorbed. Hence, the main factors responsible for the energy losses in solar cells can be summarized as: (i) loss by long wavelengths; (ii) loss by excess energy of photons (thermalization); (iii) loss by metal electrode coverage; (iv) loss by reflection; (v) loss by incomplete absorption due to the finite thickness and (vi) loss due to recombination.[2]

In order to exceed the Shockley-Queisser limit some strategies can be adopted such as[3a,3b]: (i) employ more than one semiconductor material in a cell; (ii) promote hetero-junction structures; (iii) modification of semiconductor band structures by doping; (iv) modification of semiconductor morphology and configuration; (v) sensitization of semiconductors using dye molecules or quantum dots; (vi) addition of co-catalyst; (vii) addition of other additives such as graphene or carbon nanotubes; (viii) plasmonic assistance and (ix) concentrate the sunlight. In this way, a critical analysis

---

[*] photo-catalyst, photo-semiconductor and/or semiconductor will be used throughout this manuscript without distinction between them.
[†] This system was inspired by natural photosynthesis in green plants, which represents the energy diagram for electron transfer in the "light reaction" during photosynthesis. Also considered a PEC mechanism that uses tandem particles.

of these features can be used to guide the design of improved semiconductors achieving higher efficiencies.

In view of these facts, maximum efficiency can be calculated based on two critical factors: (i) number of semiconductor materials (photosystems) used either single (S) semiconductor or dual (D) semiconductors with different band gap values; (ii) the minimum number of absorbed photons per H_2 molecule, i.e. the use of 1, 2 or 4 photons.[1b] When these factors are taken into account, the threshold photon energy and the maximum efficiency can be calculated for all possible combinations between the semiconductor systems (S and D) and the number of absorbed photons (1, 2 and 4). According to Bolton's classification the possible solar water photolysis schemes are denoted as follow including their theoretical efficiencies: S1 - 5.3%, S2 - 30.7%, S4 - 30.6%, D2 - 42.4% and D4-41.0%[‡]. For example, considering a single semiconductor with E_g 1.6 eV or equivalent wavelength threshold of 775 nm the maximum conversion efficiency under simulated sunlight (AM 1.5G[§], 1 atm, 298 K) is nearly 31%. Thus, this system is classified as S2, which is a single band gap material with a minimum of 2 absorbed photons per H_2 molecule. The theoretical model which predicts photoconversion to chemical energy efficiency can be calculated by eq. 2.1.

$$\eta = \frac{J_g \cdot \mu_{ex} \cdot \phi_{conv}}{S}$$

(2.1)

Where: J_g accounts for the absorbed photons flux ($s^{-1}m^{-2}$), μ_{ex} is the excess chemical potential generated by light absorption, ϕ_{conv} is the quantum yield for absorbed photons and S is the total incident light irradiance (mW cm^{-2}). Hence, the critical analysis of Bolton's classification for splitting water into its molecular species sets ideal limits on their efficiencies. Moreover, for practical reasons single gap schemes can achieve up to 10% practical overall efficiency while dual band gap schemes can achieve up to 16%, after taking into account several losses (i.e. scattering, reflection, quantum yield, absorption collection losses, etc) .[1b]

To evaluate the performance of a given photocatalyst system its efficiency or photocatalytic activity in hydrogen generation can be measured directly from the amount of hydrogen gas evolved or indirectly through electron transfer from the semiconductor to water within a certain time period. However, due to different photocatalytic setup configurations, different light sources and the use of

---

[‡] For example: S1 refers to single semiconductor system absorbing only one photon; while D2 refers to a dual semiconductor system absorbing 2 photons.
[§] Air Mass Global corresponds to the vertical path the sunlight has to traverse through the atmosphere. For AM 1.5 the sunlight has to traverse 1.5 times as much as AM1 radiation.

bias assistance[**] for instance, it becomes extremely difficult to evaluate and make comparison between hydrogen evolution results reported in the literature. In heterogeneous photocatalysis (particulate semiconductors), quantum yield evaluates the number of molecules converted relative to the total number of photons incident on the reactor walls for an undefined reactor geometry and for polychromatic radiation. In fact, the quantum yield (Φ) as the concept developed for homogeneous photochemistry must express the amount (mol) of reactant consumed or product formed in the bulk phase, (n) to the amount of photons at certain wavelength (λ) absorbed by the photocatalyst, (n_{ph}) (eq. 2.2).

$$\phi_\lambda = \frac{n}{n_{ph}}$$
(2.2)

Where: n is the amount (mol) of reacted electrons or H_2 produced, while n_{ph} is the amount of absorbed photons by the photocatalyst at wavelength λ.[3c] Alternatevily, the solar energy conversion is another acceptable parameter to evaluate the light energy conversion efficiency and is defined as according to eq. 2.3.[4]

$$\eta \ (\%) = \frac{\text{Output energy as } H_2}{\text{Energy of incident sunlight}} \times 100$$
(2.3)

2.3   Classification of the solar water splitting systems

In solar water splitting, hydrogen is produced from water using sunlight and suitable photocatalysts. However there are several ways and configurations one can combine a specialized semiconductor to harvest and convert light and generate hydrogen and/or oxygen. Hence, this section will describe and classify the many pathways one can use to cleave the water molecule with the aid of a photocatalyst and light (i.e. solar spectrum or monochromatic light) as illustrated in Fig. 2.1.

The main feature which characterizes whether a system is photocatalytic particulate or photoelectrochemical (PEC) water splitting is based on the physical way the semiconductor is employed. Within particulate systems there are two configurations possible: the first is a single photocatalyst systems without proper band gap requirements which need chemical bias to generate H_2 and O_2. This approach is the most used system to investigate half reactions, in particular for hydrogen evolution. Several examples can be enumerated to illustrate this approach, i.e. TiO_2

[**] Here bias assistance can be understand as an additional energy input to the system facilitating the desired reaction, such as: optical, pressure, thermal, chemical or electrical. Chemical bias is also known as sacrificial agents or hole scavengers.

particles decorated with noble metals as co-catalyst or the usage of hole scavengers like methanol, ethanol or glycerol.[5-7]
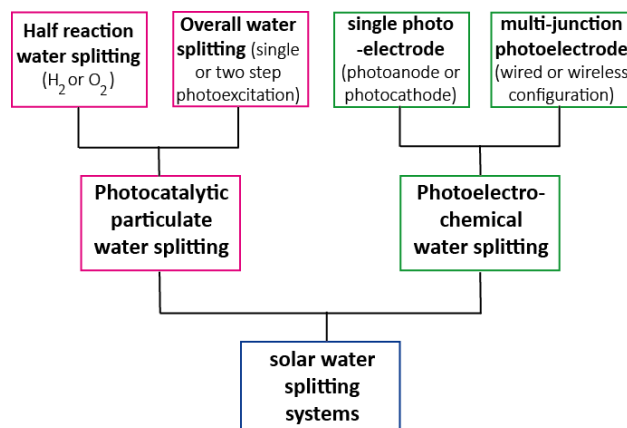
Figure 2.1 Classification scheme for water splitting systems.

Reactions that use sacrificial reagents such as methanol, ethanol, glycerol, EDTA, I^-, IO_3^- and Fe^{3+} are designated as half reactions of water splitting. These sacrificial agents are frequently employed to conduct test reactions and to establish whether a certain photocatalyst satisfies the kinetic and thermodynamic requirements for photocatalytic H_2 or O_2 evolution. Thus, achieving simultaneous oxidation and reduction of water involves a complex multistep reaction which requires four holes to each oxygen molecule or at least two electrons per hydrogen molecule produced as indicated by equations 2.5-2.7. Addionally, the use of sacrificial agents can significantly improve H_2 production by scavenging holes while the electrons are directed to co-catalyst reducing drastically in this way carrier recombination. Since methanol, ethanol or glycerol are widely used as sacrificial agents, their utilization from the environmental point of view will be relevant only if they are derived from biomass or residue waste other than from fossil sources. Furthermore, since only one gas is evolved in half-reactions the back reaction which could generate water is suppressed increasing the H_2 yield, which also obviates the need for gas separation.[8]

The second configuration (i.e. for overall water splitting) can be sub-divided into two more categories: single step photoexcitation and two step photoexcitation (z-scheme or dual-absorber tandem) system. Single step photoexcitation is based on a layered perovskite single photocatalysts such as $(BaTi_4O_9)$[9], tantalates $(KTaO_3)$[10] and $(Ga_{1-x}Zn_x)(N_{1-x}O_x)$ solid solutions[11] under UV irradiation to promote overall water splitting. Two step photoexcitation (dual photo-semiconductor) is used to comply with the band gap requirements necessary to oxidize and reduce water, such as catalyst systems composed of $Pt/ZrO_2/TaON$ and Pt/WO_3.[12]

The PEC system is divided into single photoelectrodes or multi-junction photoelectrodes. The first configuration is based on the use of a n-type single catalyst (called photoanode) and a p-type single catalyst (called phocathode). For example, titania thin films are n-type semiconductors that are

used frequently as photoanodes[13] while $CaFe_2O_4$ is a significant representative of p-type material which can be used as photocathode.[14] In contrast, the multi-junction system uses at least two different semiconductors to absorb a substancial fraction of the solar spectrum and generates sufficient free energy to promote water splitting. Nocera et al. developed a device based into a triple junction made of amorphous silicon photovoltaic interfaced to hydrogen- and oxygen-evolving catalysts made from an alloy of earth-abundant metals and a cobalt-borate catalyst operating at neutral pH conditions achieving efficiencies of approx. 5% for a wired system while 2.5% for a wireless system. [15] Fig. 2.1 summarizes these configurations aforementioned.

2.4   Basic principles of water photolysis using photocatalysts

The design of high active photocatalysts relies on understanding of the relationship between their properties and their performance. Although the comprehension of how photocatalysts work and their performance have been improved since the pioneering work from Fujishima and Honda[13] in 1972, the current knowledge is still not satisfactory to reach the proposed 10% solar to fuels efficiency. Regarding the question "How to develop high-efficient (photo)catalysts?" George M. Whitesides, one of the most influential chemists of our times, wrote in a perspective essay the following:[16] "One of the uniquely important skills of chemistry is heterogeneous catalysis. Given its pervasive importance, it is astonishing how much we still do not know about this subject… into today's universe of commodity catalysts, we still do not understand (beyond a superficial level) the mechanisms of these processes that generate fuels, chemicals, and materials". Comparably, this state of affairs is not much different for photocatalysts.
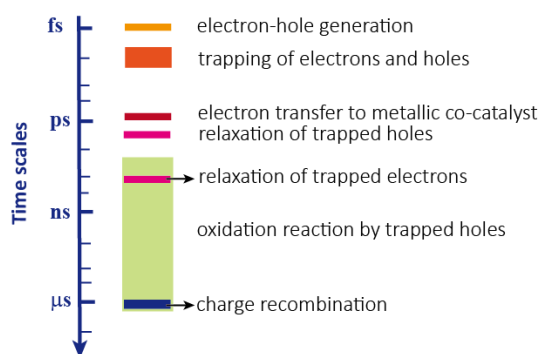
Figure 2.2 Overview of the time scales in photocatalysis. Illustration adapted from reference 17.

However, recent advances and fundamental studies of photocatalytic processes using time resolved absorption spectroscopy have contributed to the elucidation of the mobility of photogenerated charge carriers. Consequently, this allowed the stablishment of the time scales associated with ectron-hole generation, trapping, relaxation of the trapped carriers, their recombination and interface charge transfer as shown in Fig. 2.2 (usually the time ranges from a few femto to 100 micro-

seconds depending on the reaction).[18-19] Knowledge of the time scales and transport of the photo-generated charge carriers is essential to improve the overall efficiency. Moreover, it is possible to identify and tackle competing reactions in the bulk or interfacial charge transfer by fostering photocatalyst design such as noble metal deposition[7], transition metal ions doping[20], anion doping[21], sensitization[22] and semiconductor coupling.[23,24]

The process of collecting and storing solar energy into chemical bonds such as hydrogen (H_2) is known as artificial photosynthesis, because it is reminiscent of the photosynthesis performed by green plants that convert CO_2 and water into sugars and oxygen (O_2) upon irradiation with sunlight. The structures which collects and converts sunlight in plants are called a chloroplasts, they are complex and hierarchical structures composed of thylakoid membranes[††], chlorophyll pigments and carotenoids working together driven by visible light.[25] Comparably in artificial photosynthesis the structure responsible for the sunlight harvesting and conversion is known as photocatalyst. In general, semiconductors are a group of materials having conductivities between those of metals and insulators. They possess a nearly filled valence band and a nearly empty conduction band separated by a band gap (E_g).[26] The semiconductor photocatalyst concept was pioneered by Fujishima and Honda in the early 70's.[13] Since then, there is a notable growth of interest and research in photocatalysis and artificial systems that can mimic plant photosynthesis to harvest and convert solar energy into fuel. From the thermodynamic point of view, to split 1 mol or (18g) of water into its elementary O_2 and H_2 requires a change of at least 237 kJ mol^{-1} or 1.23 eV in the Gibbs free energy per mol of electrons transferred. Hence, the energy required to generate 1 mol of oxygen gas (eq. 2.5) corresponds to 4.92 eV because it involves 4 electron-hole pairs per O_2 molecule, whereas to generate 1 mol of hydrogen gas (eq. 2.6) corresponds to 2.46 eV because it requires 2 electron-hole pairs per H_2 molecule, which is in the domain of 500 nm and 250 nm respectively. The semiconductor photoexcitation and charge carriers formation, in addition to the half reactions for water splitting are described below (eq. 2.4 – 2.7).

$$\textbf{Semiconductor (SC):} \quad SC + 4\,h\nu \implies 4\,e^- + 4\,h^+ \qquad (2.4)$$

$$\textbf{Oxidation:} \quad 2\,H_2O + 4\,h^+ \longrightarrow O_2 + 4\,H^+ \qquad (2.5)$$

$$\textbf{Reduction:} \quad 4\,H^+ + 4\,e^- \longrightarrow 2\,H_2 \qquad (2.6)$$

$$\textbf{Overall Process:} \quad 2\,H_2O + 4\,h\nu \longrightarrow 2\,H_2 + O_2 \qquad (2.7)$$
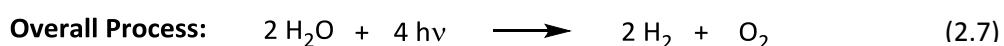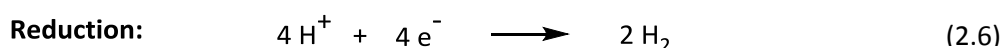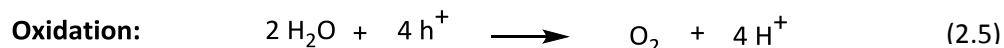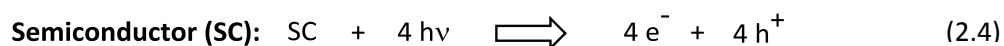
[††] The thylakoid membrane or flattened sac is a photosynthetic membrane which uses the light energy to split water into protons, electrons and oxygen.

Eq. 2.4 represents the photon conversion and electron-hole pair formation in a semiconductor photocatalyst when illuminated with photons having energies equal or larger than the semiconductor band gap (E_g). However, this reaction is not enough to explain all processes and phenomena that occur in a semiconductor while irradiated. For this purpose the band gap model (as depicted by Fig. 2.3) illustrates accordingly the principles and processes involved in a typical single semiconductor photocatalytic process. Fig. 2.3a illustrates the electronic structure of a semiconductor which is characterized by a specific band gap for each semiconductor material. The band gap is defined as the energy difference between the valence band (VB) and the conduction band (CB). Therefore the water photolysis is initiated when a semiconductor absorbs light photons with energies greater than the band gap energy. This energy absorption promotes the electrons in the valence band to the conduction band, consequently each electron promoted to the conduction band leaves back one counterpart electron hole in the valence band, or just referred as the electron (e^-) hole (h^+) pairs, as shown in Fig. 2.3(a). The semiconductor must attend essential conditions to achieve meaningful water photocatalytic decomposition such as: a) the reduction hydrogen potential of the conduction band must be more negative than the reduction potential of H^+/H_2 (0 V vs normal hydrogen electrode - NHE), whereas the valence band must be more positive than the redox potential of O_2/H_2O (1.23 V vs. NHE); b) the semiconductor photocatalyst must be stable throughout the irradiation period and c) the charge transfer through the entire semiconductor must be fast enough to prevent corrosion and/or reduce energy losses due to overvoltage or overpotential in case of PEC cells.[27]
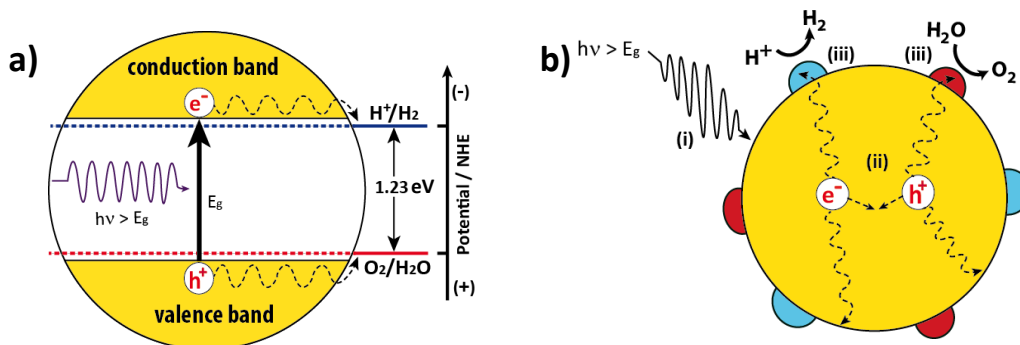
Figure 2.3 Schematic illustration of overall water splitting (a) on a single semiconductor photocatalyst, (b) main steps involved in a photocatalytic process: (i) photoexcitation and charge carriers generation, (ii) separation of excited carriers (electrons and holes) and their drift/diffusion to the catalyst surface, (iii) introduction of reduction and/or oxidation co-catalyst sites to facilitate the H_2 and O_2 evolution reactions respectively. Illustration adapted from reference 36.

In Fig. 2.3b the main processes involved in the light absorption and charge carriers formation and their diffusion through the semiconductor surface is illustrated as follows: (i) photoexcitation and charge carrier generation, (ii) separation of excited carriers (electrons and holes) and their drift/diffusion to the catalyst surface, (iii) reduction and/or oxidation on co-catalysts to facilitate the hydrogen and/or oxygen evolution reaction. Although several reviews were published in the topic of

heterogeneous photocatalysis mechanism using the energy band model (as shown in Fig. 2.2.), we still lack a great deal of understanding it. [2,4 ,9,28-35]

2.5   Design strategies for semiconductor photocatalysts

2.5.1   One step photoexcitation: Colloidal semiconductors particulate materials suspended in water

All strategies for designing a light driven photocatalyst in the field of heterogeneous photocatalysis share the same concept of band gap photoexcitation employing semiconductors. In general, there are three different design strategies for using semiconductors to generate solar fuel: (a) particulate or colloidal semiconductors; (b) Z-scheme coupled with light absorbing units for reduction and oxidation reactions and (c) semiconductor photoelectrochemical cells (PEC) for water photolysis, as illustrated in Fig. 2.4.

The first approach is based on a single particulate or colloidal semiconductor suspended in water under light irradiation (absorbing two photons to produce one H_2, denominated S2 approach) , as depicted in Fig. 2.3a. This system offers advantages like simplicity, scalability, high extinction coefficients, fast charge carriers diffusion path to reach the interface and the possibility to modify the semiconductor particle surface by co-catalyst deposition, functionalization or adsorption of species which can facilitate the charge carrier separation resulting in improved solar fuels generation. As a drawback this system generates in a single compartment vessel a potential explosive mixture of hydrogen and oxygen, demanding additional gas dilution with inert gas and their separation in a further step for safety reason.
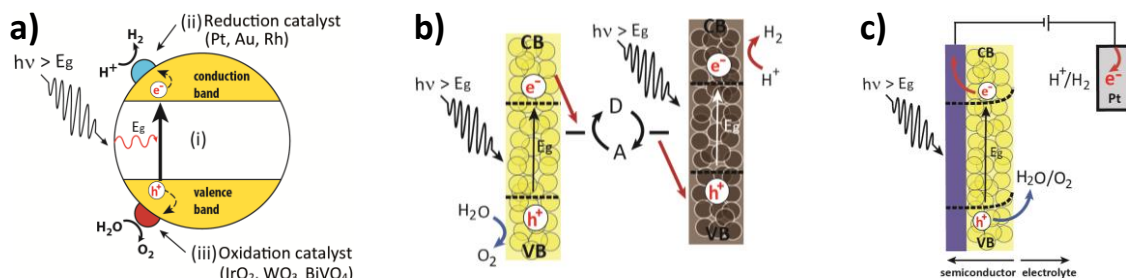
Figure 2.4 Summary of photocatalytic semiconductor strategies applied to water splitting (a) particulate or colloidal semiconductor, (b) Z-scheme or tandem configuration with a two-step photoexcitation system in the presence of a redox mediator, (c) photoanode immobilized into a conductive substrate to promote water splitting in a (photo)electrochemical cell.

The most successful particulate materials tested according to the system in Fig. 2.4a can be divided into two categories: (a) visible light active materials such as oxynitride, sulphide or selenide photocatalysts for instance: gallium nitride-zinc oxide solid solution (GaN-ZnO) loaded with RuO_2 co-catalyst is one of the singular compound systems able to promote overall water splitting without using a sacrificial agent under visible light irradiation, reported by Domen;[37] CdS loaded with Pt-PdS

23

as cocatalyst and sulphide/sulfite couple as sacrificial agent reported by Yan et al.;[38] cadmium sulphide incorporated into a titanium based mesoporous MCM-48 support (CdS-Ti-MCM-48) with RuO_2 used as co-catalyst and ethanol as sacrificial agent according to Peng et al.;[39] and a system denominated by their authors as "multicomponent nanoheterostructured platinum-tipped cadmium sulfide rod with an embedded cadmium selenide seed" shortly (CdS-CdSe) used together with Pt nanoparticles as co-catalyst and methanol as sacrificial agent reported by Alivisatos and Amirav[40]; (b) UV-active materials mainly metal oxides such as tantalates and titania: Sodium tantalate mesocrystals doped with strontium were prepared by Sun et al. and used as photocatalyst in the presence of methanol as hole scavanger obtaining high yields for hydrogen photocatalytic reaction.[41] The so-called black titania (disorder-engineered nanocrystal with dopant incorporation obtained after the hydrogenation of TiO_2) was developed by Chen et al. to improve the visible light absorption of TiO_2. The titania absorption coefficient was slightly enhanced when irradiating the material under visible light and using Pt as co-catalyst and methanol as hole scavenger, however, when using the same system under UV light, an enhancement of nearly 100 times were achieved.[42] The main obstacles in the development of colloidal or particulate materials driven by one-step photoexcitation is related to the lack of compounds which possess band gaps narrower than 3 eV. Photo semiconductor band-edges must encompass the reduction and oxidation potential of H_2 and O_2, in addition to being stable throughout the photocatalytic reaction.

2.5.2   Two step photoexcitation: Z-scheme or dual absorber tandem cell

Each semiconductor has its characteristic band structure with a distinct band gap, which allows it to absorb light of different wavelengths, and to separate and transfer charges to the semiconductor surface or to an interface. The concept of using a single semiconductor absorber requires a semiconductor with a wide band gap to exploit a significant part of the solar spectrum.[27] Some of the obstacles mentioned for the development of particulate semiconductor materials can be addressed by using multiple semiconductors in Z-scheme or tandem cells. The tandem cell uses a dual absorber semiconductor and four photons are involved (so called D4 scheme), as illustrated in Figure 2.4b.[1b] This dual semiconductor configuration (used as particulate photocatalyst) was reported by many reports and in the best case a quantum yield (%) of 6.3 under visible light irradiation (420-800 nm) was achieved with $SrTiO_3$:Rh/$BiVO_4$ as light absorber.[43]

The Z-scheme system mimicks the natural photosynthesis system and it is composed of a semiconductor-semiconductor junction. This junction is a result of band structure alignment between the two semiconductors, such as a p-n junction.[26] However, in the Z-scheme or tandem configuration it is possible to combine the VB of one semiconductor with the CB of another, in order to cover the

water redox potential requirements to achieve overall water splitting, as shown in Figs. 2.4b and 2.5. In one example, $SrTiO_3$:Rh is the unit responsible for H_2 reduction while $BiVO_4$ is the unit responsible for oxygen oxidation.[43] In this configuration the charge transfer occurs in the following manner: the photogenerated electrons from the semiconductor with the lower CB edge can recombine with the holes in the semiconductor with the higher VB edge resulting in a net surplus of holes in the semiconductor with lower VB edge, and in an electron surplus in the semiconductor with the higher CB edge (as illustrated by Fig. 2.4b and the energy diagram in Fig. 2.5). Consequently, the hole and electron surpluses can be used to direct oxidation and reduction by combining half-reactions at completely different sites.
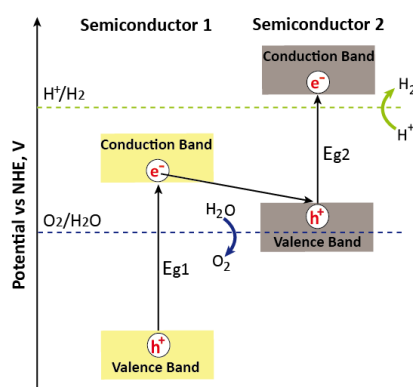
Figure 2.5 Energy diagram scheme of two-step photoexcitation approach (Z-scheme) used in photocatalytic water photolysis. Represented by the contact in between two distinct semiconductors.

Thus, the main advantage of using dual a semiconductor system in comparison with single particulate system, consists of promoting a broader and more efficient absorption of solar spectrum, in addition it may allow the full photospliting of water to be achieved. The main drawback of the two-step photoexcitation systems is the two-fold number of photons in comparison with one-step systems. Also, depending on the tandem configuration an additional electron mediator pair (usually Fe^{2+}/Fe^{3+} or IO_3^-/I^- is used) is required to mediate the charge transport in between the two semiconductors according to Fig. 2.4b. The backward reactions between electron acceptor (A) and electron donor (D) over the photocatalyst may reduce the amount of H_2 and O_2 produced.

2.5.3 Photoelectrochemical water splitting based on thin film electrodes

The last strategy to be discussed consists of a photo-active semiconducting thin layer materials (n- or p-type) coupled with a counter electrode made of either metallic platinum or another semiconductor, which are immersed in an electrolyte solution. The assembly of these components into a single device is called (photo)electrochemical cell as illustrated in Fig. 2.4c. The photoelectrode configuration may vary, depending on the kind of semiconductor used (n- or p-type), or whether dyes or quantum dots are employed as sensitizers to inject electrons into the

semiconductor's conduction band, or whether two or more semiconductors are connected in series (multi-junction electrodes) in order to obtain a tandem cell, as shown in Fig. 2.6.

Semiconductors based on electrode thin-films, possess the advantage of generating gases in different compartments. The electrical bias can be applied to compensate the band gap requirements for oxidation and/or reduction potentials. In addition, higher efficiencies can be reached when the tandem configuration is used instead of single semiconductor.

The charge carrier separation in photoelectrochemical cells is mainly attributed to the electric field induced by space charge layer (also known as depletion layer) at the semiconductor liquid electrolyte interface (junction) as described by Gerischer.[44] In order to equilibrate this potential difference, charge transfer takes place between the surface and the bulk of the semiconductor material. As a consequence of these charge transfer, the accumulation of electrons on the semiconductor surface leads to upward band bending, whereas excessive holes on the surface would bend the bands downward. Hence, this electrical field generated in the space charge layer is the driving force responsible for photocurrents and photovoltages at semiconductor electrodes which resembles the p-n-junctions. However, the effectiveness of this semiconcuntor-electrolyte interface to separate charge carriers is influenced by the material used as electrode, doping, particle size, morphology and the use of overpotential as reviewed recently.[45] In the n-type photo-semiconductor configuration or the so-called photoanode (Fig. 2.4c) it is possible to generate one H_2 molecule from one water molecule by absorbing 2 photons (i.e. S2 scheme).[1b] Thus, one-step excitation can be applied to PEC cells. They are classified into 3 types: (i) photoanodes made of n-type semiconductors such as TiO_2;[13] (ii) photocathodes made of p-type semiconductor like $CaFe_2O_4$[14] and (iii) n- or p-type semiconductors sensitized by a molecular dye[46] or quantum dots.[47] Upon irradiation of a semiconductor while immersed in an electrolyte solution, its photoexcited electrons are shuttled through an external circuit to the counter electrode (Pt), where it can drive a redox reaction such as proton (H^+) reduction, while the holes migrate to the photoanode surface to oxidize water to O_2 (Fig. 2.4c). In the p-type photo-semiconductor water is oxidized at the counter electrode and reduced at the surface of the semiconductor (Fig. 2.6a).[‡‡] The sensitized semiconductor system was reported by Tributsch et al.,[46a] in order to address the large band gap and to extend the solar spectrum utilization. Dye sensitization of a semiconductor can be defined as the process by which the excitation of a chromophore, herein referred to as a dye or sensitizer, is followed by interfacial electron transfer, or electron injection, into the semiconductor.[48] In more detail, first photons excite the dye from the ground (D/D^+) into an excited state (D^*), then the excited electron is transferred into the TiO_2 conduction band (so called charge injection) and the oxidized dye is regenerated by mediator species

---

[‡‡] positive holes are the mobile charge carriers in p-type semiconductors.

in the electrolyte (donor/acceptor redox pair). Several studies demonstrated the fundamentals and mechanism of photosensitization as an effective strategy for populating the conduction band of wide band gap semiconductors with electrons under visible light irradiation as shown in Fig. 2.6b.[49] Normally, single photoanode or photocathode operations are restricted to external bias assistance, such as electrical bias applied by external voltage between the photoelectrode and the counter electrode or chemical bias (i.e. pH). Ovepotential is required to promote better charge separation in the photo-anode or -cathode, even in the case a semiconductor possesses the suitable band gap requirements to oxidize or reduce water. This overpotential is mainly applied to overcome the resistance generated by the electrodes immersed in the electrolyte and also to compensate the potential deficiency of the semiconductor to drive redox reactions as a result of undesirable Fermi level and band mismatch.[50]

Alternatively, the two-step photoexcitation using thin-film electrodes are another promising method to generate fuels from solar energy. Hence, dual absorber semiconductors and four photons (D4 scheme) approaches can be applied as photoanodes/photocathodes or photoelectrodes/photovoltaic configurations as reported by Graetzel et al..[24] The scheme for a photoanode/photocathode connection is illustrated in Figure 2.6c. In this configuration, two semiconductor band gaps (E_{g1} and E_{g2}) absorb complementary fractions of the solar spectrum. Additionally, more absorbers can be added to the system at the expense of increasing the complexity and possible fabrication costs.[51]
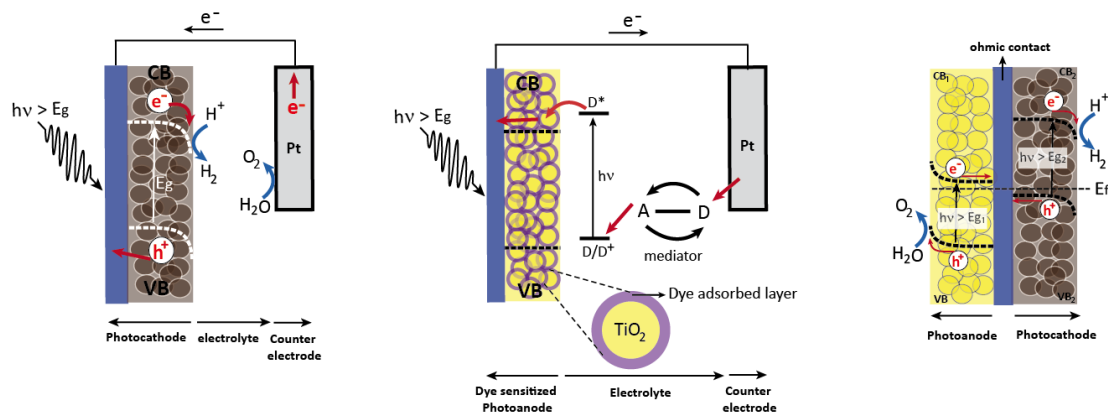
Figure 2.6 Schematic illustration of the mode of action of photoelectrochemical water splitting based on (a) one step excitation type-p semiconductor (photocathode), (b) dye sensitized electrochemical cell (sensitized photoanode) and (c) semiconductor-semiconductor all solid state Z-scheme or photoanode and photocathode in tandem. (Legend: A= acceptor, D= donor); Inset in figure (b) TiO_2 particle is zoomed in to show the dye adsorbed over the titania surface, which is responsible for the sensitization effect.

Recently several semiconductors in dual absorber tandem configurations with enhanced photocatalytic activity for overall water splitting have been reported by Brillet et. al.[24], Shi et. al.[52] and Li et. al..[53] Brillet et al. developed a simple tandem architecture between single-photoanode (Fe_2O_3 or WO_3 with E_g of 2.1 and 2.6 eV respectively) coupled with a single-dye sensitized solar cell

(DSC), where the device is stacked in a way that the incident light reaches the photoanode before the photovoltaic cell (i.e. first the visible light is absorbed by the low band gap hematite or WO_3 and the remaining UV is absorbed by the DSC composed of sensitized TiO_2). The results are encouraging, reaching photocurrents of 0.95 mAcm^{-2} for Fe_2O_3/DSC and 2.52 mAcm^{-2} for WO_3/DSC respectively or efficiencies (η) of 1.17% (hematite) and 3.10% (WO_3).[24] While in the work from Shi et al. the same concept and architecture was used as reported by Brillet with slightly modifications in the photoanode such as $BiVO_4$-sensitised mesoporous WO_3 films. Instead of using the conventional organic dye (ruthenium complex) authors have chosen to use a porphyrin-dye-based which resulted in photocurrents of 4.7 mAcm^{-2} and efficiency (η) of approx. 6%.[52] In the report from Li et. al. another innovative approach was described employing metal oxides (TiO_2 and NiO) as materials for photoelectrodes coupled with an organic dye and a homogeneous catalyst (ruthenium and cobalt complexes). Briefly their system consists of mesoporous TiO_2 as photoanode, co-sensitized by the organic dye and a ruthenium molecular catalyst while the photocathode was made of nanoscale NiO and also co-sensitized by an organic dye coupled to a cobalt catalyst reaching a current of aprox. 300 μAcm^{-2} or an efficiency output (η) of 0.05% under neutral pH, visible light and free electrical bias.[53] Therefore, the charge separation strategy based in the semiconductor-electrolyte interface can lead to relative high photocurrents or solar to hydrogen efficiencies, however to reach the goal of at least 10% efficiency[54], alternative approaches to improve devices performance such as novel compositions, architectures, optimized co-catalysts, anchoring of homogeneous catalysts for enhancing surface rates and improvementa of carrier lifetimes are still necessary.

2.6   References

1.   (a) Shockley, W.; Queisser, H. J., Detailed Balance Limit of Efficiency of p-n Junction Solar Cells. *Journal of Applied Physics* **1961,** *32* (3), 510-519; (b) Bolton, J. R., Solar Fuels. *Science* **1978,** *202* (4369), 705-711; (c) Bolton, J. R.; Strickler, S. J.; Connolly, J. S., Limiting and realizable efficiencies of solar photolysis of water. *Nature* **1985,** *316* (6028), 495-500.

2.   (a) Bard, A. J.; Fox, M. A., Artificial photosynthesis - Solar splitting of water to hydrogen and oxygen. *Accounts Chem. Res.* **1995,** *28* (3), 141-145; (b) Dhankhar, M.; Pal Singh, O.; Singh, V. N., Physical principles of losses in thin film solar cells and efficiency enhancement methods. *Renewable and Sustainable Energy Reviews* **2014,** *40*, 214-223.

3.   (a) Chen, H. M.; Chen, C. K.; Liu, R.-S.; Zhang, L.; Zhang, J.; Wilkinson, D. P., Nano-architecture and material designs for water splitting photoelectrodes. *Chem. Soc. Rev.* **2012,** *41* (17), 5654-5671; (b) Bai, S.; Jiang, J.; Zhang, Q.; Xiong, Y., Steering charge kinetics in photocatalysis: intersection of materials syntheses, characterization techniques and theoretical simulations. *Chem. Soc. Rev.* **2015,** *44* (10), 2893-2939; (c) Serpone, N.; Salinaro, A., Terminology, relative photonic efficiencies and quantum yields in heterogeneous photocatalysis. Part I: Suggested protocol (technical report). *Pure and Applied Chemistry* **1999,** *71* (2), 303-320.

4.   Kudo, A.; Miseki, Y., Heterogeneous photocatalyst materials for water splitting. *Chem. Soc. Rev.* **2009,** *38* (1), 253-278.

5.   Kawai, T.; Sakata, T., Photocatalytic hydrogen production from liquid methanol and water *J. Chem. Soc.-Chem. Commun.* **1980,** (15), 694-695.

6.   Kanno, H.; Yamamoto, Y.; Harada, H., TiO_2 based photocatalysts prepared from titanium isopropoxide and aqueous electrolyte solutions. *Chemical Physics Letters* **1985,** *121* (3), 245-248.

7.   Su, R.; Tiruvalam, R.; Logsdail, A. J.; He, Q.; Downing, C. A.; Jensen, M. T.; Dimitratos, N.; Kesavan, L.; Wells, P. P.; Bechstein, R.; Jensen, H. H.; Wendt, S.; Catlow, C. R. A.; Kiely, C. J.; Hutchings, G. J.; Besenbacher, F., Designer Titania-Supported Au-Pd Nanoparticles for Efficient Photocatalytic Hydrogen Production. *ACS Nano* **2014,** *8* (4), 3490-3497.

8.   Schneider, J.; Bahnemann, D. W., Undesired Role of Sacrificial Reagents in Photocatalysis. *The Journal of Physical Chemistry Letters* **2013,** *4* (20), 3479-3483.

9.   Takata, T.; Tanaka, A.; Hara, M.; Kondo, J. N.; Domen, K., Recent progress of photocatalysts for overall water splitting. *Catal. Today* **1998,** *44* (1-4), 17-26.

10.   Shimizu, K.-i.; Tsuji, Y.; Hatamachi, T.; Toda, K.; Kodama, T.; Sato, M.; Kitayama, Y., Photocatalytic water splitting on hydrated layered perovskite tantalate $A_2SrTa_2O_7 \cdot nH_2O$ (A = H, K, and Rb). *Phys. Chem. Chem. Phys.* **2004,** *6* (5), 1064-1069.

11.   Maeda, K.; Teramura, K.; Takata, T.; Hara, M.; Saito, N.; Toda, K.; Inoue, Y.; Kobayashi, H.; Domen, K., Overall water splitting on $(Ga_{1-x}Zn_x)(N_{1-x}O_x)$ solid solution photocatalyst: Relationship between physical properties and photocatalytic activity. *Journal of Physical Chemistry B* **2005,** *109* (43), 20504-20510.

12.   Maeda, K.; Higashi, M.; Lu, D.; Abe, R.; Domen, K., Efficient Nonsacrificial Water Splitting through Two-Step Photoexcitation by Visible Light using a Modified Oxynitride as a Hydrogen Evolution Photocatalyst. *J. Am. Chem. Soc.* **2010,** *132* (16), 5858-5868.

13.   Fujishima, A.; Honda, K., Electrochemical Photolysis of Water at a Semiconductor Electrode. *Nature* **1972,** *238* (5358), 37-38.

14.   Ida, S.; Yamada, K.; Matsunaga, T.; Hagiwara, H.; Matsumoto, Y.; Ishihara, T., Preparation of p-Type $CaFe_2O_4$ Photocathodes for Producing Hydrogen from Water. *J. Am. Chem. Soc.* **2010,** *132* (49), 17343-17345.

15.   Reece, S. Y.; Hamel, J. A.; Sung, K.; Jarvi, T. D.; Esswein, A. J.; Pijpers, J. J. H.; Nocera, D. G., Wireless Solar Water Splitting Using Silicon-Based Semiconductors and Earth-Abundant Catalysts. *Science* **2011,** *334* (6056), 645-648.

16.   Whitesides, G. M., Reinventing Chemistry. *Angewandte Chemie International Edition* **2015,** *54* (11), 3196-3209.

17.   Fujishima, A.; Zhang, X.; Tryk, D. A., TiO_2 photocatalysis and related surface phenomena. *Surf. Sci. Rep.* **2008,** *63* (12), 515-582.

18.   Iwata, K.; Takaya, T.; Hamaguchi, H.-o.; Yamakata, A.; Ishibashi, T.-a.; Onishi, H.; Kuroda, H., Carrier Dynamics in TiO_2 and Pt/TiO_2 Powders Observed by Femtosecond Time-Resolved Near-Infrared Spectroscopy at a Spectral Region of 0.9–1.5 μm with the Direct Absorption Method. *The Journal of Physical Chemistry B* **2004,** *108* (52), 20233-20239.

19.   Tamaki, Y.; Hara, K.; Katoh, R.; Tachiya, M.; Furube, A., Femtosecond Visible-to-IR Spectroscopy of TiO_2 Nanocrystalline Films: Elucidation of the Electron Mobility before Deep Trapping†. *The Journal of Physical Chemistry C* **2009,** *113* (27), 11741-11746.

20.   Choi, J.; Park, H.; Hoffmann, M. R., Effects of Single Metal-Ion Doping on the Visible-Light Photoreactivity of TiO_2. *J. Phys. Chem. C* **2010,** *114* (2), 783-792.

21.   Ni, M.; Leung, M. K. H.; Leung, D. Y. C.; Sumathy, K., A review and recent developments in photocatalytic water-splitting using TiO_2 for hydrogen production. *Renewable & Sustainable Energy Reviews* **2007,** *11* (3), 401-425.

22.   Dhanalakshmi, K. B.; Latha, S.; Anandan, S.; Maruthamuthu, P., Dye sensitized hydrogen evolution from water. *Int. J. Hydrog. Energy* **2001,** *26* (7), 669-674.

23.   Narayanan, R.; Deepa, M.; Srivastava, A. K., Nanoscale connectivity in a TiO_2/CdSe quantum dots/functionalized graphene oxide nanosheets/Au nanoparticles composite for enhanced photoelectrochemical solar cell performance. *Phys. Chem. Chem. Phys.* **2012,** *14* (2), 767-778.

24.   Brillet, J.; Yum, J. H.; Cornuz, M.; Hisatomi, T.; Solarska, R.; Augustynski, J.; Graetzel, M.; Sivula, K., Highly efficient water splitting by a dual-absorber tandem cell. *Nat. Photonics* **2012,** *6* (12), 823-827.

25.   Whitmarsh, J.; Govindjee, The Photosynthetic Process. In *Concepts in Photobiology*, Singhal, G. S.; Renger, G.; Sopory, S. K.; Irrgang, K. D.; Govindjee, Eds. Springer Netherlands: 1999; pp 11-51.

26.   Sze, S. M.; Ng, K. K., *Physics of semiconductor devices*. Wiley-Interscience: Hoboken, N.J., 2007.

27.   Walter, M. G.; Warren, E. L.; McKone, J. R.; Boettcher, S. W.; Mi, Q.; Santori, E. A.; Lewis, N. S., Solar Water Splitting Cells. *Chem. Rev.* **2010,** *110* (11), 6446-6473.

28.   Graetzel, M., Artificial photosynthesis: water cleavage into hydrogen and oxygen by visible light. *Accounts Chem. Res.* **1981,** *14* (12), 376-384.

29.   Bard, A. J., Design of semiconductor photo-electrochemical systems for solar energy conversion. *J Phys Chem-Us* **1982,** *86* (2), 172-177.

30.   Fox, M. A.; Dulay, M. T., Heterogeneous Photocatalysis *Chem. Rev.* **1993,** *93* (1), 341-357.

31.   Navarro Yerga, R. M.; Alvarez Galvan, M. C.; del Valle, F.; Villoria de la Mano, J. A.; Fierro, J. L. G., Water Splitting on Semiconductor Catalysts under Visible-Light Irradiation. *Chemsuschem* **2009,** *2* (6), 471-485.

32.   Maeda, K., Photocatalytic water splitting using semiconductor particles: History and recent developments. *Journal of Photochemistry and Photobiology C-Photochemistry Reviews* **2011,** *12* (4), 237-268.

33.   Chen, X.; Shen, S.; Guo, L.; Mao, S. S., Semiconductor-based Photocatalytic Hydrogen Generation. *Chem. Rev.* **2010,** *110* (11), 6503-6570.

34.   Kisch, H., Semiconductor PhotocatalysisMechanistic and Synthetic Aspects. *Angew. Chem.-Int. Edit.* **2013,** *52* (3), 812-847.

35.   Osterloh, F. E., Inorganic nanostructures for photoelectrochemical and photocatalytic water splitting. *Chem. Soc. Rev.* **2013,** *42* (6), 2294-2320.

36.   Qu, Y.; Duan, X., Progress, challenge and perspective of heterogeneous photocatalysts. *Chem. Soc. Rev.* **2013,** *42* (7), 2568-2580.

37.   Maeda, K.; Domen, K., New non-oxide photocatalysts designed for overall water splitting under visible light. *J. Phys. Chem. C* **2007,** *111* (22), 7851-7861.

38.   Yan, H.; Yang, J.; Ma, G.; Wu, G.; Zong, X.; Lei, Z.; Shi, J.; Li, C., Visible-light-driven hydrogen production with extremely high quantum efficiency on Pt–PdS/CdS photocatalyst. *J Catal* **2009,** *266* (2), 165-168.

39.   Peng, R.; Wu, C.-M.; Baltrusaitis, J.; Dimitrijevic, N. M.; Rajh, T.; Koodali, R. T., Ultra-stable CdS incorporated Ti-MCM-48 mesoporous materials for efficient photocatalytic decomposition of water under visible light illumination. *Chem. Commun.* **2013,** *49* (31), 3221-3223.

40.   Amirav, L.; Alivisatos, A. P., Photocatalytic Hydrogen Production with Tunable Nanorod Heterostructures. *The Journal of Physical Chemistry Letters* **2010,** *1* (7), 1051-1054.

41.   Sun, J.; Chen, G.; Pei, J.; Jin, R.; Wang, Q.; Guang, X., A simple approach to strontium sodium tantalite mesocrystals with ultra-high photocatalytic properties for water splitting. *J. Mater. Chem.* **2012,** *22* (12), 5609-5614.

42.   Chen, X. B.; Liu, L.; Yu, P. Y.; Mao, S. S., Increasing Solar Absorption for Photocatalysis with Black Hydrogenated Titanium Dioxide Nanocrystals. *Science* **2011,** *331* (6018), 746-750.

43.   Sasaki, Y.; Nemoto, H.; Saito, K.; Kudo, A., Solar Water Splitting Using Powdered Photocatalysts Driven by Z-Schematic Interparticle Electron Transfer without an Electron Mediator. *J. Phys. Chem. C* **2009,** *113* (40), 17536-17542.

44.   Gerischer, H., Electrochemical photo and solar cells principles and some experiments. *Journal of Electroanalytical Chemistry and Interfacial Electrochemistry* **1975,** *58* (1), 263-274.

45.   Fabian, D. M.; Hu, S.; Singh, N.; Houle, F. A.; Hisatomi, T.; Domen, K.; Osterloh, F. E.; Ardo, S., Particle suspension reactors and materials for solar-driven water splitting. *Energy Environ. Sci.* **2015,** *8* (10), 2825-2850.

46.   (a) Tributsch, H.; Calvin, M., Electrochemistry of excited molecules: Photo-electrochemical reactions of chlorophylls* *Photochemistry and Photobiology* **1971,** *14* (2), 95-112; (b) Desilvestro, J.; Graetzel, M.; Kavan, L.; Moser, J.; Augustynski, J., Highly efficient sensitization of titanium dioxide. *J. Am. Chem. Soc.* **1985,** *107* (10), 2988-2990.

47.   (a) Lee, Y.-L.; Chi, C.-F.; Liau, S.-Y., CdS/CdSe Co-Sensitized TiO$_2$ Photoelectrode for Efficient Hydrogen Generation in a Photoelectrochemical Cell. *Chem. Mat.* **2010,** *22* (3), 922-927; (b) Yu, J.; Zhang, J.; Jaroniec, M., Preparation and enhanced visible-light photocatalytic H$_2$-production activity of CdS quantum dots-sensitized Zn1-xCdxS solid solution. *Green Chemistry* **2010,** *12* (9), 1611-1614.

48.   Watson, D. F.; Meyer, G. J., Electron injection at dye-sensitized semiconductor electrodes. In *Annual Review of Physical Chemistry*, Annual Reviews: Palo Alto, 2005; Vol. 56, pp 119-156.

49.   (a) Gerischer, H., Electrochemical techniques for the study of photosensitization*. *Photochemistry and Photobiology* **1972,** *16* (4), 243-260; (b) Memming, R.; Tributsch, H., Electrochemical investigations on the spectral sensitization of gallium phosphide electrodes. *The Journal of Physical Chemistry* **1971,** *75* (4), 562-570; (c) Memming, R., Electron transfer reactions of excited ruthenium(II) complexes at semiconductor electrodes. *Surface Science* **1980,** *101* (1–3), 551-563.

50.   Hisatomi, T.; Kubota, J.; Domen, K., Recent advances in semiconductors for photocatalytic and photoelectrochemical water splitting. *Chem. Soc. Rev.* **2014,** *43* (22), 7520-7535.

51.   Sivula, K., Metal Oxide Photoelectrodes for Solar Fuel Production, Surface Traps, and Catalysis. *The Journal of Physical Chemistry Letters* **2013,** *4* (10), 1624-1633.

52.   Shi, X.; Zhang, K.; Shin, K.; Ma, M.; Kwon, J.; Choi, I. T.; Kim, J. K.; Kim, H. K.; Wang, D. H.; Park, J. H., Unassisted photoelectrochemical water splitting beyond 5.7% solar-to-hydrogen conversion efficiency by a wireless monolithic photoanode/dye-sensitised solar cell tandem device. *Nano Energy* **2015,** *13*, 182-191.

53.   Li, F. S.; Fan, K.; Xu, B.; Gabrielsson, E.; Daniel, Q.; Li, L.; Sun, L. C., Organic Dye-Sensitized Tandem Photoelectrochemical Cell for Light Driven Total Water Splitting. *J. Am. Chem. Soc.* **2015,** *137* (28), 9153-9159.

54.   Lewis, N. S.; Crabtree, G.; Nozik, A. J.; Wasielewski, M. R.; Alivisatos, P.; Kung, H.; Tsao, J.; Chandler, E.; Walukiewicz, W.; Spitler, M.; Ellingson, R.; Overend, R.; Mazer, J.; Gress, M.; Horwitz, J.; Ashton, C.; Herndon, B.; Shapard, L.; Nault, R. M. *Basic Research Needs for Solar Energy Utilization. Report of the Basic Energy Sciences Workshop on Solar Energy Utilization, April 18-21, 2005*; 2005; p Medium: ED.

3. Chemically produced graphene as an additive to improve H$_2$ generation

3.1 Scope of this chapter

The results described in this chapter had as aim the improvement of the H$_2$ generation of an oxidic semiconductor by using i) an attached co-catalyst and ii) graphene oxide in a simple solution mixture[*]. The idea behind this is based on excellent physical properties of graphene, which is a two-dimensional single layer of carbon atoms densely packed in a honeycomb crystal lattice, such as high charge carrier mobility and large surface area. Therefore, mixing the photosemiconductor (PS) in the presence of a co-catalyst, such as metallic nanoparticles (MNP) together with graphene layers may enhance the reaction activity and selectivity. Fig. 3.1 illustrates the photosemiconductor and metallic nanoparticles in the interplay with graphene as composite during the water splitting reaction. The semiconductor is excited by light irradiation consequently generating the electron-hole pairs. The graphene sheet may capture and shuttle the electrons across the two-dimensional conductive carbon network to the metallic nanoparticle sites, facilitating in this way the hydrogen evolution. Similar concepts were demonstrated earlier by several groups.[1-3] For instance, a ternary composite consisting of graphene nanosheets with CdS clusters with Pt 0.5 wt.% as co-catalyst was used as photocatalyst to generate hydrogen under visible light irradiation (420 nm). The authors achieved a hydrogen production rate of 1.12 mmolh^{-1} with a loading of 1.0 wt.% of reduced graphene oxide while the pure cadmium sulphide showed a hydrogen production rate of only 230 μmolh^{-1}.[1a] Similar approach was used by M. Jaroniec et al. employing a ternary TiO$_2$-graphene-MoS$_2$ composite photocatalyst containing a layered MoS$_2$/graphene.[3] The composite photocatalyst showed a hydrogen evolution rate of around 37 μmolh^{-1} for the TiO$_2$-MoS$_2$ composite, while 165 μmolh^{-1} of hydrogen were produced on the TiO$_2$-graphene-MoS$_2$ composite with 0.5 wt.% graphene loading under UV-vis irradiation (365 nm). These results were attributed to the synergistic effects between all components, in addition to the high charge carrier mobility of the chemically produced graphene.[3]

In this work a dedicated semiconductor synthesis for an easy available multilayer reduced graphene oxide (m-rGO) was developed. Sodium tantalate (NaTaO$_3$) was used as the photosemiconductor. This material has been extensively investigated earlier due to its very active photocatalytic properties.[4-6] Gold metallic nanoparticles (Au-MNP) were used as co-catalysts or reduction sites by photodeposition on NaTaO$_3$/m-rGO in the solution mixture[*]. Therefore, the current work describes the combination of 3 components that should lead to an enhancement of activity, as a result of Au-MNP and m-rGO interplay with NaTaO$_3$ photo-semiconductor. Here, the synthesis and performance of this new material is described, as well as its behaviour under photocatalytic conditions employing in situ EPR spectroscopy.[7]

---

[*] Solution mixture: The term is used to determine the simple mixture of the components dispersed in water-methanol solution.
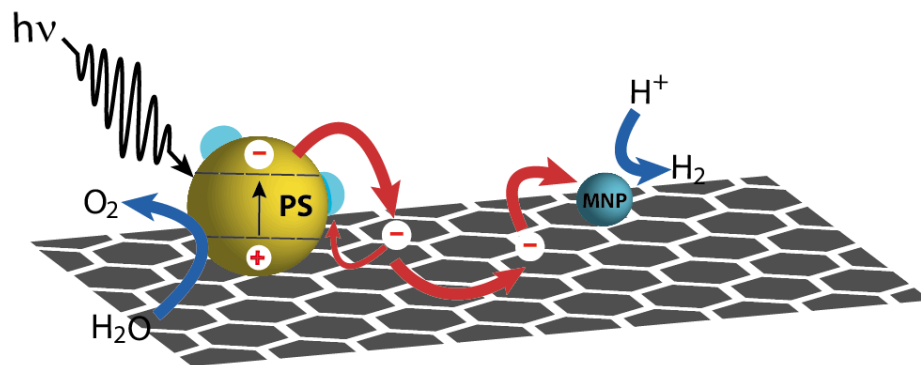
Figure 3.1 Scheme showing the advantage of employing graphene as 2-D support for incorporating photo-semiconductor (PS) and a metallic nanoparticle (MNP) in water splitting reaction.

3.2 Tantalates applied to photocatalysis and their synthetic routes

Materials with a perovskite structure (as illustrated in Fig. 3.2) are well known for their interesting properties such as colossal magnetoresistance[8], ferroelectricity[9], superconductivity[10]; in addition they are used as heterogeneous catalysis.[11] Within the field of heterogeneous catalytic processes that employ perovskite-like structures the following are worth to mention: NO_x, CO and CH_4 oxidation and catalytic reforming of hydrocarbons.[11] Furthermore, perovskite-like structures achieved remarkable activity in the field of heterogeneous photocatalytic water splitting for hydrogen and oxygen production.[5] Tantalate compounds are a class of materials composed in most of the cases of TaO_3^- anions that can be combined with a broad variety of metal cations. The resulting compounds can be classified in the following way: alkali tantalates ($ATaO_3$)[12], alkaline earth tantalates (BTa_2O_6[13,14], $B_2Ta_2O_7$[15]), mixed alkali-alkaline earth tantalates ($A_2BTa_2O_7$[16] $AB_2Ta_3O_{10}$[17,18]), [where A= Li, Na, K, Rb and B = Ca, Sr, Ba]. Besides all tantalates aforementioned, it is also possible to find in the literature solid solutions of tantalates combined with transition metals (such as Nb, Zr or Hf), rare earths (La, Sm or Nd) and other elements (such as Bi, Sn or Si) as reported by some excellent reviews on this topic.[19-23] Several of these crystalline tantalate compounds exhibit the perovskite-like structure (Fig. 3.2). So far, alkali tantalates such as $NaTaO_3$ have been used as photocatalysts for overall water splitting; they exhibited one of the highest activities among tantalates, however due to their wide band gap tantalates are restricted to UV irradiation.[20] This high photocatalytic activity of tantalates may be attributed to the structure that provides specific sites for the reduction and oxidation reactions; consequently, in this arrangement the charge recombination is low.[5] Therefore, tantalum oxides and their mixed oxides may play a pivotal role in the field of photocatalysis serving either as photocatalysts or semiconductor surface platforms to anchor homogeneous active catalysts as recently reported by the Cowan group, in order to further enhance photocatalytic performance.[24]
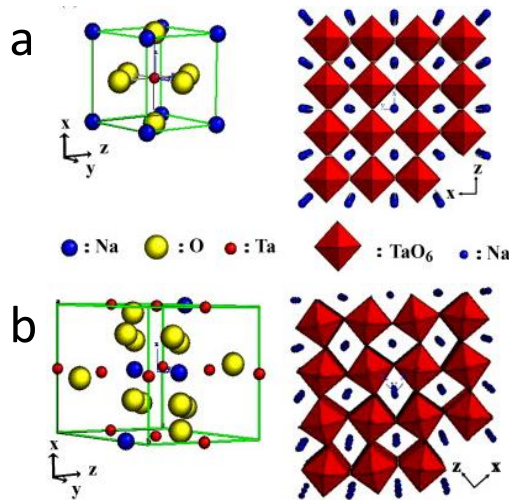
Figure 3.2 Representation of the unit-cell and the perovskite crystalline structures of $NaTaO_3$: (a) the monoclinic phase; (b) the orthorhombic phase. The coordination polyhedra on the right show the octahedra linkage in both cases and the distortion in the orthorhombic phase.[25] Copyright 2007 Elsevier

It is recognized that the performance of photocatalysts relies on features like their crystallinity, phase composition, morphology, band gap and surface properties, which can be tailored and adapted depending on the photocatalytic system involved. In this context, the use and development of chemical approaches to obtain these features are highly desired. Several methods have been reported for the preparation of tantalates. However, the solid state reaction is still the most widely employed method to obtain the majority of tantalate compounds.[13] This is because the synthesis of ternary oxides or even more complex oxides demands high-temperatures (usually above 600 °C), and such temperatures make the achievement of small particle sizes or high surface areas hardly possible. Thus, on the one hand, solid state reactions require high temperatures and long calcination periods to obtain the desired phases, but this leads to a small surface area (or large crystallite sizes due to sintering and particle growth). On the other hand, general soft-chemistry methods make use of mild temperatures plus ligands and/or stabilizers, ensuring the control over nucleation and particle growth (temperatures between 120 and 200 °C followed by annealing temperatures around 500 °C). Additionally, It is worth to mention hydrothermal[26], alkoxide based[27] and sol-gel methods[25,28] can be used to achieve nanostructured materials with relatively larger surface areas at the cost of restricted tantalate compositions. In the present work, the exo-template method employed by Wohlrab et al. was adapted to synthesize sodium tantalate ($NaTaO_3$) with nanoscale dimensions and consequently higher surface areas. This method consists of enclosing the formation and crystallization of a precursor within a D-sucrose/polyvinyl alcohol matrix (exo-template)[29] which is removed during the formation of the oxide material. In this manner, particle agglomeration was avoided resulting in nanoparticles with narrow particle size distribution. In order to compare the photocatalytic results obtained by the exo-template method, Table 3.1 summarizes the performance

in photocatalytic water splitting by the most relevant sodium tantalates prepared by different methods.

Table 3.1 NaTaO$_3$ photocatalysts used for water splitting reaction

Catalyst	Synthesis method	Lamp (filter)	Co-catalyst (loading amount)	Reaction Solution	H$_2$ evolution Activity [μmol h^{-1}g^{-1}]	Year [Ref.]
NaTaO$_3$	solid state reaction	400 W Hg	-	water	4	1998[13]
NaTaO$_3$	solid state reaction	400 W Hg	-	water	160	2001[12]
NaTaO$_3$	solid state reaction	400 W Hg	Ni / 0.16 wt.%	water	219	2001[12]
NaTaO$_3$	solid state reaction	400 W Hg	Ag / 0.2 wt. %	water	38	2001[12]
NaTaO$_3$	solid state reaction	400 W Hg	Pt / 0.1 wt. %	water	2.6	2001[12]
NaTaO$_3$	solid state reaction	400 W Hg	NiO / 0.05 wt.%	water	2180	2001[12]
NaTaO$_3$:La[a]	solid state reaction	400 W Hg	NiO / 0.2 wt.%	water	19800	2003[5]
NaTaO$_3$	solid state reaction	400 W Hg	-	water	13.5	2009[30]
NaTaO$_3$:Sr[b]	solid state reaction	400 W Hg	NiO / 0.1 wt.%	water	27200	2009[31]
NaTaO$_3$	solid state reaction	400 W Hg	Au / 3 wt.%	water	2820	2013[32]
NaTaO$_3$	solid state reaction	700 W Hg	-	water-methanol	10500	2014[33]
NaTaO$_3$	solid state reaction	150 W Hg	-	water-methanol	340	2014[33]
NaTaO$_3$	solid state reaction	150 W Hg	Au / 0.2 wt.%	water-methanol	890	2014[7] (this work)
NaTaO$_3$	solid state reaction	150 W Hg	m-rGO /10 wt.%	water-methanol	290	2014[7] (this work)
NaTaO$_3$	solid state reaction	150 W Hg	Au 0.2 wt.% and m-rGO 10 wt.%	water-methanol	380	2014[7] (this work)
NaTaO$_3$	hydrothermal	350 W Hg	-	water-methanol	36750	2007[34]
NaTaO$_3$	hydrothermal	450 W Hg	NiO / 1.0 wt.%	water-methanol	6666.7	2011[26]
NaTaO$_3$	hydrothermal	450 W Hg	NiO / 0.4 wt.%	water	1100	2012[35]
NaTaO$_3$	hydrothermal	700 W Hg	-	water-methanol	15600	2014[33]
NaTaO$_3$	hydrothermal	300 W Xe 420-800 nm	Pt / 0.5 wt.%	water-methanol	104	2015[36]

35

$NaTaO_3$	sol-gel	400 W Hg	-	water	2050	2007[25]
$NaTaO_3$	sol-gel	400 W Hg	-	water	2550	2007[30]
$NaTaO_3$	sol-gel	400 W Hg	NiO / 3 wt.%	water	9000	2010[37]
$NaTaO_3$:La[a]	sol-gel	400 W Hg	RuO_2 / 1.0 wt.%	water	4108	2010[38]
$NaTaO_3$:La[a]	sol-gel	400 W Hg	-	water-methanol	2860	2011[5]
$NaTaO_3$:La[a]	sol-gel	400 W Hg	NiO / 0.3 wt.%	water-methanol	29200	2011[28]
$NaTaO_3$	template	400 W Hg	NiO / 1 wt.%	water	3450	2011[26]
$NaTaO_3$	exo-template	150 W Hg	-	water-methanol	5960	2014[7] (this work)
$NaTaO_3$	exo-template	150 W Hg	Au / 0.2 wt.%	water-methanol	10060	2014[7] (this work)
$NaTaO_3$	exo-template	150 W Hg	m-rGO /10 wt.%	water-methanol	9500	2014[7] (this work)
$NaTaO_3$	exo-template	150 W Hg	Au 0.2 wt.% and m-rGO 10 wt.%	water-methanol	17780	2014[7] (this work)

a: doped with lanthanum; b: doped with strontium; The table is organized by synthesis method and year.

3.3 Co-catalyst loading for efficient photogenerated charge separation

The coupling of efficient co-catalysts to the light absorbing semiconductor has been extensively investigated as a pathway to enhance solar fuels production, hence co-catalyst loading onto semiconductors is the key to achieve charge carrier separation in photocatalytic water splitting systems.[3,39,40] Consequently, noble metals like Au, Pt, Rh, Pd, Ag have been extensively used together i.e. co-loaded with different kinds of photosemiconductor materials. The class of photosemiconductors includes the long list of metal oxides, (oxy)nitrides, chalcogenides such as tellurides, sulfides and selenides for instance. In summary nearly 200 crystalline phases were reported until 2010.[41] The loading of co-catalysts onto the semiconductor surface has been proven beneficial to enhance the activity and photocatalyst lifetime. The intimate contact between the metallic particle and the semiconductor is responsible for the formation of a Schottky junction (i.e. to achieve Fermi level equilibria, the electrons from the semiconductor will flow in the direction of the lower energy states in the metal). Therefore positively charged atoms remain in the semiconductor, generating a space charge interface. This interface may promote the separation of photogenerated electrons and holes.[42] Moreover, metallic particles deposited onto the surface of the semiconductor behave as an electron sink or reduction sites to facilitate the proton reduction reaction for instance, as illustrated by Fig. 1.1a. Likewise, preparation of photocatalysts loaded with different co-catalysts prepared by different methods was reported by Kanno et al. where Pt, Au and Pd enhanced the evolved amount of hydrogen gas.[43] In this context, Bamwenda et al. compared the photocatalytic

activity for hydrogen generation from water-ethanol solutions using Pt and Au as co-catalysts. The H_2 turnover rate was higher for Pt in comparison with Au reaching 8.85 and 7.81 $\mu molgmin^{-1}m^{-2}$, respectively.[44] However, Iwase et al. reported a similar study of several different photocatalysts photodeposited with noble metal nanoparticles. Additionally, it was found out that the back reaction between H_2 and O_2 to produce water is negligible just by using gold.[32,45] Later, the influence of the co-catalyst structure over photocatalytic hydrogen production was investigated. Structures like Pd_1Au_1 alloy, Au_{shell}-Pd_{core} and Pd_{shell}-Au_{core} were synthesized, loaded onto benchmark photocatalyst and tested as cocatalysts.[46] The authors identified that the alloy composition, size and morphology of the metal co-catalyst strongly influenced the photocatalyst performance. Besides, $Pd_{shell}Au_{core}$ displayed extraordinary high efficiencies for the H_2 evolution over a variety of chemical feedstocks (like glycerol, ethanol, 1,2-propanediol, fructose, etc) yielding 0.9 $mmol\,h^{-1}$ hydrogen.[46] All the aforementioned examples contributed to corroborate the approach of introducing co-catalyst to prevent the photogenerated charge recombination improving in this manner the photocatalytic efficiency.

3.4   Graphene and related layered material applied to photocatalysis

The successful isolation of a single layer honeycomb lattice made of carbon atoms into a two dimensional crystal structure in 2004, gave rise to another carbon allotrope called graphene.[47] The advent of graphene is so impressive that in a period of nearly 10 years, most of the top journals in chemistry, physics and materials science displays at least one paper featuring in the most cited papers of all times[†]. This excitement in the scientific community was caused by the unique properties this flat monolayer of carbon atoms displayed. First, it is a one-atom-thick crystal or the thinnest 2D monolayer. Nanoindentation experiments established graphene as the strongest material ever measured.[48] Furthermore, due to the superior electron conductivity, and mobility of charge carriers at room temperature (200000 $cm^2V^{-1}s^{-1}$), chemical stability and high theoretical specific surface area of nearly 2630 m^2g^{-1}, it is not surprising that many applications have been found such as solar energy conversion[49,50] fuel cells[51], batteries[52], biomaterials[53] and photocatalysis[7,54] that make use of these excellent graphene properties.

Concerning the exceptional properties of graphene, one important distinction must be addressed regarding the properties that are obtained by physical methods and the properties obtained by chemical methods. In general, the physical approaches such as micromechanical exfoliation[55], chemical vapor deposition[56] and epitaxial growth onto metallic surfaces[57] are able to produce high quality samples (usually few flakes within the range of 1 cm^2 with one or two layers[47])

[†] Journals like: Science, Nature, Nature Materials, PNAS, Physical Review Letters, Chem. Soc. Rev., ACS Nano, Angew. Chem. Int. Ed., Nano Letters, Chemistry of Materials and Carbon for instance. Citation number of each journal was performed using ISI Web of Knowledge database and sorted by the highest citation option, as of April 2015.

that can be used to measure fundamental physical properties at the expense of obtaining very small amounts, very high cost and complex equipment. However, the chemical properties of graphene depend very much upon its preparation method. Hence, chemical methods such as colloidal dispersions[58,59] and oxidation-exfoliation followed by reduction have been used.[60,61] By using chemical approaches employing graphite as starting material it is possible to achieve scalability and affordability to the detriment of lower quality. As a result of the harsh oxidation and exfoliation conditions the so called graphene products provided by chemical methods possess drawbacks such as large variations in thickness, surface defects, lateral areas, and shape of the exfoliated graphene flakes.[62] This polydispersity represents issues in many applications since many of the properties of graphene are intrinsically linked to its monolayer structure. Shortly, many applications described above cannot make use of those exceptional properties that are present in high quality samples produced by physical methods, due to the limited amount. Therefore, the great majority of these applications rely on chemical produced "graphene" that provides at least a few grams of sample with poorer physical properties.

An overview of the literature dedicated to graphene combined with semiconductors applied to photocatalytic approaches revealed that an activity improvement arises from the superior electron mobility properties of graphene, which is conducive to the separation of the photogenerated charge carriers from the photocatalyst.[1,54,63,64] Several authors proposed the following mechanism for the electron-hole pairs separation: The photoexcited electrons are transferred from the conduction band of the semiconductor (e.g. CdS) not only to the co-catalyst (e.g. Pt), but also to the carbon atoms on the graphene layers. The electron transfer to the graphene sheet enables additional accessible sites to readily reduce protons into H_2.[1] Additionally, high quality reviews can be found elsewhere demonstrating the high electron mobility property of graphene and the electron transfer mechanism.[54,63,64] Tracking the first publications using the combination of photocatalyst with graphene is comparable to find a needle in a haystack, because of the huge amount of publication in this field and besides the inconvenience of inaccurate and unsystematic nomenclature used to designate graphene. As an inaccurate nomenclature example one can mention the following: "Materials are referred to as "graphene", even when they contain hundreds of layers or are particles that lack the basic sheet-like structure of a 2D material. However, a very clear and concise nomenclature was proposed by journal CARBON.[65] Therefore, the first representative papers in this field may be attributed to Kamat, Loh and Akhavan et al.[66-68] Kamat et al. followed by Loh et al. performed a UV-assisted reduction of graphene oxide in colloidal TiO_2, by a stepwise electron transfer from the TiO_2 conduction band to graphene oxide. Resulting in the reduction of the main oxygen functional groups present in graphene oxide and consequently improving the conductivity of the obtained reduced graphene composite material. Akhavan and Ghaderi used graphene oxide-TiO_2

thin films to promote the same effect as obtained by Kamat and Loh groups, however at this time by the use of solar irradiation. Further, the obtained nanocomposite films were used as photocatalysts for photodegradation of E. coli bacteria in an aqueous solution. Thus far, since 2010 graphene based composites have been used for several photocatalytic reactions which include: degradation of organic dyes/pollutants, selective organic transformations, photovoltaic devices, reduction of CO_2 and for water splitting.[66-68] One interesting report regarding improving water splitting involving tantalates and reduced graphene oxide was reported by Mukherji et al..[69] In this approach, a doped nitrogen-tantalate ($Sr_2Ta_2O_{7-x}N_x$) was synthesized by solid-state reaction. Similarly to the method of Kamat and Loh, the nitrogen doped-photocatalyst ($Sr_2Ta_2O_{7-x}N_x$) was employed to reduce graphene oxide. Later on, the obtained conductive carbon material (reduced graphene oxide) was reported to shuttle electrons to a platinum co-catalyst deposited onto the reduced graphene oxide surface upon sun light irradiation. The strategy of using graphene to promote electron transfer the authors expected to reduce significantly the recombination of electrons with holes, by facilitating the electron transfer to the surface of the photocatalyst for hydrogen production. In this way, they achieved hydrogen evolution rates of nearly 300 µmolh^{-1} under simulated sunlight.

In spite of the recent advances in the field of chemically produced graphene and its use in combination with photocatalysts, there is still much room for improvement in the synthesis of graphene in regard to influencing its electronic properties in the photocatalysis field.

3.5   Main results and Discussion

Sodium tantalate was synthesized by two different methodologies: (i) exotemplate method (EM) and (ii) solid state reaction (SSR). The X-ray powder diffraction (XRD) patterns of $NaTaO_3$ prepared by EM and SSR showed that it existed as pure orthorhombic[70] single crystalline phase, as represented in Fig. 3.2b. The obtained structures were in correspondence with the powder diffraction file (PDF) 73-878 or ICSD 23319, as shown in Fig. 3.3. Features like particle size and specific surface area of the powders were calculated using Scherrer's equation[‡] from the XRD patterns and the Brunauer, Emmett and Teller isotherms (BET method) using nitrogen sorption experiments, respectively. The powder obtained by the EM method resulted in average crystallite sizes of nearly 25 nm and a surface area of around 22 m^2g^{-1}, whereas the powder material obtained from SSR exhibited surface area of approx. 1.5 m^2g^{-1}, and as a result of the sharp reflections and limitations of the Scherrer equation its crystallite size could not be calculated.

So far, the microstructure and surface observed for the mentioned compounds are in agreement as expected from these experimental methodologies, i.e. SSR vs soft chemistry route.

[‡] $\beta(2\theta) = K \lambda / L \cos \theta$, where: B = peak width; K = the Scherrer constant (shape factor); λ = X-ray wavelength; θ = the Bragg angle and L = mean crystallite size.
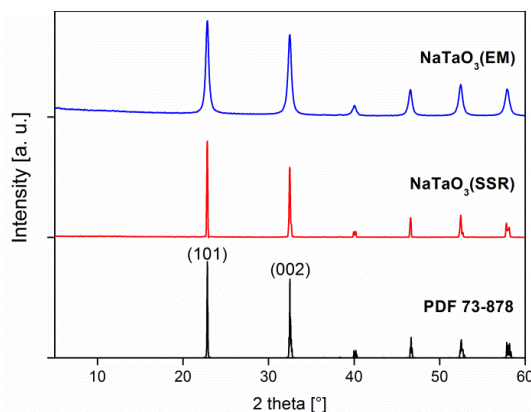
Figure 3.3 Powder XRD patterns of NaTaO$_3$ prepared by SSR and EM compared to the orthorhombic powder diffraction pattern (PDF 73-878).

As SSR relies on high temperature synthesis (> 1000 °C), the reaction is governed by diffusion and mass transport, resulting in a thermodynamically highly stable compound, high crystallinity and large grain/particle sizes due to sintering effects. The soft chemistry route (EM) generates smaller particle sizes with relative high crystallinity. Due to the presence of the organic matrix particle growth is limited as illustrated by Fig. 3.4e. However, template removal should proceed fast in order to prevent subsequent sintering. To monitor this, particle size and morphology of the tantalates produced by SSR and EM can be visualized by scanning electron microscopy (SEM) as depicted in Fig. 3.4. As expected NaTaO$_3$ (SSR) consist of crystallites with sizes in the micrometer range, as several aggregates and to the irregular morphology (as in Figs. 3.4a and 3.4b), whereas NaTaO$_3$ (EM) is mainly composed of particles in the nanometer range (Figs. 3.5c and 3.5d).
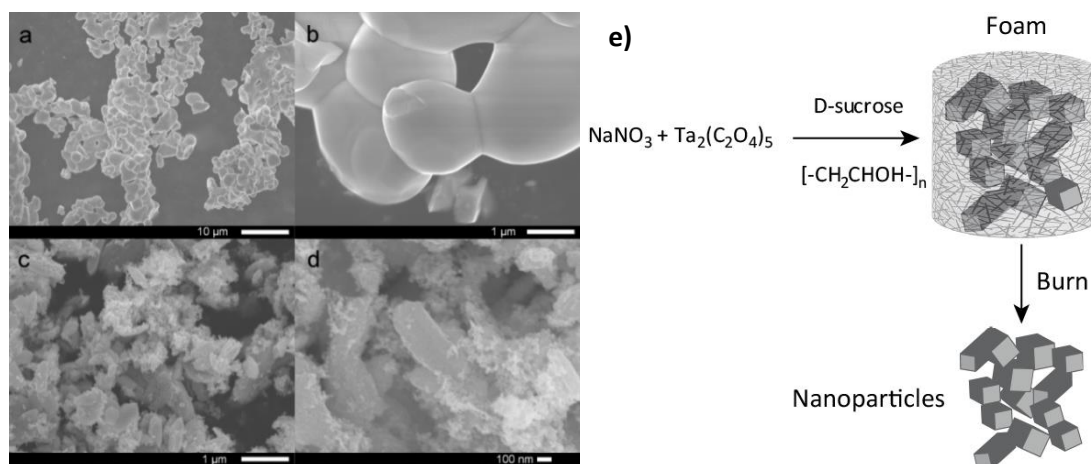
Figure 3.4 SEM images of NaTaO$_3$ materials prepared by SSR showing the overview of the obtained particles (a) higher magnification is able to show the sintering effect provoked by high annealing temperature (b) particles obtained by EM method showing smaller particle sizes provided by the low temperature soft-chemistry (c), higher magnification showing the agglomerates of small crystallites d). Illustration of the exo-template method used to prepare the nanoscale tantalate (e).

40

Further transmission electron microscopy of the latter revealed that the nanoparticle sizes are in the range of 20 to 25 nm (Figure 3.5), which agrees well with the values estimated by the Scherrer equation. The insets in Figure 3.5 show the selected area electron diffraction (SAED) patterns which corresponds to the orthorhombic phase in analogy with the XRD measurement.
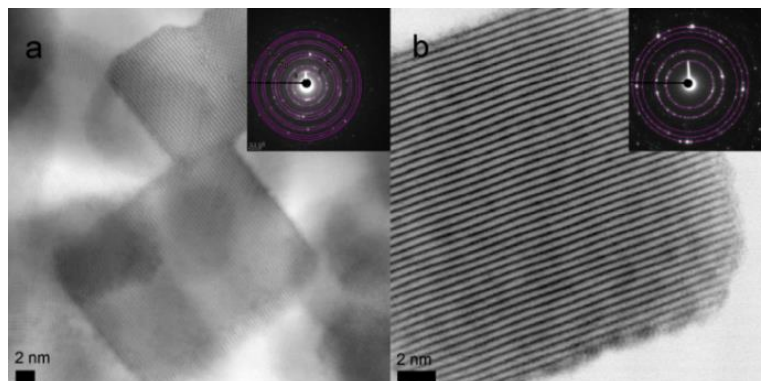
Figure 3.5 HRTEM images of NaTaO$_3$ (EM) nanoparticles (a, b) with insets of SAED patterns.

Au-MNP were photochemically deposited (0.2 wt. %)[§] onto the NaTaO$_3$ synthesized by (SSR). TEM images of this arrangement are shown in Figure 3.6a and 3.6b. The same procedure was performed with the tantalate produced by the EM method; see Figs. 3.6c and 3.6d for TEM pictures. The sizes of the gold particles in both cases are in the range of 2-10 nm and the shapes are nearly spherical. However, one should take into account the higher spatial distribution of Au-MNP on the NaTaO$_3$ (EM) in comparison with those on NaTaO$_3$ (SSR), which leads to a slightly different Au-MNP size distribution in the SSR material compared with the EM material. The arrangement of the photo-semiconductor decorated with Au-MNP resembles that shown in Fig. 2.3b, where one can observe individual and isolated Au particles deposited onto the NaTaO$_3$ surface (in both employed methods) acting as reduction catalyst site.

m-rGO was prepared by oxidation and exfoliation of pristine graphite (by a modified Hummer's method)[71] , followed by a reduction step in order to achieve the conductive multilayer carbon material, as published elsewhere.[72,73] Therefore, taking into account that pristine graphite is the starting material, the resulting oxidation/exfoliation and reduction steps should result in structural changes such as: (i) the distances between the layers (interlayer spacing), (ii) disrupted carbon sp^2 bonding network into sp^3 hybridization due to the high oxidizing acidic media and (iii) a partially restored π-network by the reduction of graphene oxide (m-GO). The XRD patterns of the graphite, m-GO and the m-rGO are shown in Fig. 3.7a.

[§] Other photochemical deposited gold loadings were also tested (0.5, 1 and 2 wt. %), at the conditions tested 0.2 wt. % showed the best relation loading/activity.

The main plane (002) of the graphite powder was 2θ = 26.5° (*d*-spacing of 3.4 Å). A typical broad peak shift to 2θ = 11.3° was observed after the oxidation and exfoliation process. The generated m-GO possess an interlayer spacing of around 7.9 Å that is attributed to the inclusion of carbon sp^3 carbon and oxygen containing functional groups (like: carbonyl, epoxy, alkoxy and hydroxyl groups) besides incorporated water molecules.[74-76]
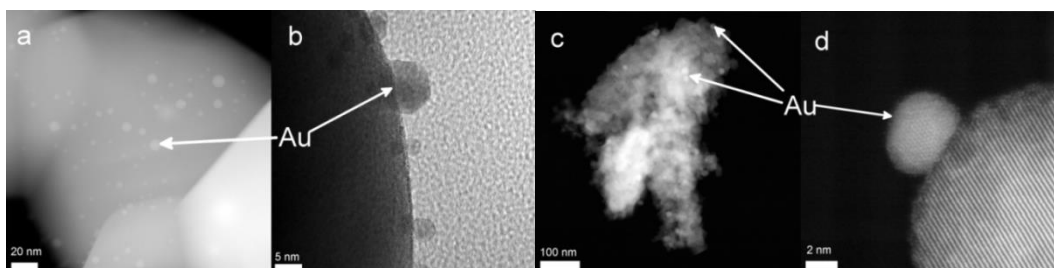
Figure 3.6 TEM image of photo deposited 0.2 wt.% Au-NP on NaTaO$_3$ prepared by SSR (a, b) and EM (c, d).

After the chemical reduction step the (002) reflection, characteristic for the π-π stack layers, was weakened by one order of magnitude, however the (002) reflection is still centered at 2θ = 11.3°. This indicates that the planar π-network was just partially re-established.

The ATR-FTIR in Fig. 3.7b clearly displays the oxygen functional groups incorporated into m-GO and the partial reduction generated at m-rGO. The vibration bands belonging to the hydroxyl (3415 cm^{-1}), alkoxy (1055 cm^{-1}) and epoxy (1229 cm^{-1}) groups completely disappeared after the solvothermal reduction. The presence of carboxyl group vibrations in the m-rGO spectrum is still visible, indicating the partially reduction of m-rGO and the persistence of oxygen functional groups. Additionally, the main C=C bond of the graphene stack layers is preserved, which is confirmed by the presence of the vibration band of the conjugated double bond (1625 cm^{-1}), which is shifted in the spectrum of m-rGO to 1561 cm^{-1} in conformity with what was reported in the literature.[77] X-ray photoelectron spectroscopy (XPS) measurements (Fig. 3.7c, 3.7d) provided direct evidence for the partial reduction of m-GO corroborating the main results observed by FTIR. XPS of m-rGO still shows a significant degree of oxidation. For instance, the C1s curve fitting results in the assignment of the 4 following groups: (i) non-oxygenated C ring (C-C) at 284.5 eV, (ii) the carbon in C-O bonds (C-O) at 285.6 eV, (iii) carbonyl carbon (C=O) in the range of 287 eV and the carboxylate carbon (C-O=O) at around 289 eV. Additionally, the observed peak at 292.5 eV can be identified as a shake-up transition characterized by a π-π* satellite peak.[**] The O1s spectrum is split into two functional groups such as the C-O and C=O bonds respectively at 531,7 and 533,2 eV.[78,79] XPS analysis has also been used to

---

[**] The origin of shake-up peak arises due to the removal of a core electron through photoionization process, in which an electron from a bonding orbital can be transferred to an antibonding orbital. In detail: a part of the outgoing electron interacts with valence electrons and excites them (shakes it up) to a higher energy level. As a consequence the kinetic energy of these core electrons is reduced and a satellite structure appears a few (eV) below the core level position.

determine atomic composition for carbon to oxygen (C/O) ratios of m-GO and m-rGO and the results are summarized in Table 3.2. Reduction of m-GO to m-rGO can be indicated by an increase in the C/O ratio. The oxygen content of the m-rGO is still disappointingly high after the reduction step. Since only surface species are measured with XPS it can be derived that the reduction of the m-GO to m-rGO occurs mainly on the surface of the carbon sheets. Therefore, the apparent disparity results from Table 3.2 are consistent with the obtained multilayer carbon material, because the inner layers were not as well reduced as the top and bottom layers. The elemental analysis provides an average of the bulk sample whereas XPS provides an average of the functional groups present on the surface.

Table 3.2 Atomic composition of multilayer graphene oxide (m-GO) and multilayer reduced graphene oxide (m-rGO) measured by X-ray Photoelectron Spectroscopy (XPS) and Elemental Analysis (EA)

sample	Elemental Analysis %			XPS %		
	C	O	C/O	C	O	C/O
m-GO	54.77	43.3	1.26	64.53	35.47	1.82
m-rGO	68.4	30.1	2.27	85.16	14.84	5.74
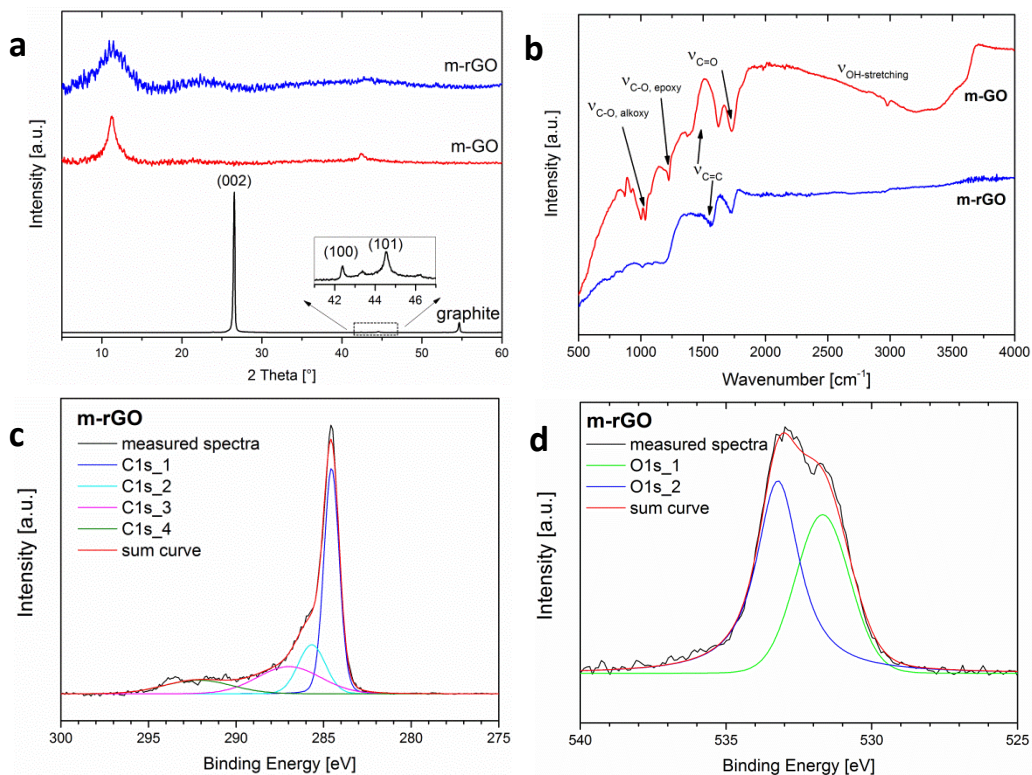
Figure 3.7 (a) Powder XRD pattern of pristine graphite, multilayer graphene oxide (m-GO) and multilayer reduced graphene oxide (m-rGO); (b) ATR-FTIR spectra of m-GO and m-rGO; (c) XPS of m-rGO C1s peak and (d) O1s peak.

TEM investigations conducted on m-rGO samples revealed that the stacks are in the size range of 50-200 nm as depicted by Figure 3.8a and the thickness of the obtained stack can be seen in Fig.

3.8(b). This information also confirms that the oxidation/exfoliation procedure followed by the reduction was not sufficient to produce single isolated sheets. Instead, a multilayer structure was the result of the method employed in this work. The HRTEM in Fig. 3.8(b) displayed clearly the d-spacing between the graphitic stack which could be measured by using image processing software (ImageJ 1.47v). The number of layers observed in the analysed zoomed region in the inset in Fig. 3.8c is exhibited in the plot profile on the right side. In this region there are 16 layers.

Both $NaTaO_3$ (EM) as well as $NaTaO_3$ (SSR) were tested for photocatalytic hydrogen generation. The photocatalytic activity of pure $NaTaO_3$ (EM) was at least 17-fold higher than that of pure $NaTaO_3$ (SSR) (black columns in Fig. 3.9). Next, the effect of adding m-rGO to $NaTaO_3$ (EM) and $NaTaO_3$ (SSR) was evaluated. Breakthrough values of photocatalytic activity such as 32 times higher activity for the $NaTaO_3$ (EM) with 10 wt. % of m-rGO (related to the photo-semiconductor mass) were obtained (green columns in Fig. 3.9). This result demonstrates the electron collecting and transporting properties of m-rGO as well as its intrinsic catalytic activity as demonstrated by the EPR measurements (Fig. 3.10). $NaTaO_3$ (SSR) exhibited no significant changes with respect to the kind of co-catalyst and/or additive added, while $NaTaO_3$ (EM) displayed significant enhancement of its photocatalytic activity by combining the catalyst with photo-deposited Au-MNP and/or m-rGO.
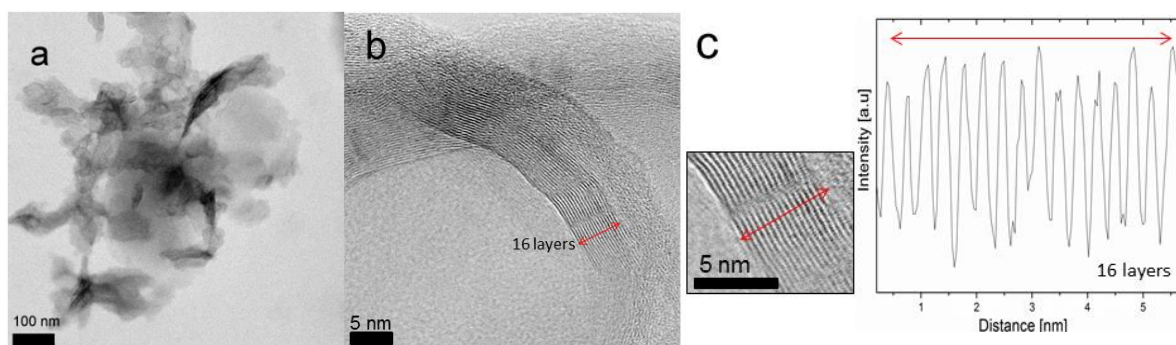
Figure 3.8 TEM images of multilayer reduced graphene oxide (m-rGO). (a) Overview of the dried m-rGO; (b) HRTEM profile of the m-rGO displaying the multilayer characteristic of the obtained material, (c) Inset: zoomed region of figure (b) showing the interlayer spacing between the m-rGO and experimental plot profile of the red arrow of a typical HRTEM image displaying the amount peaks. Each peak represents one single layer of reduced graphene oxide. The plot profile of the analysed region possesses 16 layers.

The poor activity of this ensemble can be attributed to the large particle size (> 1 μm) and consequently the very low specific surface area (1.4 m^2g^{-1}) of $NaTaO_3$ (SSR) as well as the size incompatibility between the catalyst (in the micro-size range) and the nano-meter size range of Au-MNP and m-rGO. The large heterostructure suffers from bulk recombination, whilst small particle sizes may allow short pathways between photocarrier generation junction and redox reaction centers, reducing in this way the length of charge diffusion and therefore improving the photocatalytic efficiency.[22] It should be noted that the photocatalytic activity in the current case

correlates well with the specific surface area of the semiconductors measured by BET. The EM/SSR NaTaO$_3$ BET surface area ratio is 16, which correlates well with the ratio of photocatalytic hydrogen production of 17.5. Moreover, the incorporation of Au-MNP together with m-rGO into a NaTaO$_3$ (EM) solution mixture led to a hydrogen evolution rate of 17.78 mmolh^{-1}g^{-1} which is 52 times higher than the NaTaO$_3$ (SSR) reference. The reason for this might be that all components are in the same nano-size range and therefore have good interparticulate contact. Additionally, the configuration of the Au-MNP together with the m-rGO onto the photo-semiconductor (NaTaO$_3$) facilitates the photogenerated electron transfer from conduction band to the additives with electron affinity such as the deposited Au-MNP and m-rGO conductive material. From the results shown in Fig. 3.9 is is clear that the m-rGO when combined with sodium tantalate also acts as a co-catalyst; in fact, it is as effective as Au-MNP.

Thus, the enhanced hydrogen generation can be attributed to an efficient electron transfer and the synergistic effect due to the presence of Au-MNP and m-rGO in solution mixture.

In view of the H$_2$ evolution results that were obtained by co-loading the photocatalyst with Au-MNP and/or m-rGO and the lack of spectroscopic proof concerning the active species (electron-hole pairs) involved in this heterogeneous photocatalytic system, it was decided to perform *in situ* EPR investigations to shed light onto the enhancement of photocatalytic performance. For these investigations, EPR spectra of pure NaTaO$_3$ (EM) and (SSR) were collected under optional UV-vis light under air, helium and saturated with water/methanol under Helium.
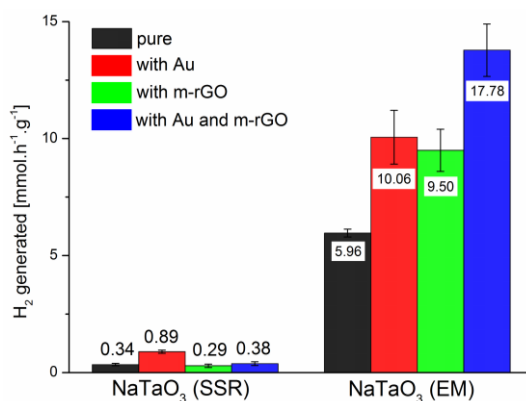
Figure 3.9 Comparison of the photocatalytic activity of NaTaO$_3$ synthesized by solid state reaction (SSR) and exotemplate method (EM) for H$_2$ generation and the influence of different incorporated additives. Experimental conditions: 200 mg of catalyst, 7 vol% methanol aqueous solution as sacrificial reagent, 0.2 wt% Au as cocatalyst and 10 wt% of m-rGO as additive. 150 W mercury lamp irradiation source. The H$_2$ amount was determined by offline gas chromatography using a molecular sieve 5 Å column, TCD and argon as carrier gas.

The irradiated samples under air (i) at room temperature generated distinguished signals for NaTaO$_3$ (EM) at **A** and **B**, Fig. 3.10a. However, no light induced species could be detected for the NaTaO$_3$ (SSR). Since the EPR signals are not broadened due to ambient oxygen and signal **A** is not affected by intensity, the center **A** was assigned to electrons trapped in oxygen vacancies as

observed in other metal oxides reported by Sun et al.,[80] whereas the **B** center was assigned to trapped holes ($O^{\bullet-}$ species) located in $NaTaO_3$ subsurface depth. The replacement of air by helium resulted in the curve registered at (ii) Figure 3.10a where both tantalates (EM) and (SSR) exhibited the same signal although the SSR sample showed less intensity, as result of the high surface area of $NaTaO_3$ (EM). It was observed three additional centers labelled as **C**, **D** and **E**, which are more prone to be located at the outermost $NaTaO_3$ surface. Their nature were probed under illumination with small addition of H_2O_2 to the $NaTaO_3$ (EM), which produced superoxide species, $O_2^{\bullet-}$, with signal similar to **C**. This indicated that signal **C** can be attributed to surface-bound $O_2^{\bullet-}$, which can occur by the trapping of electrons promoted by light. However the nature of signals **D** and **E** were not identified for a good match between the experimental and simulated spectrum, these signals most probably arise from adsorbed paramagnetic oxygen radicals.
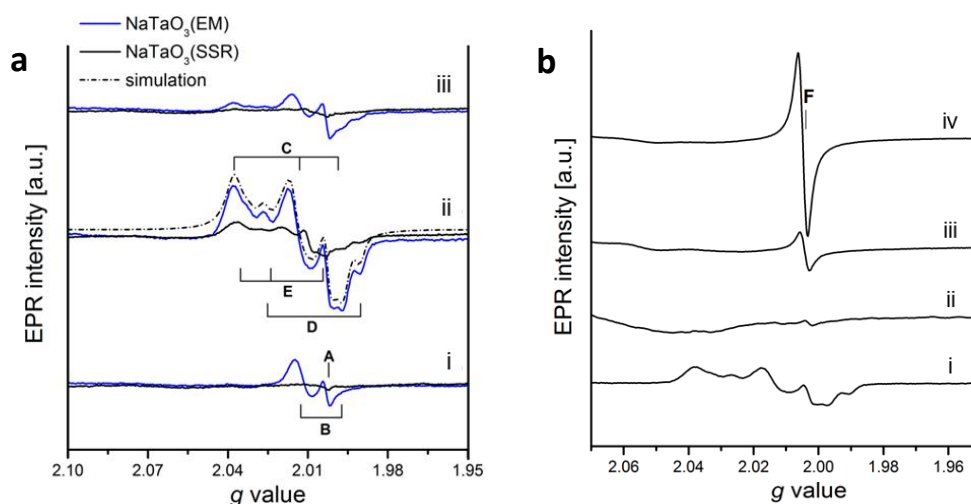
Figure 3.10 (a) *in situ* EPR spectra comparison of the experimental (solid lines) and simulated (dashed line) during irradiation with UV-vis light of $NaTaO_3$ (EM) (blue) and $NaTaO_3$ (SSR) (black) (i) ambient air (ii) under helium flow and (iii) under H_2O/methanol saturated helium flow. **A** center signal: assignment to **F** centers; **B** center: assignment to subsurface oxygen radical $O^{\bullet-}$; **C** center: surface superoxide radical $O_2^{\bullet-}$; **D** and **E** centers: surface oxygen species. (b) in situ EPR spectra in helium flow during irradiation with UV-vis light of $NaTaO_3$ (EM) (i) pure, (ii) loaded with 0.2 wt. % Au, (iii) loaded with 10 wt. % m-rGO, (iv) loaded with 0.2 wt. % Au and 10 wt. % m-rGO. **F** center signal: assignment to carbon based localized conduction electrons, EPR parameters: $g_1=2.003$, $g_2=2.003$, $g_3=2.003$.

Addition of H_2O/methanol to saturate the helium flow, resulted in significant decrease of intensity attributed to signals to surface-bound oxygen species (signals **C**, **D**, and **E**) as well as to subsurface $O^{\bullet-}$ radicals (signal **B**). Signals **C**, **D**, and **E** also lost intensity upon the solely addition of water without the presence of hole scavenger. This is evidence that the corresponding surface oxygen radicals are either consumed by water molecules or their formation is prevented by addition of H_2O. Whereas the addition of methanol slightly decreased the signal **B** attributed to trapped holes at oxide anions ($O^{\bullet-}$), without changing the others signals **C**, **D** and **E**. The *in situ* EPR spectra depicted in Figure 3.10b confirmed the role of m-rGO acting as a conductive layer contributing to supress the charge carriers

recombination in physical mixture of the solids. The curve (iv) at Figure 3.10b which contains $NaTaO_3$ (EM) loaded with Au and m-rGO exhibited a strong signal called **F** center while in the other curves (i-iii) such high intensity signal was not observed. The signal F was assigned to carbon-based localized conduction electrons in the m-rGO. Thus, the loading of Au-MNP and m-rGO onto $NaTaO_3$ (EM) enables the electron transfer from the conduction band of the photocatalyst to the co-catalysts like Au-MNP and m-rGO as illustrated by the scheme in Fig. 3.1. This electron transfer is considered one of the reasons for the enhacement of photocatalytic activity of oxide semiconductors in solution mixtures. Additionally, the $NaTaO_3$ (EM) loaded with Au and m-rGO (Fig. 3.10b, curve iv) exhibited a more intense signal **F** in comparison with $NaTaO_3$ (EM) loaded only with m-rGO (Fig. 3.10b, curve iii). It can be concluded that the Au co-catalyst supports the electron transfer from the semiconductor to the carbon atoms on the graphene sheet. Surface plasmon resonance phenomena usually attributed to metal nanoparticles such as gold were not observed so far in the measured UV-vis spectra as shown in Fig. 3.11. However the plasmonic effect can play an important role concerning the conducting electron transfer from Au nanoparticles to the graphene sheet and/or semiconductor and this effect cannot be excluded. Significant novel insights into this effect were reported by Priebe et al., who described a visible light driven electron injection from the Au conduction band to the TiO_2 semiconductor conduction band, which contributed to activate the TiO_2 photocatalyst into the visible light.[82]
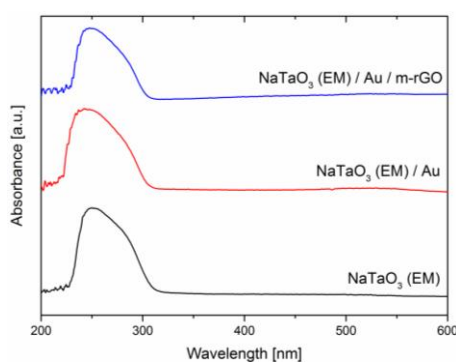
Figure 3.11 UV-vis data of pure $NaTaO_3$, $NaTaO_3$ loaded with Au and $NaTaO_3$ loaded with Au and m-rGO produced by the exotemplate method (EM).

3.6   Conclusions

Strategies such as implementing soft chemical routes like the exo-template method (EM) resulted in the formation of crystals with smaller particle sizes, which is an important parameter to enhance photocatalytic activity. $NaTaO_3$ nanoparticles also proved to be more active as photocatalyst than the ones synthesized by solid-state reaction (SSR). Furthermore, the hydrogen generation was increased significantly by adding Au-MNP and/or m-rGO as co-catalysts onto the $NaTaO_3$ (EM) photo-semiconductor, whilst for $NaTaO_3$ (SSR) no significant changes were observed with respect to

photocatalytic activity. In this context, optimization of the proper spatial configuration and the relative size between the components (Au-MNP, m-rGO together with $NaTaO_3$ nanocrystals) resulted in a further improvement of hydrogen generation. Hydrogen generation was 52-fold higher (17.78 $mmolh^{-1}g^{-1}$) than using pure $NaTaO_3$ (SSR) as reference. One of the main drawbacks of photocatalytic systems that use heterogeneous photocatalysts lies in the fast electron-hole pair recombination. It was shown that optimized spatial configuration of gold NP reduction centers aided by the addition of a conductive reduced multilayer graphene oxide provided an effective way of suppressing the recombination of charge carriers.

3.7 Experimental Section

3.7.1 Synthesis and materials

$NaTaO_3$ (EM) was prepared via an adapted exotemplate method as described elsewhere.[81] To a solution of 0.75 g $NaNO_3$ (8.80 mmol, p.a., Merck, Germany) in 50 ml deionized water 11.4 ml of a $Ta_2(C_2O_4)_5$ (tantalum oxalate) solution (8.80 mmol, c_{Ta} = 0.77 $mmol \cdot ml^{-1}$ H.C. Starck, Germany), 3.0 g of polyvinyl alcohol (98%, M_n = 72000 $gmol^{-1}$, Roth, Germany) and 30.0 g of D-sucrose (99.7%, Roth, Germany) were added under stirring at 368 K. After complete dissolution the honey-like highly viscous mixture was heated at 493 K for 1 h to form carbonaceous precursor foam, from which the nanoparticles were produced by calcination at 773 K for 20 h.

$NaTaO_3$ (SSR) was prepared using a solid state reaction route described by Kato and Kudo.[12] Briefly, a stoichiometric mixture of 1.06 g Na_2CO_3 (9.96 mmol, p.a., Merck, Germany) and 4.40 g Ta_2O_5 (9.96 mmol, 99.99%, ChemPur, Germany) was well ground in an agate ball mill with 200 rpm for 24 h. For better distribution 20 ml of ethanol were added before milling and removed afterwards in a vacuum oven at 323 K. Finally, the mixture was thermally treated in a Pt-crucible at 1420 K for 10 h with a heating rate of 10 $Kmin^{-1}$.

Graphite powder (Sigma-Aldrich, particle size <20 μm) was used as precursor to synthesize multilayer graphene oxides m-GO and m-rGO. The synthesis protocol was modified from the procedure described by Marcano et al..[72] In detail, 3.0 g of graphite and 18.0 g of $KMnO_4$ were slowly added to a solution of 360 ml 98% H_2SO_4 and 40 ml 85% H_3PO_4 while the temperature was kept at 313 K. The mixture was set on a hot plate with a temperature of 323 K and kept there for about 12 h. After the mixture was cooled down to room temperature it was added to 400 ml ice containing 3.0 ml of 30% H_2O_2. At first the mixture was sifted two times through a metal sieve (250 μm) and the filtrate was centrifuged 15 minutes at 8000 rpm. The precipitated solid was washed two times consecutively with deionized water, 30% HCl solution and ethanol; and centrifuged (15 min. at 8000 rpm) after each washing step. Finally, the remaining material was washed with water, centrifuged and vacuum-dried overnight at 60°C to collect m-GO. For the reduction step the solid product was

dispersed in ethanol and finally kept in a Teflon-lined stainless steel autoclave at 423 K for 12 h to obtain the final m-rGO or thermal expansion approach was used to obtain m-rGO as published elsewhere.[73] The obtained oxidized material from Hummer's method was placed inside a quartz tube under argon/hydrogen (85:15 vol. % at fixed flow 100 ml/min) for at least one hour to remove the excess of adsorbed oxygen. Then, a tube oven was heated until it reached 1050 °C; after this the tube is inserted into the hot oven during 30 seconds until a short burst (thermal expansion) is observed and the black aired powder is collected with a paper filter on a filter flask connected to a vacuum pump.

3.7.2   Characterization

Powder X-ray diffraction (XRD) was carried out on a Stoe STADI P instrument in transmission geometry with Cu Kα1 radiation. The BET surface area determination was carried out on a Quantachrome Nova 4200 instrument with nitrogen sorption for high surface areas or on a Micromeritrics ASAP 2020 instrument with krypton sorption for small surface areas. SEM images were collected using a JEOL 7401F instrument and ATR-FT-IR was done on a Nicolet 6700.

The XPS investigations were obtained with an Escalab220iXL (ThermoFisher) with Al K_{α} radiation (E = 1486.6 eV). For charge compensation a flood gun was used. The spectra were referenced to the C1s peak at 284.8 eV. The samples were fixed on a stainless steel sample holder with a double adhesive carbon tape. For the determination of the electron binding energy and of the peak area the spectra were fitted with Gaussian-Lorentzian curves after subtraction of a Shirley background. For quantitative analysis of the surface composition the peak area were divided by the element specific Scofield factors and the transmission function of the spectrometer.

Transmission electron microscopy (TEM) measurements were performed at 200 kV on a JEM-ARM200F instrument (JEOL, Japan), aberration-corrected by a CESCOR (CEOS) for STEM applications. The samples were prepared by adding the solid ground samples directly on a holey carbon-supported grid (mesh 300) and transferred to the instrument.

3.7.3   Photocatalytic activity measurement

The photocatalytic H_2 production experiments were performed at least twice for each sample in an inner irradiation reactor with a 150 W medium pressure mercury lamp (TQ 150, UV-Consulting Peschl). The lamp was mounted in a quartz glass cooling jacket and kept at a constant temperature at 298 K. Prior to photocatalytic activity measurements 0.2 g of semiconductor were suspended in 100 ml of a 1:1 H_2O:MeOH solution and in some experiments 10 wt.-% of m-rGO (related to the semiconductor mass) were added and stirred overnight. Prior to irradiation, 650 ml of water were added and the suspension was stirred and purged with argon for 30 min and in some cases 0.2 wt.-%

Au (related to the mass of the semiconductor) were photodeposited onto the solid from dissolved $H[AuCl_4] \cdot 4H_2O$. The resulting solution mixtures are simply dispersed in a H_2O:MeOH solution. During the photocatalytic activity measurement the evolved gases were measured until a minimum of 20 mL was collected with gas burettes under ambient pressure and temperature. At the end of each measurement the H_2 amount was determined by offline gas chromatography using a molecular sieve 5 Å column, TCD and argon as carrier gas.

3.8 References

1.   (a) Li, Q.; Guo, B.; Yu, J.; Ran, J.; Zhang, B.; Yan, H.; Gong, J. R., Highly Efficient Visible-Light-Driven Photocatalytic Hydrogen Production of CdS-Cluster-Decorated Graphene Nanosheets. *J. Am. Chem. Soc.* **2011,** *133* (28), 10878-10884; (b) Zeng, P.; Zhang, Q.; Peng, T.; Zhang, X., One-pot synthesis of reduced graphene oxide-cadmium sulfide nanocomposite and its photocatalytic hydrogen production. *Phys. Chem. Chem. Phys.* **2011,** *13* (48), 21496-21502.

2.   Kim, H. I.; Moon, G. H.; Monllor-Satoca, D.; Park, Y.; Choi, W., Solar Photoconversion Using Graphene/TiO_2 Composites: Nanographene Shell on TiO_2 Core versus TiO_2 Nanoparticles on Graphene Sheet. *J. Phys. Chem. C* **2012,** *116* (1), 1535-1543.

3.   Xiang, Q.; Yu, J.; Jaroniec, M., Synergetic Effect of MoS_2 and Graphene as Cocatalysts for Enhanced Photocatalytic H_2 Production Activity of TiO_2 Nanoparticles. *J. Am. Chem. Soc.* **2012,** *134* (15), 6575-6578.

4.   Kato, H.; Kudo, A., Highly efficient decomposition of pure water into H_2 and O_2 over $NaTaO_3$ photocatalysts. *Catalysis Letters* **1999,** *58* (2-3), 153-155.

5.   Kato, H.; Asakura, K.; Kudo, A., Highly efficient water splitting into H_2 and O_2 over lanthanum-doped $NaTaO_3$ photocatalysts with high crystallinity and surface nanostructure. *J. Am. Chem. Soc.* **2003,** *125* (10), 3082-3089.

6.   Lin, W.-H.; Cheng, C.; Hu, C.-C.; Teng, H., $NaTaO_3$ photocatalysts of different crystalline structures for water splitting into H_2 and O_2. *Applied Physics Letters* **2006,** *89* (21).

7.   Meyer, T.; Priebe, J. B.; da Silva, R. O.; Peppel, T.; Junge, H.; Beller, M.; Brueckner, A.; Wohlrab, S., Advanced Charge Utilization from $NaTaO_3$ Photocatalysts by Multilayer Reduced Graphene Oxide. *Chem. Mat.* **2014,** *26* (16), 4705-4711.

8.   Raveau, B.; Maignan, A.; Martin, C.; Hervieu, M., Colossal Magnetoresistance Manganite Perovskites: Relations between Crystal Chemistry and Properties. *Chem. Mat.* **1998,** *10* (10), 2641-2652.

9.   Cohen, R. E., Origin of Ferroelectricity in perovskite Oxides *Nature* **1992,** *358* (6382), 136-138.

10.   Maeno, Y.; Hashimoto, H.; Yoshida, K.; Nishizaki, S.; Fujita, T.; Bednorz, J. G.; Lichtenberg, F., Superconductivity in a Layered Perovskite without Copper. *Nature* **1994,** *372* (6506), 532-534.

11.   Zhu, J.; Li, H.; Zhong, L.; Xiao, P.; Xu, X.; Yang, X.; Zhao, Z.; Li, J., Perovskite Oxides: Preparation, Characterizations, and Applications in Heterogeneous Catalysis. *Acs Catalysis* **2014,** *4* (9), 2917-2940.

12.   Kato, H.; Kudo, A., Water splitting into H_2 and O_2 on alkali tantalate photocatalysts $ATaO_3$ (A = Li, Na, and K). *Journal of Physical Chemistry B* **2001,** *105* (19), 4285-4292.

13.   Kato, H.; Kudo, A., New tantalate photocatalysts for water decomposition into H_2 and O_2. *Chemical Physics Letters* **1998,** *295* (5-6), 487-492.

14.   Yoshioka, K.; Petrykin, V.; Kakihana, M.; Kato, H.; Kudo, A., The relationship between photocatalytic activity and crystal structure in strontium tantalates. *J Catal* **2005,** *232* (1), 102-107.

15.   Kudo, A.; Kato, H.; Nakagawa, S., Water Splitting into H_2 and O_2 on New $Sr_2M_2O_7$ (M = Nb and Ta) Photocatalysts with Layered Perovskite Structures: Factors Affecting the Photocatalytic Activity. *The Journal of Physical Chemistry B* **2000,** *104* (3), 571-575.

16.   Shimizu, K.-i.; Tsuji, Y.; Hatamachi, T.; Toda, K.; Kodama, T.; Sato, M.; Kitayama, Y., Photocatalytic water splitting on hydrated layered perovskite tantalate $A_2SrTa_2O_7 \cdot nH_2O$ (A = H, K, and Rb). *Phys. Chem. Chem. Phys.* **2004,** *6* (5), 1064-1069.

17.   G. Kim, H.; W. Hwang, D.; Kim, J.; G. Kim, Y.; S. Lee, J., Highly donor-doped (110) layered perovskite materials as novel photocatalysts for overall water splitting. *Chem. Commun.* **1999,** (12), 1077-1078.

18.   Yao, W. F.; Ye, J. H., Photocatalytic properties of a new photocatalyst $K2Sr_{1.5}Ta_3O_{10}$. *Chemical Physics Letters* **2007,** *435* (1-3), 96-99.

19.   Osterloh, F. E., Inorganic materials as catalysts for photochemical splitting of water. *Chem. Mat.* **2008,** *20* (1), 35-54.

20.   Zhang, P.; Zhang, J.; Gong, J., Tantalum-based semiconductors for solar water splitting. *Chem. Soc. Rev.* **2014,** *43* (13), 4395-4422.

21.   Kanhere, P.; Chen, Z., A Review on Visible Light Active Perovskite-Based Photocatalysts. *Molecules* **2014,** *19* (12), 19995-20022.

22.   Kudo, A.; Miseki, Y., Heterogeneous photocatalyst materials for water splitting. *Chem. Soc. Rev.* **2009,** *38* (1), 253-278.

23.   Shi, J.; Guo, L., ABO_3-based photocatalysts for water splitting. *Progress in Natural Science-Materials International* **2012,** *22* (6), 592-615.

24.   Neri, G.; Walsh, J. J.; Wilson, C.; Reynal, A.; Lim, J. Y. C.; Li, X.; White, A. J. P.; Long, N. J.; Durrant, J. R.; Cowan, A. J., A functionalised nickel cyclam catalyst for CO_2 reduction: electrocatalysis, semiconductor surface immobilisation and light-driven electron transfer. *Phys. Chem. Chem. Phys.* **2015,** *17* (3), 1562-1566.

25.   Hu, C.-C.; Teng, H., Influence of structural features on the photocatalytic activity of $NaTaO_3$ powders from different synthesis methods. *Applied Catalysis a-General* **2007,** *331*, 44-50.

26.   Yokoi, T.; Sakuma, J.; Maeda, K.; Domen, K.; Tatsumi, T.; Kondo, J. N., Preparation of a colloidal array of $NaTaO_3$ nanoparticles via a confined space synthesis route and its photocatalytic application. *Phys. Chem. Chem. Phys.* **2011,** *13* (7), 2563-2570.

27.   Ishihara, T.; Baik, N. S.; Ono, N.; Nishiguchi, H.; Takita, Y., Effects of crystal structure on photolysis of H2O on K-Ta mixed oxide. *Journal of Photochemistry and Photobiology a-Chemistry* **2004,** *167* (2-3), 149-157.

28.   Husin, H.; Chen, H. M.; Su, W. N.; Pan, C. J.; Chuang, W. T.; Sheu, H. S.; Hwang, B. J., Green fabrication of La-doped $NaTaO_3$ via H_2O_2 assisted sol-gel route for photocatalytic hydrogen production. *Applied Catalysis B-Environmental* **2011,** *102* (1-2), 343-351.

29.   Schwickardi, M.; Johann, T.; Schmidt, W.; Schüth, F., High-Surface-Area Oxides Obtained by an Activated Carbon Route. *Chem. Mat.* **2002,** *14* (9), 3913-3919.

30.   Hu, C.-C.; Tsai, C.-C.; Teng, H., Structure Characterization and Tuning of Perovskite-Like NaTaO3 for Applications in Photoluminescence and Photocatalysis. *J. Am. Ceram. Soc.* **2009,** *92* (2), 460-466.

31.   Iwase, A.; Kato, H.; Kudo, A., The Effect of Alkaline Earth Metal Ion Dopants on Photocatalytic Water Splitting by $NaTaO_3$ Powder. *ChemSusChem* **2009,** *2* (9), 873-877.

32.   Iwase, A.; Kato, H.; Kudo, A., The effect of Au cocatalyst loaded on La-doped $NaTaO_3$ on photocatalytic water splitting and O_2 photoreduction. *Applied Catalysis B-Environmental* **2013,** *136*, 89-93.

33.   Grewe, T.; Meier, K.; Tueysuez, H., Photocatalytic hydrogen production over various sodium tantalates. *Catal. Today* **2014,** *225*, 142-148.

34.   Liu, J. W.; Chen, G.; Li, Z. H.; Zhang, Z. G., Hydrothermal synthesis and photocatalytic properties of $ATaO_3$ and $ANbO_3$ (A = Na and K). *Int. J. Hydrog. Energy* **2007,** *32* (13), 2269-2272.

35.   Shi, J.; Liu, G.; Wang, N.; Li, C., Microwave-assisted hydrothermal synthesis of perovskite $NaTaO_3$ nanocrystals and their photocatalytic properties. *J. Mater. Chem.* **2012,** *22* (36), 18808-18813.

36.   Chia, J. S. Y.; Tan, M. T. T.; Khiew, P. S.; Chin, J. K.; Siong, C. W., A bio-electrochemical sensing platform for glucose based on irreversible, non-covalent pi-pi functionalization of graphene produced via a novel, green synthesis method. *Sens. Actuator B-Chem.* **2015,** *210*, 558-565.

37.   Hu, C.-C.; Teng, H., Structural features of p-type semiconducting NiO as a co-catalyst for photocatalytic water splitting. *J Catal* **2010,** *272* (1), 1-8.

38.   Torres-Martinez, L. M.; Gomez, R.; Vazquez-Cuchillo, O.; Juarez-Ramirez, I.; Cruz-Lopez, A.; Alejandre-Sandoval, F. J., Enhanced photocatalytic water splitting hydrogen production on RuO_2/La $NaTaO_3$ prepared by sol-gel method. *Catalysis Communications* **2010,** *12* (4), 268-272.

39.   Maeda, K.; Teramura, K.; Lu, D.; Saito, N.; Inoue, Y.; Domen, K., Noble-Metal/Cr_2O_3 Core/Shell Nanoparticles as a Cocatalyst for Photocatalytic Overall Water Splitting. *Angewandte Chemie International Edition* **2006,** *45* (46), 7806-7809.

40.   Yang, J.; Wang, D.; Han, H.; Li, C., Roles of Cocatalysts in Photocatalysis and Photoelectrocatalysis. *Accounts Chem. Res.* **2013,** *46* (8), 1900-1909.

41.   Chen, X.; Shen, S.; Guo, L.; Mao, S. S., Semiconductor-based Photocatalytic Hydrogen Generation. *Chem. Rev.* **2010,** *110* (11), 6503-6570.

42.   Sze, S. M.; Ng, K. K., *Physics of semiconductor devices*. Wiley-Interscience: Hoboken, N.J., 2007.

43.   Kanno, H.; Yamamoto, Y.; Harada, H., TiO_2 based photocatalysts prepared from titanium isopropoxide and aqueous electrolyte solutions. *Chemical Physics Letters* **1985,** *121* (3), 245-248.

44.   Bamwenda, G. R.; Tsubota, S.; Nakamura, T.; Haruta, M., Photoassisted hydrogen production from a water-ethanol solution: a comparison of activities of Au-TiO_2 and Pt-TiO_2. *Journal of Photochemistry and Photobiology a-Chemistry* **1995,** *89* (2), 177-189.

45.   Iwase, A.; Kato, H.; Kudo, A., Nanosized Au Particles as an Efficient Cocatalyst for Photocatalytic Overall Water Splitting. *Catalysis Letters* **2006,** *108* (1-2), 7-10.

46.   Su, R.; Tiruvalam, R.; Logsdail, A. J.; He, Q.; Downing, C. A.; Jensen, M. T.; Dimitratos, N.; Kesavan, L.; Wells, P. P.; Bechstein, R.; Jensen, H. H.; Wendt, S.; Catlow, C. R. A.; Kiely, C. J.; Hutchings, G. J.; Besenbacher, F., Designer Titania-Supported Au-Pd Nanoparticles for Efficient Photocatalytic Hydrogen Production. *ACS Nano* **2014,** *8* (4), 3490-3497.

47.   Geim, A. K.; Novoselov, K. S., The rise of graphene. *Nat. Mater.* **2007,** *6* (3), 183-191.

48.   Lee, C.; Wei, X.; Kysar, J. W.; Hone, J., Measurement of the Elastic Properties and Intrinsic Strength of Monolayer Graphene. *Science* **2008,** *321* (5887), 385-388.

49.   Hu, Y. H.; Wang, H.; Hu, B., Thinnest Two-Dimensional Nanomaterial—Graphene for Solar Energy. *ChemSusChem* **2010,** *3* (7), 782-796.

50.   Song, J.; Yin, Z.; Yang, Z.; Amaladass, P.; Wu, S.; Ye, J.; Zhao, Y.; Deng, W.-Q.; Zhang, H.; Liu, X.-W., Enhancement of Photogenerated Electron Transport in Dye-Sensitized Solar Cells with Introduction of a Reduced Graphene Oxide–TiO_2 Junction. *Chemistry – A European Journal* **2011,** *17* (39), 10832-10837.

51.   Imran Jafri, R.; Rajalakshmi, N.; Ramaprabhu, S., Nitrogen doped graphene nanoplatelets as catalyst support for oxygen reduction reaction in proton exchange membrane fuel cell. *J. Mater. Chem.* **2010,** *20* (34), 7114-7117.

52.   Wu, Z.-S.; Ren, W.; Wen, L.; Gao, L.; Zhao, J.; Chen, Z.; Zhou, G.; Li, F.; Cheng, H.-M., Graphene Anchored with Co3O4 Nanoparticles as Anode of Lithium Ion Batteries with Enhanced Reversible Capacity and Cyclic Performance. *ACS Nano* **2010,** *4* (6), 3187-3194.

53.   Lu, C.-H.; Yang, H.-H.; Zhu, C.-L.; Chen, X.; Chen, G.-N., A Graphene Platform for Sensing Biomolecules. *Angewandte Chemie* **2009,** *121* (26), 4879-4881.

54.   Xiang, Q.; Yu, J.; Jaroniec, M., Graphene-based semiconductor photocatalysts. *Chem. Soc. Rev.* **2012,** *41* (2), 782-796.

55.   Geim, A. K., Graphene: Status and Prospects. *Science* **2009,** *324* (5934), 1530-1534.

56.   Zhang, Y.; Zhang, L.; Zhou, C., Review of Chemical Vapor Deposition of Graphene and Related Applications. *Accounts Chem. Res.* **2013,** *46* (10), 2329-2339.

57.   Sutter, P. W.; Flege, J.-I.; Sutter, E. A., Epitaxial graphene on ruthenium. *Nat Mater* **2008,** *7* (5), 406-411.

58.   Nethravathi, C.; Rajamathi, M., Chemically modified graphene sheets produced by the solvothermal reduction of colloidal dispersions of graphite oxide. *Carbon* **2008,** *46* (14), 1994-1998.

59.   Park, S.; Ruoff, R. S., Chemical methods for the production of graphenes. *Nat. Nanotechnol.* **2009,** *4* (4), 217-224.

60.   Soldano, C.; Mahmood, A.; Dujardin, E., Production, properties and potential of graphene. *Carbon* **2010,** *48* (8), 2127-2150.

61.   Sun, Z.; James, D. K.; Tour, J. M., Graphene Chemistry: Synthesis and Manipulation. *J. Phys. Chem. Lett.* **2011,** *2* (19), 2425-2432.

62.   Pei, S.; Cheng, H.-M., The reduction of graphene oxide. *Carbon* **2012,** *50* (9), 3210-3228.

63.   Huang, X.; Qi, X.; Boey, F.; Zhang, H., Graphene-based composites. *Chem. Soc. Rev.* **2012,** *41* (2), 666-686.

64.   Huang, C.; Li, C.; Shi, G., Graphene based catalysts. *Energy Environ. Sci.* **2012,** *5* (10), 8848-8868.

65.   Bianco, A.; Cheng, H. M.; Enoki, T.; Gogotsi, Y.; Hurt, R. H.; Koratkar, N.; Kyotani, T.; Monthioux, M.; Park, C. R.; Tascon, J. M. D.; Zhang, J., All in the graphene family - A recommended nomenclature for two-dimensional carbon materials. *Carbon* **2013,** *65*, 1-6.

66.   Williams, G.; Seger, B.; Kamat, P. V., TiO_2-graphene nanocomposites. UV-assisted photocatalytic reduction of graphene oxide. *ACS Nano* **2008,** *2* (7), 1487-1491.

67.   Manga, K. K.; Zhou, Y.; Yan, Y. L.; Loh, K. P., Multilayer Hybrid Films Consisting of Alternating Graphene and Titania Nanosheets with Ultrafast Electron Transfer and Photoconversion Properties. *Adv. Funct. Mater.* **2009,** *19* (22), 3638-3643.

68.   Akhavan, O.; Ghaderi, E., Photocatalytic Reduction of Graphene Oxide Nanosheets on TiO_2 Thin Film for Photoinactivation of Bacteria in Solar Light Irradiation. *J. Phys. Chem. C* **2009,** *113* (47), 20214-20220.

69.   Mukherji, A.; Seger, B.; Lu, G. Q.; Wang, L. Z., Nitrogen Doped $Sr_2Ta_2O_7$ Coupled with Graphene Sheets as Photocatalysts for Increased Photocatalytic Hydrogen Production. *ACS Nano* **2011,** *5* (5), 3483-3492.

70.   Mitchell, R. H.; Liferovich, R. P., A structural study of the perovskite series $Ca_{1-x}Na_xTi_{1-x}Ta_xO_3$. *Journal of Solid State Chemistry* **2004,** *177* (12), 4420-4427.

71.   Hummers, W. S.; Offeman, R. E., Preparation of Graphitic Oxide. *J. Am. Chem. Soc.* **1958,** *80* (6), 1339-1339.

72. Marcano, D. C.; Kosynkin, D. V.; Berlin, J. M.; Sinitskii, A.; Sun, Z.; Slesarev, A.; Alemany, L. B.; Lu, W.; Tour, J. M., Improved Synthesis of Graphene Oxide. *ACS Nano* **2010,** *4* (8), 4806-4814.

73. McAllister, M. J.; Li, J.-L.; Adamson, D. H.; Schniepp, H. C.; Abdala, A. A.; Liu, J.; Herrera-Alonso, M.; Milius, D. L.; Car, R.; Prud'homme, R. K.; Aksay, I. A., Single sheet functionalized graphene by oxidation and thermal expansion of graphite. *Chem. Mat.* **2007,** *19* (18), 4396-4404.

74. Dubin, S.; Gilje, S.; Wang, K.; Tung, V. C.; Cha, K.; Hall, A. S.; Farrar, J.; Varshneya, R.; Yang, Y.; Kaner, R. B., A One-Step, Solvothermal Reduction Method for Producing Reduced Graphene Oxide Dispersions in Organic Solvents. *ACS Nano* **2010,** *4* (7), 3845-3852.

75. Dikin, D. A.; Stankovich, S.; Zimney, E. J.; Piner, R. D.; Dommett, G. H. B.; Evmenenko, G.; Nguyen, S. T.; Ruoff, R. S., Preparation and characterization of graphene oxide paper. *Nature* **2007,** *448* (7152), 457-460.

76. Buchsteiner, A.; Lerf, A.; Pieper, J., Water dynamics in graphite oxide investigated with neutron scattering. *Journal of Physical Chemistry B* **2006,** *110* (45), 22328-22338.

77. Guardia, L.; Villar-Rodil, S.; Paredes, J. I.; Rozada, R.; Martinez-Alonso, A.; Tascon, J. M. D., UV light exposure of aqueous graphene oxide suspensions to promote their direct reduction, formation of graphene-metal nanoparticle hybrids and dye degradation. *Carbon* **2012,** *50* (3), 1014-1024.

78. Jo, G.; Choe, M.; Cho, C.-Y.; Kim, J. H.; Park, W.; Lee, S.; Hong, W.-K.; Kim, T.-W.; Park, S.-J.; Hong, B. H.; Kahng, Y. H.; Lee, T., Large-scale patterned multi-layer graphene films as transparent conducting electrodes for GaN light-emitting diodes. *Nanotechnology* **2010,** *21* (17).

79. Su, C.; Acik, M.; Takai, K.; Lu, J.; Hao, S.-J.; Zheng, Y.; Wu, P.; Bao, Q.; Enoki, T.; Chabal, Y. J.; Loh, K. P., Probing the catalytic activity of porous graphene oxide and the origin of this behaviour. *Nature Communications* **2012,** *3*.

80. Sun, Y.; Egawa, T.; Zhang, L. Y.; Yao, X., Novel method to directly prepare high-surface-area anatase titania nanoparticles with trapped electrons on oxygen vacancies. *Journal of Materials Science Letters* **2003,** *22* (11), 799-802.

81. Wohlrab, S.; Weiss, M.; Du, H.; Kaskel, S., Synthesis of $MNbO_3$ nanoparticles (M = Li, Na, K). *Chem. Mat.* **2006,** *18* (18), 4227-4230.

82. Priebe, J. B.; Karnahl, M.; Junge, H.; Beller, M.; Hollmann, D.; Brückner, A., Water Reduction with Visible Light: Synergy between Optical Transitions and Electron Transfer in Au-TiO2 Catalysts Visualized by In situ EPR Spectroscopy. *Angewandte Chemie International Edition* **2013,** *52* (43), 11420-11424.

4. Multicomponent aerogel architectures

4.1 Scope of this chapter

The main idea of the proposed approach is to retain the high surface area of nanosized photocatalysts by building aerogel architectures. The aerogel approach provides a suitable platform or support and it enables the addition of materials that may enhance the photocatalytic activity such as preformed nanoparticles (acting as co-catalyst) by just adding the desired co-catalyst during the gelation step. Furthermore, additives insertion during the formation of aerogels is fundamental to overcome the problem of the wide band gap of TiO_2 and to increase its photoreactivity and photostability.

The development of photocatalyst materials is more and more directed towards the combination of single components to obtain multifunctional materials. Thus, beside photocatalyst synthesis its mixing with other activity enhancing materials plays a significant role in light-driven photocatalytic water splitting and photoelectrochemical hydrogen generation. In the previous chapter 3, the particle size influence of $NaTaO_3$ semiconductors decorated with gold nanoparticles (NP) dispersed in a solution mixture containing conducting multilayer reduced graphene oxide (m-rGO) on the photocatalytic water splitting was investigated.[1] Although the catalytic performance was remarkably increased in the case of nanoscale $NaTaO_3$, the interactions between the multilayer graphene oxide and the catalyst are rather random since no chemical or physical attachment of the components was achieved. Likewise, Rolison and co-authors reported plasmonic enhancement of visible light driven splitting of water at 3D network gold-titania (Au-TiO_2) aerogels. The Au-TiO_2 anatase porous composite architecture with $1 - 8.5\%$ Au nanoparticles retained the high surface and mesoporosity of unmodified TiO_2 and also maintained a stable dispersion of the gold nanoparticles guests.[2]

The current chapter will give an overview of the concept of aerogel architectures including its processing and drying procedures, also the main advances will be briefly addressed. Moreover, synthesis, properties, modifications and the main achievements obtained with TiO_2 powder materials within the field of photocatalysis are discussed.

Aerogels are a class of highly porous materials that combine unique properties like high specific surface area, low density and low thermal conductivity in a continuous 3D network of meso- to micropores as presented schematically in Figure 4.1a. These properties make them attractive for photocatalytic applications.[3-7] Hence, the approach presented here could lead to the combination of a number of desired properties at the composite architectures, such as high surface area, a mesoporous network, hetero-junction, photoactivation of the semiconductor, extended sunlight absorption and charge transfer. These properties can be obtained for instance by the addition of: co-catalyst to act as electron trap, anion or ion doping to increase the photoactivation, sensitization by

dyes or quantum dots to extend sunlight absorption, crystal facet engineering by exposing reactive facets and a charge transfer promoter such as the graphene-like materials. In this context, the multicomponent aerogel strategy reported by Niederberger et al. provided a good concept by physically combining several different materials into a single architecture based on a TiO_2 model system. Such an assembly of multicomponent aerogels and their application in photocatalytic H_2 production is shown in Fig. 4.1 and Figure 4.2. The photocatalysts consist of chemically synthesized conductive carbon layers (multilayer reduced graphene oxide – m-rGO) and either chemically synthesized platinum nanoparticles or laser ablated metallic particles in liquid solution (physical method), embedded in a porous semiconductor TiO_2 anatase matrix. The combination of catalytically active and conducting components in aerogels leads to an increase in photocatalytic activity. The data and results obtained in this chapter were published elsewhere.[9]
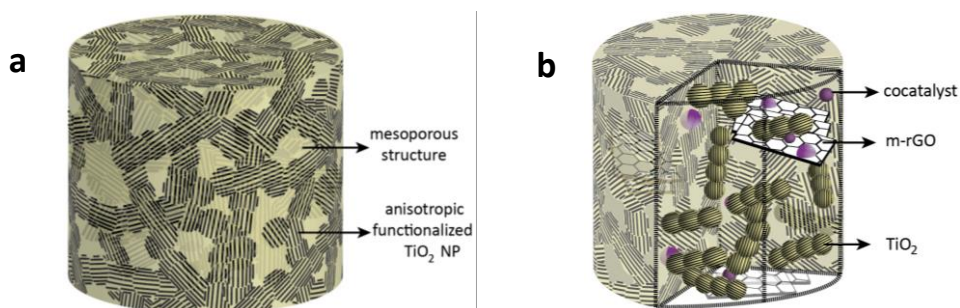
Figure 4.1 TiO_2 aerogel architecture scheme (a) including the porous network connected by the functionalized TiO_2 nanoparticles. Multicomponent aerogel is depicted in (b) where additives such as cocatalyst and conductive carbon layers can be inserted into the aerogel network.
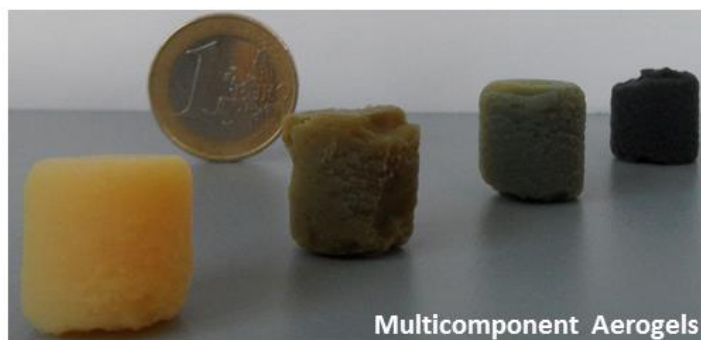
Figure 4.2 Aerogel and multicomponent aerogel monoliths produced after supercritical drying. From left to right: pure TiO_2, TiO_2 loaded with 0.4 wt% Pt, TiO_2 loaded with 0.4 wt.% Pt and 1 wt.% m-rGO, TiO_2 loaded with 10 wt% m-rGO.

4.2 Nanoscale titanium dioxide (TiO_2): Synthesis, properties and modifications

Titanium (IV) oxide is one of the most studied materials in the field of chemical catalysis and surface science.[10-14] It crystallizes into three major polymorphs of decreasing stability[*]: rutile,

---

[*] For the sake of simplicity, I will just use rutile, anatase or brookite to refer to TiO_2 and the specific phase as a whole. Example: Anatase = TiO_2 with anatase phase; rutile = TiO_2 with rutile phase and so on.

brookite and anatase respectively.[15] Their unit cells are built of the same Ti-O_6 octahedral building units but connected slightly different depending on the polymorph.

The last decades was characterized by an exponential growth of research in nanoscience and its related fields with TiO_2 being one of the prominent components in nanoscience and photocatalysis. Recently, Fresno et al. surveyed the photocatalysis research conducted exclusively with titania and/or as one of the photocatalyst components, as a result the following was described[†]: (i) TiO_2 is still the most used photocatalyst (currently, over 40% of all research articles using photocatalysts are based on TiO_2), especially the use of anatase and anatase-rutile mixture phases as benchmark semiconductors is remakable; (ii) Strong predominance of TiO_2 during the 90's until reach a plateau during the 2000's which corresponded to 60% of all photocatalysts surveyed; (iii) End of the 2000 decade is observed by the decay of TiO_2 preponderance due to the exploration of new materials and the search for active photocatalysts under visible light.[16]

The synthesis of nanostructured TiO_2 is very well documented in the literature: from monodisperse to all sorts of sizes and shapes through control of the assembly process. Examples of these structures are nano-rods, -wires and -tubes, multiple size spheres, whiskers, platelets, thin films, mesoporous titania and even aerogel structures made of TiO_2, which will be described in the current chapter.[13-23] TiO_2 nanoparticles can be obtained by a broad variety of synthesis methods such as sol gel,[24] non-aqueous sol gel,[25] ionic liquids,[26] chemical vapor deposition,[27] electrodeposition,[28] sonochemical,[29] microwave assisted[30] for instance, to mention just a few.

Sol gel processes are being considered as very powerful chemical routes to obtain inorganic materials at mild temperatures. They are based on the hydrolysis and condensation of molecular precursors such as metal salts, alkoxides or metal halides.[24] However, one main drawback is the lack of control of the reaction rates that are often too fast, resulting in the loss of microstructural control (i.e. crystallinity, phase, particle size and morphology). Additionally, the as-synthesized metal oxides are often amorphous, and a further annealing step is necessary, but as a result it becomes difficult to retain full control over the crystallization process during this step. To overcome the aforementioned lack of reaction control, the "aqueous" sol-gel method evolved into nonaqueous sol-gel methods, resulting in better control over particle sizes, morphologies and crystallinity, and still at mild temperatures. The substitution of water as solvent (in the sol gel method) by organic solvents like alcohols, ketones, aldehydes or ethers (in non-aqueous sol gel methods) resulted in lower reaction rates, mainly as a result of the moderate reactivity of the C-O bond, in combination with the stabilizing effects of the organic species. The introduction of these aspects may lead to uniform crystalline nanoparticles obviating the need of the additional annealing step.[31,32] The versatile non-

---

[†] Period in context from 1990-2014

aqueous sol-gel approach allowed us to produce titania nanoparticles in the form of the aerogel architecture.

Finally, Banfield et al. reported that under ambient conditions rutile is thermodynamically stable relative to anatase or brookite. However, thermodynamic stability is particle-size dependent, and at particle diameters below ca. 14 nm, anatase is more stable than rutile.[15,33] This explains why anatase can be obtained in nano sizes and the predominance of anatase in the fields of heterogeneous catalysis, including sensitized solar cells and photocatalysis. [10,13,34,35] Titania is an extensively investigated photosemiconductor used for photocatalytic water splitting, because of the following features: (i) it is cheap and abundant material available on industrial scale[‡]; (ii) possess chemical and corrosion resistant; (iii) nontoxic and (iv) high absorption in the UV region, conduction and valence band energy potentials are suitable for the redox potentials of water, as discussed in chapter 2.

4.2.1 Nanoscale TiO_2 modifications: Photocatalytic enhancement

Photocatalysis research using titanium oxide materials is basically focused on two pathways. The first is concentrated on the enhancement of photocatalytic H_2 production by the addition of additives (e.g. noble metal loading as co-catalysts, other additives like) or conductive carbon sheets, (m-rGO) and the second pathway is focused on narrowing the TiO_2 band gap in order to enhance the TiO_2 materials visible light absorption. As previously described in chapter 3.3 the loading of noble metals and metal alloys (as cocatalyst) plays a significant role in photocatalysis enhancement. Noble metals like Pt, Rh, Au, Ag, Pd, and Cu, or Ni,[36-41] as well as noble alloys like Au-Pd, Au-Cu and Pt-Cu have been reported to be very effective, especially together with a TiO_2 semiconductor.[42-44] However, the description of electron donors and crystal facet engineering are missing in order to provide the full panorama of the hydrogen enhancement techniques. The addition of electron donors i.e. hole scavengers or sacrificial reagents to consume the photogenerated valence band holes may enhance the photocatalytic electron-hole separation, while the generated electrons in the conduction band can reduce protons resulting in hydrogen molecules. However, continuous addition of electron donors is required to keep the hydrogen production alive. In general, organic compounds are widely used as electron donors like EDTA, methanol, ethanol, lactic acid, ascorbic acid and formaldehyde for instance.[36,45-47] Since, adding methanol to pure water can play a crucial role in enhancing hydrogen generation, several reports proposed possible mechanisms for the photocatalytic oxidation of methanol.[48-51] Therefore, two possible mechanisms were identified (i) direct oxidation by

---

[‡] Annual global production of TiO_2 is over 4 million metric tons estimated in a US\$ 14 billion business. Source: Cristal Global Company and TiO_2 pigment Annual Review (2012). Five global producers make up nearly 60% of the global nameplate capacity: DuPont, Cristal Global, Tronox, Huntsman and Kronos.

photogenerated holes and (ii) indirect oxidation via interfacial formed $^\bullet$OH radicals, that is the product of trapped VB holes by surface –OH groups or adsorbed water molecules. Using isotopic labelling and temperature programmed desorption in combination with laser surface photocatalysis Chenbiao et al. investigated the molecular hydrogen formation from photocatalysis on TiO_2 rutile (110)[§]. The authors provided significant evidence that molecular hydrogen may be produced via thermal recombination reaction of hydrogen atoms on the bridged-bond oxygen (in the exposed TiO_2 surface), produced by methanol photocatalysis on TiO_2 rutile (110) under 400 nm irradiation. This may well a possible universal mechanism for H_2 generation using titania-based catalysts.[52,53]

Since the remarkable work of Lu and co-authors in 2008, the development and advances in crystal facet engineering of semiconductor photocatalysts increased tremendously, because facet engineering enables the tuning of properties such as reactivity and selectivity of photosemiconductors, especially in the case of TiO_2 anatase.[54] A TiO_2 anatase crystal is usually dominated by {101} facets (yellow facets in Figure 4.3), which present the lowest surface energy as depicted in Figure 4.3.[55] Considering other facets, theoretical studies have demonstrated the following sequence for surface relative energies: {101} < {100} < {001}.[54] An inversion in the sequence position between the {101} and {100} facets can occur; e.g., in oxygenated surfaces, {100} facets are mostly stable whereas under clear and hydrogenated conditions, {101} facets are more stable. However, the {001} facets (green facet in Figure 4.3) has the highest energy. The relative energy variations of these surfaces can be explained by the different chemical compositions of the facets, resulting in diverse degrees of broken chemical bonds on the surface. Lu and co-authors reported the preparation of anatase microcrystals with surfaces formed preferentially by {001} facets.

On the basis of first-principle quantum chemistry calculations, the strategy used by them was the reversal of the relative stability of the facets through the use of fluoride ions during the synthesis.
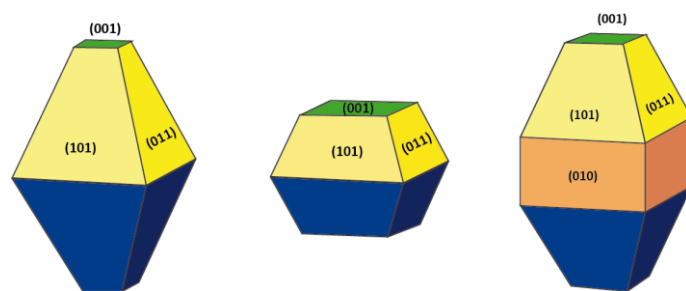
Figure 4.3 Crystal morphology predicted for anatase TiO_2 using Wulff's construction[**]. Every crystal facet is represented by different colours (which correspond to different planes i.e. (101), (001), (011), (010) and all the related family planes).

[§] TiO_2 rutile (110) according to Wulff's construction is one of the equilibrium shapes (or crystal facet) present in the TiO_2 rutile crystal.
[**] Wulff construction is a mathematical method of predicting the equilibrium shape of nanoparticles given the surface energies of the material.

The presence of fluoride ions favors the formation of strong F–Ti bond at the surface, leading to a decrease in the (001) surface energy, which results in a higher stability than the (101) surface. Then Zheng and co-workers used a similar approach to synthesize anatase TiO_2 nanosheets with exposed {001} facets and excellent photocatalytic activity towards the degradation of organic pollutants such as methyl orange was achieved.[56]

4.2.2 Nanoscale TiO_2 modifications: extending solar absorption

This section describes the methods used to extend the TiO_2 solar spectrum absorption, because the solar-driven photocatalytic process of unmodified[††] titania is highly limited by its wide band gap (3.2 eV), which is only excited by UV light which comprises approx. 5% of the solar spectrum. This fact has inspired an intensive effort to promote the photocatalytic activity and enhance the visible light response. Briefly, the strategies that have been employed to enhance the visible light response for TiO_2 materials are: dye sensitization, metal ion doping and non-metal doping strategies.

Dye sensitization is a low cost concept developed by O'Regan and Grätzel in the early 90's to improve the efficiency of solar cells by using TiO_2 as photocatalyst combined with a ruthenium complex - $[Ru(bpy)_3]^{2+}$ known as a dye, which enables visible-light harvesting of wide-bandgap semiconductors such as TiO_2 through sensitization, achieving an overall light-to-electric energy conversion yield of 12% under solar light.[35] Sensitization is based on the redox properties of some dyes, which under visible light illumination can promote the excited electrons to the conduction band of photosemiconductors to initiate catalytic reactions, as summarized in scheme 4.1, including water splitting.[57,58,59] Among the various dyes successfully applied in sensitization processes one can mention the following: metal complexes (e.g., Ru or Pt complexes,[60,61] metalloporphyrins,[62] and phthalocyanines[63]) and organic dyes (e.g., eosin Y and Rhodamine B,[64] rose Bengal,[65] merocyanine and coumarin,[66] porphine,[67] and binaphthol[68]) have been used as sensitizers for H_2 production under visible-light irradiation. The equations below (eq. 4.1 – 4.3) illustrate the electron excitation, injection and possible dye regeneration.[35] A very illustrative example was reported by Peng et al., where highly efficient visible light induced photocatalytic H_2 production was achieved using TiO_2 sensitized with $[Ru_2(bpy)_4(BL)](ClO_4)_2$ without the presence of a co-catalyst.[69] In this report, the amount of evolved H_2 after 27 h of irradiation corresponds to a turnover number of about 75340, and the apparent quantum yield is estimated to be 7.3% under 475 nm monochromatic light irradiation.

[††] Unmodified in this context, was used with the meaning of pure or bare titania.

$$dye \xrightarrow{h\nu} dye^* \tag{4.1}$$

$$dye^* \xrightarrow{TiO_2} dye^+ + e^- \tag{4.2}$$

$$dye^+ + e^- \longrightarrow dye \tag{4.3}$$
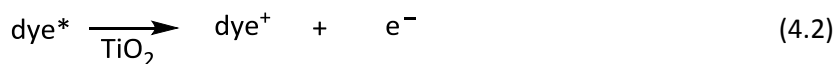
Scheme 4.1 Possible sensitization mechanism: dye excitation (Eq. 4.1), electron injection (Eq. 4.2) and dye regeneration (Eq. 4.3).

However, photosemiconductor sensitization still possesses drawbacks concerning dye desorption and backward transfer (recombination) during the photoreaction. Moreover the long-term stability of the dyes is still far from desirable.

Metal ion doping with transition or rare earth metals[‡‡] may also be employed in photocatalytic applications. Hoffmann et al. performed a systematic investigation of the photocatalytic activity of TiO_2 nanoparticles doped with 21 different metals (usually in the form of a metal salt) to evaluate the oxidation of $CHCl_3$ and the reduction of CCl_4. The authors concluded that the ability of a dopant to function as an effective trap is influenced by the dopant concentration, the energy levels generated by the dopants within the TiO_2 lattice, their electronic configuration and finally by the distribution of dopants within the particles.[70] Within the 21 different metals tested 12 showed lower and/or similar photocatalytic activity than undoped TiO_2, while TiO_2 doped with Ru^{3+} resulted in the highest activity of nearly 11 fold compared with bare TiO_2. Metal ion doping may promote a slightly higher TiO_2 absorption in the visible region, however the down side is an increase of the carrier-recombination centers, which may degrade the electron–hole separation ability and cause electron–hole recombination at the dopant sites.

In 2001, in a completely new approach, Asahi et al. used first principle calculations to predict band gap narrowing by a series of non-metallic substitutional dopants such as C, N, F, P and S to replace the O (at a doping level) in the anatase TiO_2 crystal. The substitutional doping of N was the most effective according to the authors, because its p states contributed to the band gap narrowing by mixing with O 2p states. In spite of the fact that doping with S also contributes to band narrowing, the large ionic radius of sulfur makes its incorporation into TiO_2 lattice difficult. Nitrogen doped TiO_2 thin film was prepared by sputtering and the resulting film was reported to be catalytically active for methylene blue decomposition under visible light.[71] In the following year, another group published efficient photochemical water splitting by a chemically modified TiO_2 using flame pyrolysis synthesis. The as obtained TiO_2 was doped with carbon which extended its absorption below 535 nm and

---

[‡‡] The main difference between metal loading (i) and ion doping (ii) relies in the nature and where the metallic species are located. In (i) the metallic species are made of particles or clusters and are situated in the surface of the photocatalyst, while (ii) the metal ions are inserted into the photosemiconductor lattice as impurities.

narrowed its band gap to 2.32 instead of the actual 3 eV for bulk TiO_2 rutile. The performance of C doped TiO_2 produced by this method resulted in water splitting with a total conversion efficiency of 11% at an applied potential of 0.3 Volt, under UV-Vis illumination.[72] Until now, nitrogen-doped TiO_2 exhibits the highest optical response to radiation with visible light, but its absorption in the visible and infrared still remains insufficient. In 2011, an innovative approach was presented by Mao and co-authors that succeeded to narrow TiO_2 the band gap to an exceptional 1.54 eV[§§], which significantly enhanced its photocatalysis. The method consisted of hydrogenation of TiO_2 nanocrystals at a relative high pressure (20 bars) producing black TiO_2.[73] Its photocatalytic activity was measured thorough the decomposition of methylene blue and phenol under simulated solar light. The black TiO_2 bleached the methylene blue solution at a rate 6.25 faster than unmodified TiO_2 and twice as fast in phenol degradation. The material was also tested for hydrogen evolution achieving rates of 10 $mmolh^{-1}$ loaded with platinum co-catalyst under simulated solar light. The black TiO_2 photocatalyst was submitted to long-term testing achieving consecutive cycles of 13 and 22 days, with persistent high rates of H_2 evolution throughout the cycles. Although one would expect that hydrogen thermal treatment of TiO_2 nanocrystals would result in reduction of Ti^{4+} to Ti^{3+} species or even to the metallic state, it resulted in the so called disorder-engineered black TiO_2 nanocrystals.[73] Thus, the activity of disorder titanium dioxide nanocrystals in the visible light region is still far from satisfactory, although black titania nanomaterials have shown large capabilities in absorbing a remarkable amount of sunlight and have been reported to possess visible-light photocatalytic and photoelectrochemical activities.[74-77]

4.3 Inorganic oxide aerogels: Properties, sol-gel synthesis, processing and drying

The pioneering work with silica gels from Samuel Stephens Kistler in 1931 gave birth to the term and provided a material with unique properties called aerogel (air + gel),[78] which is used or considered for use in a wide range of applications,[79] including optical[80,81] and chemical sensing,[82] thermal insulation[83] and acoustic insulation, super-hydrophobic surfaces[84,85], aerospace and space exploration,[86] nuclear particle detection (Cherenkov detector),[87,88] and catalysis which is the main focus of the present chapter.[89-93]

An aerogel is a three dimensional open network which can be assembled from nanoparticles or polymer molecules or as Kistler proposed: "an aerogel is a gel in which the liquid has been replaced by air by some means, with slightly moderate shrinkage of the solid network".[3,94] The proposed definition for aerogel by IUPAC is "gel comprised of a microporous solid in which the dispersed phase is a gas". Commonly, the aerogels precursors (wet gels) are synthesized by sol-gel chemistry, i.e. the main reactions involved are hydrolysis and condensation of a metal salt or metal alkoxide as

---

[§§] This approach performed by Mao et al. could not be reproduced by us.

summarized in scheme 4.2.[3] These reactions result in a continuously connected, solid network that is filled with solvent called wet-gel, as depicted in Fig. 4.4. Furthermore, the overview of the methods and processes involved during aerogel preparation are highlighted in Fig. 4.4. One major problem in preparing aerogels is the extraction of the solvent without collapsing the existing porous network structure. Fig. 4.4 illustrates the main difference (shrinkage) between applying supercritical drying versus conventional drying techniques, e.g. ambient air, oven or vacuum drying, which are not able to preserve the wet gel structure leading to xerogels.

According to Shen et al. aerogels can be classified by their composition in 2 main categories: single component aerogels and aerogel composites. As single components one can refer to silica (SiO_2) or non-silica (ZrO_2, NiO, CoO, TiO_2, Al_2O_3 etc), organic aerogels (resorcinol-formaldehyde, hydrogel[***] and cellulose-based)[95,96], carbon aerogels (carbonized resorcinol formaldehyde, carbon nanotubes and graphene)[93, 97] chalcogenide aerogels (CdTe, CdSe and ZnSe)[81, 98], metal or metal alloys aerogels (Au, Ag and Ag/Au, Ag/Pt).[99] Aerogel composites comprise countless combinations of single components at different ratios.[2, 92, 100]

All aerogels with few exceptions (i.e. organic and chalcogenides) are prepared by the sol-gel method. The sol-gel process is a wet-chemical method which provides solid materials such as particles, ceramics or glasses (i.e. silicates and metal oxides) starting from molecular precursors throughout inorganic polymerization until an oxide network is obtained. Depending on the nature of the precursors, sol-gel processes can be classified into two routes (i) hydrolytic – when the precursor is an inorganic salt or a hydrolysable compound (e.g. alkoxide) and water is used as solvent. The main hydrolysis and condensation reactions are illustrated by the chemical equations 4.4, 4.5 and 4.6 or (ii) non-hydrolytic – when the precursor is a metal organic compound, alkoxide or salt and organic solvent is used instead. The main condensation reactions can be illustrated by the equations 4.7 – 4.9. The aqueous chemistry of inorganic salts has several disadvantages due to the occurrence of hydrolysis reactions which convert the ions into new ionic species or to precipitates. The transition metal chemistry in aqueous solutions can be challenging because of the formation of various oligomeric species (from dimer to tetramer for instance), due to the occurrence of multiple oxidation states, in dependence on the pH and the concentration. Furthermore, the counter anions can influence the morphology and chemical composition of the obtained solid phase. However, several of these disadvantages can be circumvented by adopting a non-hydrolytic pathway i.e. by using metal organic molecular precursors such as metal chlorides, alkoxides, or acetylacetonates.[25, 31-32] Metal chlorides $M(Cl)_n$ and alkoxides $M(OR)_n$ for instance, are versatile molecular precursors for the sol-gel synthesis of metal oxides.

[***] Hydrogels are formed by crosslinking polymer chains and are well known for their ability to absorb substantial amounts of water.

$$\overset{\diagdown}{\underset{\diagup}{-}}\!M-OR \ + \ H_2O \ \longrightarrow \ \overset{\diagdown}{\underset{\diagup}{-}}\!M-OH \ + \ ROH \tag{4.4}$$

$$\overset{\diagdown}{\underset{\diagup}{-}}\!M-OH \ + \ OH-M\overset{\diagup}{\underset{\diagdown}{-}} \ \longrightarrow \ \overset{\diagdown}{\underset{\diagup}{-}}\!M-O-M\overset{\diagup}{\underset{\diagdown}{-}} \ + \ H_2O \tag{4.5}$$

$$\overset{\diagdown}{\underset{\diagup}{-}}\!M-OR \ + \ HO-M\overset{\diagup}{\underset{\diagdown}{-}} \ \longrightarrow \ \overset{\diagdown}{\underset{\diagup}{-}}\!M-O-M\overset{\diagup}{\underset{\diagdown}{-}} \ + \ ROH \tag{4.6}$$
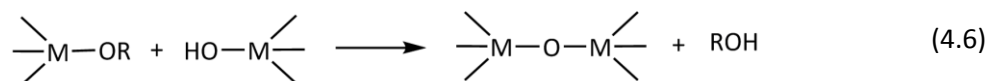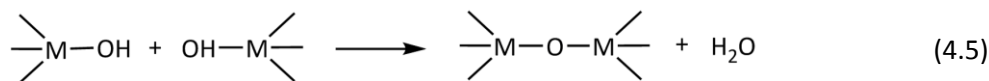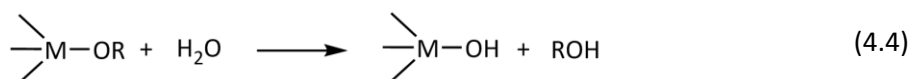
Scheme 4.2 Chemical reactions for the sol-gel process using metal alkoxides. Hydrolysis (Eq. 4.4) and condensation, involving oxolation (Eq. 4.5) and alkoxolation (Eq. 4.6), where M represents a metal species and R alkyl groups.

Because of their solubility in organic solvents, a high homogeneity and easy conversion into their corresponding oxide is possible. The main non-hydrolytic routes reported by Vioux et al. and Niederberger et al. involve the reaction of a metal chloride with either metal alkoxides or acetylacetonates or alcohols, acting as oxygen donors (equations 4.7, 4.8 and 4.9).[25,31-32] Hence, the advantage of the non-hydrolytic sol-gel process results from the coordinating effect of the organic solvent and the moderate reactivity of the C-O bond which is responsible for the slow reaction rates. The advantages are a simplified synthesis delivering high purity crystalline products within the nanoscale range, control over particle size and shape. In addition, it allows the control over surface and assembly properties.[†††]

Metal oxides are the most studied class of aerogels components, the earliest studies started with silica aerogels. Studies conducted by Kistler followed with a series of single metal oxide compositions such as alumina, zirconia, titania, nickel oxide, cobalt oxide and mixed oxide aerogels.[101] However, most of the approaches used to obtain these metal oxides are based on hydrolytic sol-gel process which leads to amorphous solid products. Consequently, the as-obtained aerogel must be annealed above 400°C to induce crystallization. Unfortunately, the high temperatures can provoke particle growth, collapse of the pores and reduction of specific surface area.

The aerogel approach adopted throughout this chapter is based on the non-aqueous sol-gel process between a metal halide (TiCl$_4$) and an alcohol (benzyl alcohol) which leads to TiO$_2$ nanocrystals and benzyl chloride as main products in accordance to eq. 4.9 in scheme 4.3. Although several mechanistic investigations involving the reaction of metal halides and alcohols or with metal alkoxides were reported on the formation of metal oxide.

[†††] It is well known, that in aqueous sol gel synthesis the hydrolysis and reaction rates are so fast that amorphous materials are often obtained, so additional annealing is needed to achieve crystalline materials to the detriment of controlling particle size and morphology.

$$MCl_x \;+\; y\,ROH \;\longrightarrow\; (RO)_y\,(MCl)_{x-y} \;+\; y\,HCl \qquad\qquad (4.7)$$

$$\text{>M-OR} \;+\; \text{RO-M<} \;\longrightarrow\; \text{>M-O-M<} \;+\; ROR \qquad\qquad (4.8)$$

$$\text{>M-Cl} \;+\; \text{RO-M<} \;\longrightarrow\; \text{>M-O-M<} \;+\; RCl \qquad\qquad (4.9)$$

$$\text{>M-O-}\underset{O}{\overset{\parallel}{C}}\text{R'} \;+\; \text{RO-M<} \;\longrightarrow\; \text{>M-O-M<} \;+\; RO\underset{O}{\overset{\parallel}{C}}R' \qquad\qquad (4.10)$$
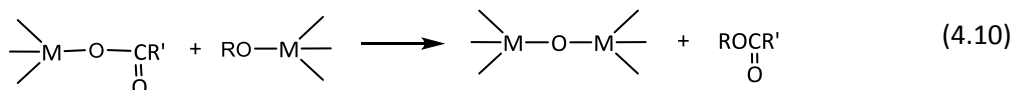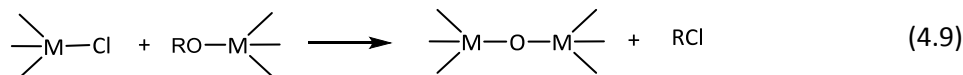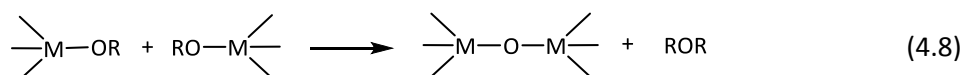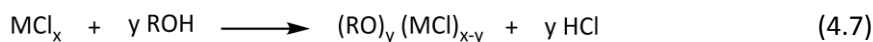
Scheme 4.3 Chemical reactions for the non-hydrolytic sol-gel process forming the M–O–M bond. The metal alkoxide species are generally produced in situ by the alcoholysis of metal halides reacting to the respective metal alkoxo-halide and hydrogen halide (Eq. 4.7); Ether elimination (Eq. 4.8); Alkyl halide elimination (4.9) and ester elimination (4.10); where R can be an alkyl or phenyl group and M is the metal specie.

The underlying reactions are still not completely understood.[25, 102,103] Scheme 4.4 shows a non-hydrolytic hydroxylation method as a result of the reaction between an alcohol and a metal halide. According to a previous report the reaction of tertiary and benzyl alcohols leads to a alkyl halide elimination following the pathway (b), but when primary and secondary alcohols are used, mechanisms (a) can occur.[103] These reaction pathways (a and b) seem to be plausible, because both involve initially the nucleophilic attack of the lone pair of electrons of an alcoholic oxygen atom to the metal center, followed by the cleavage of either the hydroxyl or alkoxyl group. Thus, alcohols with electron-donating groups (such as tertiary carbon and benzyl groups) lead to hydroxylation pathway (b) with alkyl halide elimination while alcohols containing electron-withdrawing groups prefer to directly eliminate hydrogen halide following the pathway (a).
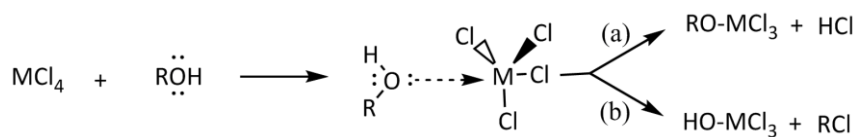
Scheme 4.4 Possible mechanism pathway for non-hydrolytic hydroxylation.

The preparation process of the aerogel includes three key steps, as shown in the Fig. 4.4.

(i) Solution-sol transition: conversion of the homogeneous metallic salt or alkoxide solution into a sol by hydrolytic or nonhydrolytic reaction.

(ii) Sol-wet-gel transition (gelation): the sol particles are further cross-linked (condensation reaction) and assembled into a wet gel continuous network.

(iii) Gel-aerogel transition (drying): the solvent inside the wet gel is replaced by air through supercritical drying, which prevents the pores inside the continuous network to collapse.
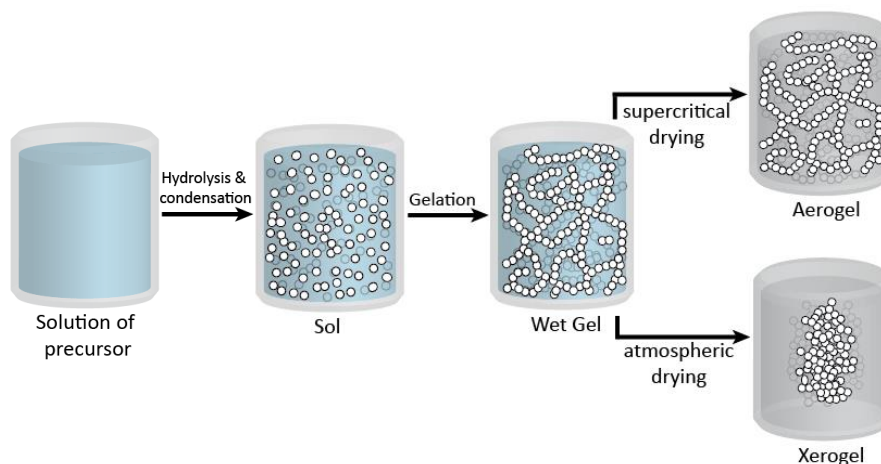
Figure 4.4 General processes and methods involved in the preparation of xerogels and aerogels. The main difference between aerogels and xerogels relie in the wet-gel structure shrinkage extent. Supercritical drying is used to preserve the full wet-gel structure with minimum shrinkage.

4.4 Supercritical Drying

The effective solvent extraction from a wet gel phase while keeping the porous network unaltered is just possible by employing supercritical drying. Supercritical drying avoids a liquid-phase by submitting the solvent above its critical point whereupon it becomes a supercritical fluid. Under supercritical conditions the fluid has properties of both liquid and gas and is characterized by having no interface or surface tension. Once the supercritical condition is achieved the fluid is then slowly depressurized into the gas phase and the solid is preserved as it was immersed in the wet gel.

By making use of the CO_2 phase diagram (Figure 4.5) it is possible to illustrate the difference between the two pathways to dry wet gels. The pathway (a) indicated by the arrow in Figure 4.5 represents the conventional drying process (such as evaporation) by crossing the liquid-gas boundary, which is characterized by the conversion of liquid into gas at defined rate while the amount of liquid is reduced. Consequently, upon solvent removal, the surface tension of the liquid in the gel pores will suffer a capillary pressure gradient in the pore walls reaching pressures nearly 1000 bar, able to collapse the pores.[104] Therefore, in order to avoid the phase boundary transition, the pathway (b) indicated by the curved arrow in Figure 4.5 can be used instead, by submitting the solvent or fluid to supercritical conditions. Supercritical CO_2 drying leads to the presence of supercritical fluid mixtures in the gel pores without residues of any liquid phase. This drying procedure prevents the presence of any intermediate vapor–liquid transition and zero surface tensions in the gel pores when the temperature and pressure are above the supercritical point[‡‡‡] as shown in Figure. 4.5, thus preventing the gel structure from the pore collapse during solvent elimination. The dashed lines in Fig. 4.5 represent the transition in a phase diagram at which the

---

[‡‡‡] Above the supercritical point there is no distinction between gas and liquid or phase boundary. The densities of the liquid phase and vapour phase become equal.

substance is indistinguishable between liquid and its gaseous states.[105]

Supercritical fluids that have been used are: Freons, acetone, nitrous oxide and CO_2. Table 4.1 exhibits the critical point temperatures and pressures for some common fluids. Usually CO_2 is used as fluid, because it has a very low critical temperature of 31°C, low toxicity, it is non-flammable, chemically inert under the employed conditions and some organic solvents like acetone, ethanol and methanol (which were used throughout the experiments) are completely soluble in CO_2. Acetone, ethanol, methanol and water require high temperatures which could modify the structure of the metal oxide material. Although N_2O possesses similar properties as CO_2, according to literature it is considered a strong oxidizer when it is in the supercritical state. The use of Freons was restricted due to the lack of information regarding its solubility for alcohols and acetone, because these solvents are the most common for the solvent exchange process. The set up to prepare aerogel materials is comprised of a stainless steel chamber or autoclave including inlet and outlet valves and one pressure manometer coupled to a liquid CO_2 bottle line. More details can be found elsewhere.[106]
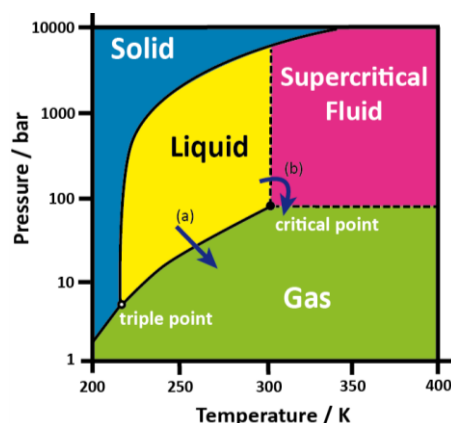
Figure 4.5 Carbon dioxide pressure temperature phase diagram showing the triple point and critical point of CO_2, respectively (5.18 bar, 216.55 K and 73.8 bar, 304.15 K).

Table 4.1 Critical point parameters of common fluids

Fluid	T_c [°C]	P_c (bar)
Freon 116 $(CF_3)_2$	20	29.7
Carbon dioxide (CO_2)	31	73.8
Acetone $(CH_3)_2O$	235	46.6
Nitrous oxide (N_2O)	37	72.4
Ethanol (C_2H_5OH)	243	63
Methanol (CH_3OH)	240	80.9
Water (H_2O)	374	220.4

4.5. Multicomponent aerogels loaded with chemically synthesized metallic particles and multilayer reduced graphene oxide results and discussion

Usually aerogel preparation is reported using amorphous precursors followed by further calcination to obtain the desired crystalline phase.[5, 101a, 101b, 107] In the current work, as shown in the

flowchart (Figure 4.6), it is possible to produce gels with preformed nanocrystalline TiO_2 by simply mixing with additives and subsequent co-gelating without further calcination. Temperature sensitive carbonaceous materials such as m-rGO and the mesoporous structure are preserved in this way (Fig. 4.7).

The aerogel formation process is based on the anisotropic growth of TiO_2 nanocrystals into branched wires, however to achieve this the nanocrystals must be functionalized with an amino compound (trizma, $NH_2C(CH_2OH)_3$). Subsequently the powder can be dispersed in a water/dimethylformamide (DMF) mixture and heated up for a couple of minutes to 90°C to induce the selective replacement of the amino compound until the gelation takes place, in this case pure titania gel is obtained. Hence, the TiO_2 gel is solvent exchanged by increasing increments amounts of acetone in water (e.g. 20/80, 40/60, 60/40, 80/20 and 100 vol. % of acetone). Subsequently, the resulting solvent-exchanged wet gel is then placed in an autoclave which is filled with acetone and submitted to supercritical drying, the result is the aerogel represented by Fig. 4.1a and 4.2.

As indicated by the flowchart in Fig. 4.6, metallic particles can also be introduced in the aerogel preparation process in order to obtain a multicomponent aerogel. In this way, two methods were used to produce metallic particles (Pt, Rh, Au and Ir): (i) a chemical route and (ii) a physical method (laser ablation synthesis in solution – LASIS).[108] The procedure to incorporate either chemically or laser ablated metal particles in the gel is straightforward, it consists in adding the desired concentration of metal particles (previous measured by ICP and/or thermogravimetry) to the TiO_2 sol, gelation and proceeding with the exchange solvent and supercritical dry steps. For the case of adding reduced graphene oxide (m-rGO) the desired concentration in wt. % is added to the TiO_2 sol before mixing it with water and followed by solvent exchange and supercritical drying, as depicted by Fig. 4.1b and 4.2.
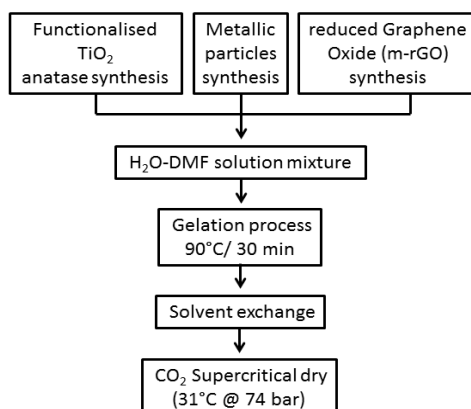
Figure 4.6 Multicomponent aerogel preparation process.

N$_2$ physisorption measurements performed on such aerogels presented high surface areas of about 500 m^2/g with a narrow mesoporous size distribution of the host titania at around 17 nm. The obtained BET surface area indicates that the aerogel architecture doubled the surface area in comparison to trizma-functionalized TiO$_2$ powder (252 m^2/g), while Pt nanoparticles (NPs) and m-rGO loading slightly decrease the surface area (Table 4.2). It was reported previously that the loading of noble metals significantly reduced the pore size distribution.[7, 107] However, in this work the BJH pore size distribution indicates that the loading of Pt NPs or m-rGO sheets does not affect the pore size distribution (Fig. 4.7) confirming the advantage of this method for aerogel preparation.

Table 4.2 Surface areas and pore size of the TiO$_2$ samples

Sample	S$_{BET}$ [m^2 g^{-1}]	D$_p$ [nm]	Band gap [eV][a]
TiO$_2$-trizma	252	-	3.30
TiO$_2$ aerogel (C)	510	18	3.30
Pt/0m-rGO/TiO$_2$ (I)	480	16.5	3.10
Pt/1.0m-rGO/TiO$_2$ (G)	498	17	3.32

S$_{BET}$: Surface area; D$_p$: Pore diameter;
[a] Band gap energies estimated from the Kubelka Munk method (Figure 4.15b).
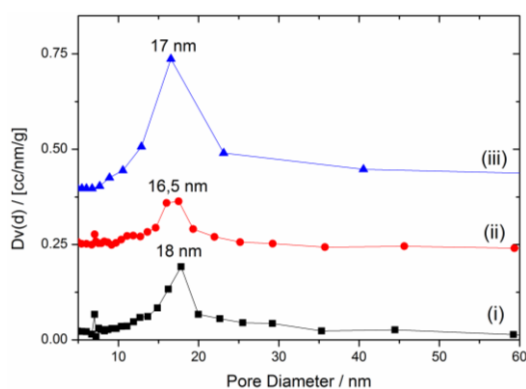
Figure 4.7 Pore size distribution (BJH method) of: (i) TiO$_2$ aerogel, (ii) Pt/0m-rGO/TiO$_2$[§§§] aerogel and (iii) Pt/1.0m-rGO/TiO$_2$ aerogel.

The XRD patterns of the TiO$_2$ trizma functionalized powder and other representative aerogel compositions are shown in Fig. 4.8a. All materials have nearly identical diffraction patterns and were assigned to be in the anatase phase (PDF 21-1272), indicating that the incorporation of Pt particles or carbon materials (m-rGO) does not affect the TiO$_2$ crystallinity. Reflections from platinum or m-rGO were not observed due to the low loading content in the Pt/0m-rGO/TiO$_2$ aerogel and Pt/1.0m-

---

[§§§] The adopted nomenclature for the samples used throughout this chapter: Pt/0m-rGO/TiO$_2$ stands for fixed concentration of Pt (0.4 wt. %), with the desired amount of m-rGO (in this case zero) and the rest of the sample is composed of TiO$_2$. Similarly, for Pt/1.0m-rGO/TiO$_2$, the /1.0m-rGO/ stands for 1 wt. % of m-rGO.

rGO/TiO$_2$ aerogel XRD patterns, respectively. In addition, the reflection peak intensity for m-rGO is 100 times lower in comparison to the TiO$_2$ reflections (Fig. 4.8b). An average crystallite size of 5 nm was determined by using Scherrer's equation fitting the (101) peak for all measured diffraction patterns indicating that the addition of Pt NPs or m-rGO do not affect the TiO$_2$ particle size.
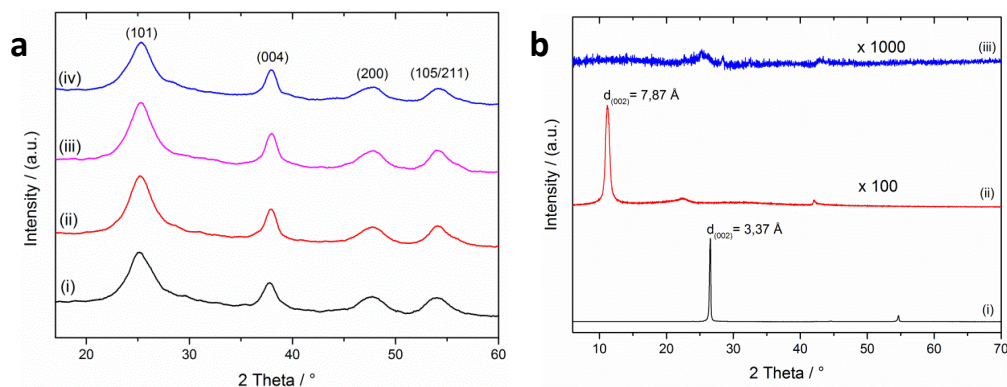
Figure 4.8 (a) XRD diffraction patterns: (i) trizma-functionalized anatase TiO$_2$ powder (ii) TiO$_2$ aerogel (iii) Pt/0m-rGO/TiO$_2$ aerogel (iv) Pt/1.0m-rGO/TiO$_2$ aerogel. (b) XRD patterns: of (i) graphite, (ii) m-graphene oxide, (iii) multilayer reduced graphene oxide (m-rGO). The diffraction pattern in b(ii) was magnified 100x and b(iii) was magnified 1000x.

Transmission electron microscopy (TEM) and high-angle annular dark field (HAADF) images provide information of the Pt/0m-rGO/TiO$_2$ and Pt/1.0m-rGO/TiO$_2$ aerogels samples showing a continuous TiO$_2$ network with multidirectional junctions that lead to the porous structure that is comprised of particle sizes not larger than 3 nm, decorated with quasi-spherical Pt NPs in the range of 1 nm (Figs. 4.9 and 4.10, respectively). Fig. 4.9a shows platinum as black dots dispersed over the TiO$_2$ network while in Fig. 4.9b the HAADF-STEM image reveals the Pt particles as white spots. More details can be observed in the HRTEM image in Fig. 4.9c.

The lattice planes that are visible in the HRTEM images of the TiO$_2$ and Pt particles further confirm their crystalline structure. Due to the contrast in the HAADF-STEM image (Fig. 4.9d) it is possible to distinguish between platinum and TiO$_2$ particles, where the grey and black regions are composed of anatase, whereas the white quasi-spherical particles are composed of platinum with maximum 2 nm in diameter. Although, the aerogel composition changed to Pt/1.0m-rGO/TiO$_2$ by the addition of 1 wt% m-rGO, it is still possible to observe similar structure features as mentioned for the Pt/0m-rGO/TiO$_2$ aerogel as shown in Fig. 4.10. Figures 4.10a and 4.10b show the overview of the Pt/1.0m-rGO/TiO$_2$ images with the characteristic multidirectional network uniformly decorated with Pt NPs. A HRTEM bright field image (Fig. 4.10c) reveals that the particles dimensions are around 3 nm for titanium oxide (light grey) and 1-2 nm for the Pt nanoparticles (dark quasi-spherical regions). In the HAADF (Fig. 4.10d) one can clearly distinguish between the Pt and titanium oxide NPs. TEM measurements were also performed on the single components such as the platinum particles (Figs. 4.11a and 4.11b), m-rGO (Fig.4.12b) and the pure TiO$_2$ aerogel. Using these microscopy techniques it

was possible to ascertain that the synthesized assemblies had the desired configuration, as shown in Figs. 4.9 and 4.10.
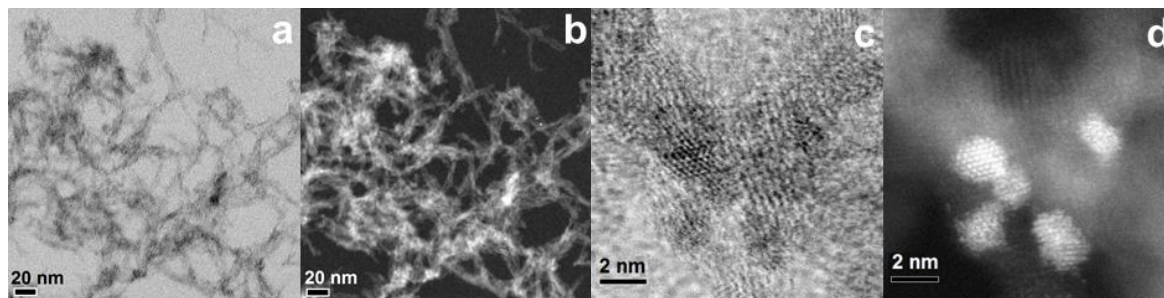
Figure 4.9 (a) Bright field TEM image of Pt/0m-rGO/TiO$_2$ aerogel. (b) HAADF-STEM image of Pt particles on the TiO$_2$ network. (c) HRTEM (d) High-resolution HAADF image of TiO$_2$ network decorated with Pt.

The TEM image of the pure m-rGO showed a carbon sheet within 2-4 microns in diameter without the presence of agglomerates. In contrast to the multilayer morphology displayed by the transmission electron microscopy, the morphology of the multilayer graphene oxide was accessed by preparing a diluted suspension in THF which was drop-casted onto a mica substrate and further analysed through atomic force microscopy (AFM).
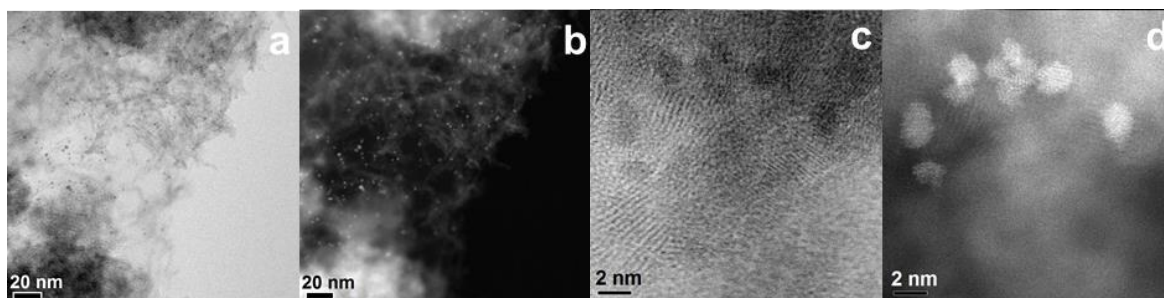
Figure 4.10 (a) Bright field TEM image of for the Pt/1.0m-rGO/TiO$_2$ aerogel. (b) HAADF-STEM image of Pt particles on TiO$_2$ m-rGO network. (c) HRTEM of Pt/1.0m-rGO/TiO$_2$ aerogel and (d) High-resolution HAADF image of TiO$_2$ m-rGO network decorated with Pt (Content: 0.4 wt% Pt and 1 wt% m-rGO).

The result of the AFM analysis is shown in Fig. 4.12 (a, c and d). These images confirm a sheet dimension size at around 2 microns which is in agreement with the transmission electron microscopy presented in Figure 4.12b and also what is expected from the thermal expansion method used to prepare the multilayer graphene oxide.[109] The number of layers was analysed by AFM, because AFM offers more reliable and direct approach to measure the cross section. In addition there is no danger of contamination with solvent or other carbonaceous contaminants that might be adsorbed on the multilayer material produced. Whereas TEM provides the information from the transmitted electrons which results in 2D projections, AFM provides the depth or height of the sample deposited onto the

mica substrate. Fig. 4.12a represents a 2D image including the colour bar in the right indicating the height scale.
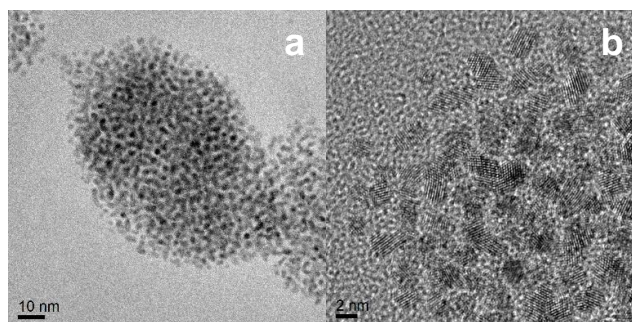
Figure 4.11 HRTEM of the as-synthesized metallic platinum nanoparticles. (a) Platinum nanoparticles overview (b) average platinum particle sizes in the range of 2 nm.
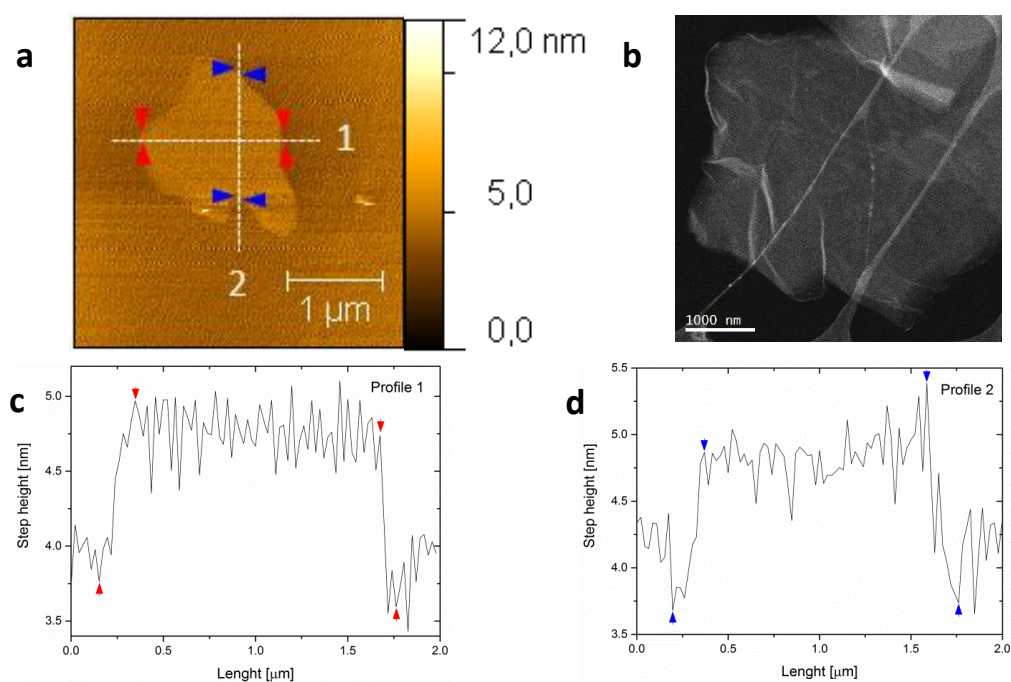
Figure 4.12 (a) AFM image of m-rGO sheet. (b) Transmission electron microscopy (TEM) overview of a (m-rGO) sheet. Depth profile of the horizontal (1) and vertical line (2) from m-rGO sheet in AFM image (a). The red and blue markers correspond to a "three-layer" graphene oxide sheet with a average height of 1.20 nm and 1.24 nm respectively.

Hence, is it possible to measure the depth profile of the sample surface in comparison with the background (mica substrate), in this manner two perpendicular lines were traced and measured and the results are plotted in Fig. 4.12c and 4.12d. A height average of nearly 1.2 nm or "three-layer" (considering the thickness of one single layer ~ 0.35 nm) sheet was determined for both horizontal and vertical lines. Moreover, one must take into account that the graphene sheet thickness is affected by the functional groups such as carbonyls and epoxides which were confirmed by C1s XPS and FTIR analysis (Fig. 4.13) and also errors associated with the AFM measurement. The C1s XPS analysis of thermal exfoliated graphene oxide under a mixture of argon and hydrogen revealed the

presence of 4 main peaks while the analysis of the graphite used as precursor showed 3 main peaks (Fig. 4.13a). Thus, carbon and oxygen amounts of 89.35% and 10.65% respectively were quantified by C1s and O1s XPS of the thermal exfoliated material, meanwhile the graphite precursor revealed carbon and oxygen amounts of 97.77% and 2.23% respectively. The graphite precursor showed 3 main peaks (insert of Fig. 4.13a), namely C–C sp^2 (284.4 eV), extended delocalised electrons denominated satellite peak (π–π*) can lead in higher binding energy nearly at 291 eV and C–O at 285.2 eV. The latter peak may be the result of atmospheric oxidation as reported by Honorita-Lucas et al.,[110] and/or impurities present in the commercial precursor. In the C1s XPS spectra obtained from the thermal exfoliated material (m-rGO) the following peaks could be assigned: C–C sp^2 (284.5 eV), C–O (285.6 eV), C=O (287 eV) and π–π* around 292 eV as observed previously by Ganguly et al.[111] The results are consistent with the amount of oxygen determined by O1s XPS analysis of nearly 10% and in addition, a sharp decrease in hydroxyl, alkoxy, carbonyl and epoxy groups was observed via the FTIR (Fig. 4.13b). However, the presence of carbonyl and epoxy groups are persistent despite of the thermal reduction applied, as a result of the larger particle size m-rGO that can be visualized in lower resolution on the outer surface of the fractures (Fig. 4.14a and 4.14b) in multicomponent aerogels. The high resolution of the lateral section of the m-rGO impregnated with platinum nanoparticles can be clearly distinguished in bright field (Fig. 4.14c) and in the HAADF (Fig. 4.14d). Moreover, the high resolution of the lateral section of the m-rGO shows the multilayer morphology of the synthesized material.
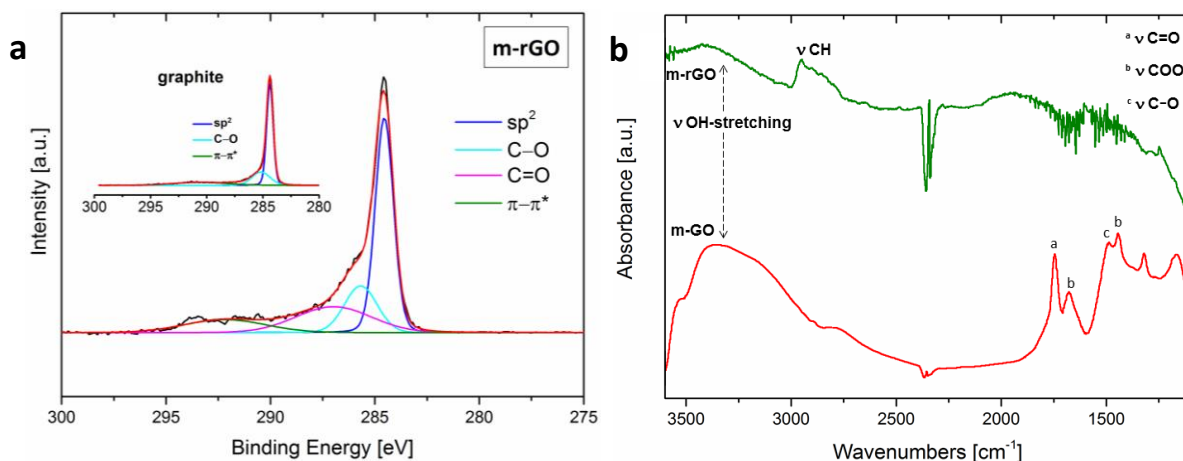
Figure 4.13 (a) C1s XPS spectra of multilayer reduced graphene oxide (m-rGO), including an insert of the C1s of the graphite material used as precursor. The black line represents the measured spectra while the red line represents the fitted curve; the blue, cyan, pink and olive curves represent the assigned functional groups. (b) FTIR of the multilayer graphene oxide (m-GO) before and after thermal reduction (m-rGO).
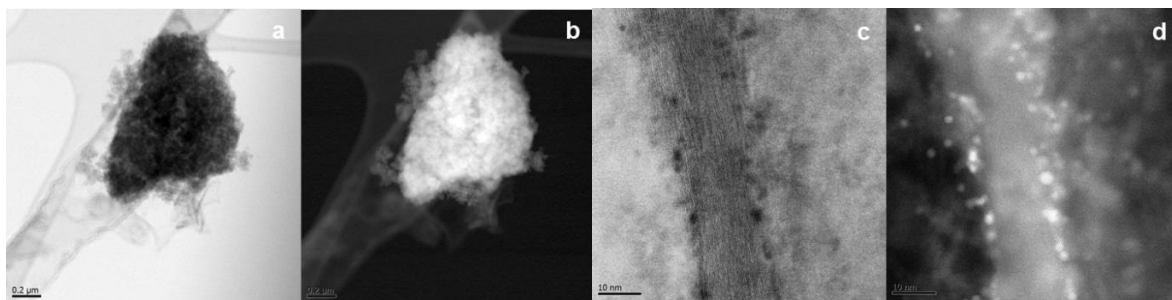
Figure 4.14. (a) TEM bright field image showing an overview of the Pt/5.0m/rGO-TiO$_2$ aerogel, (b) STEM dark field picture for Pt/5.0m-rGO/TiO$_2$ aerogel, (c) HRTEM (d) High-resolution HAADF image of m-rGO stack decorated with Pt nanoparticles surrounded by TiO$_2$ network.

Dynamic light scattering (DLS) investigations were conducted to obtain the size distribution and stability of the aerogel structures when poured into a water/methanol mixture. Figure 4.15a indicates a broad monomodal distribution with a mean size of around 630 nm for the formed pure TiO$_2$ aerogel and nearly 400 nm for Pt/0m-rGO/TiO$_2$ and Pt/1.0m-rGO/TiO$_2$ aerogels, respectively. These results indicate the hydrodynamic aerogel size in liquid media. While the macrostructure of the monolith is lost during the "dissolution" process the microstructure is still preserved by the well-interconnected TiO$_2$ network, shown in Figures 4.9a, b and 4.10a, b.

The UV diffuse reflectance spectroscopy measurements were performed to evaluate the effect of loading aerogel with platinum NP and/or with m-rGO. According to the obtained results shown in Figure 4.15b no significant shift or change in band gap was observed, however the addition of m-rGO induces light absorption intensity loss as compared to the pure TiO$_2$ aerogel.
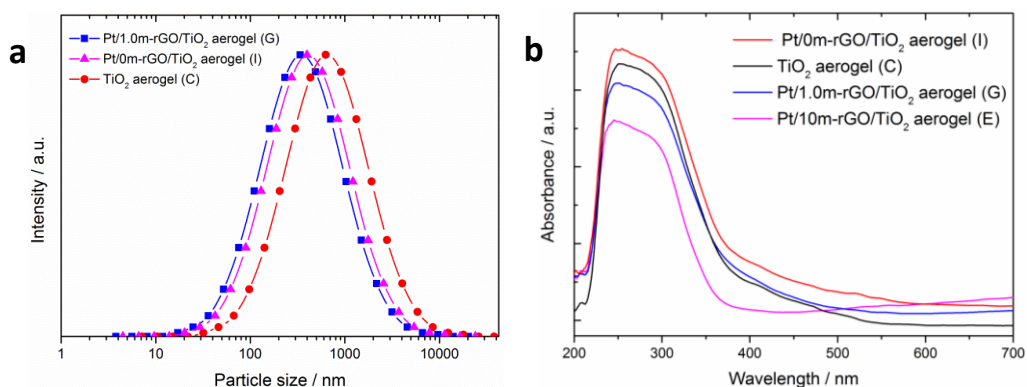
Figure 4.15 (a) Size distribution profiles obtained by dynamic light scattering (DLS) for the following aerogels: (G) 340 ± 14 nm, (I) 400 ± 42 nm and (C) 630 ± 50 nm. (b) Diffuse reflectance absorption spectra of aerogels loaded with platinum and/or m-rGO: (C) TiO$_2$ aerogel, (I) Pt/0m-rGO/TiO$_2$, (G) Pt/1m-rGO/TiO$_2$ and (E) Pt/10m-rGO/TiO$_2$.

Fig. 4.16a shows the photocatalytic H_2 generation of various materials including the pure TiO_2 aerogel (C)[****], and the samples "mixture Pt/0m-rGO/TiO_2" (A) and "mixture Pt/10m-rGO/TiO_2" (B) used as references for comparison. TiO_2 aerogel alone (C) showed only poor photocatalytic activity due to rapid recombination of photogenerated charge carriers. However, if additives are introduced such as the co-catalyst or the co-catalyst together with m-rGO higher photocatalytic activities are observed in comparison with the reference samples (A and B) in Fig. 4.16a. A significantly improved photocatalytic hydrogen generation was achieved when applying the aerogel containing material (I) (Pt/0m-rGO/TiO_2) with showed a light-to-hydrogen conversion efficiency of approx. 0.9%.[112] With the latter sample a 3.5-fold increase of activity was obtained compared to the reference powder (A), and even a 67-fold improvement compared to the TiO_2 aerogel (C) (Fig.4.16b). This comparison shows, that the activity increase is largely due to the aerogel architecture and not only to the crystal structure or from simply mixing the single components. The aerogel prevents particles from aggregation and induces a better distribution of the additives. The influence of the co-catalyst was investigated by increasing the platinum loading to 1.0 wt% and by reducing its loading to 0.1 wt%. The photocatalytic curves are shown in Figure 4.16c. The photocatalytic results suggested that the 0.4 wt% platinum is the optimum loading for the specified conditions.

The activity of sample (D) is slightly enhanced compared to sample (C) (see table 4.3) because the electrical conductive m-rGO acts by conducting electrons as previously reported.[1] Furthermore, a detailed study of the influence of m-rGO loading on the multicomponent aerogel has been performed (Fig. 4.16d) at an optimum Pt loading of 0.4 wt% (Fig. 4.16b). Depending on the m-rGO concentration different photocatalytic H_2 generation activities were observed and a clear trend could not be identified due to the relative high experimental error of nearly 15%. However the sample (I), which contains no m-rGO showed an almost 2-fold increase in activity. This fact is not consistent with previous reports from ourselves,[1] Kim et al.,[113] and Yeh et al..[114] All aforementioned groups' observed the increase of H_2 production after addition of reduced graphene oxide. The apparent drop in photocatalytic H_2 generation between samples (I and G) can be explained as follows. The photoactivity decrease of the aerogels loaded with m-rGO can be explained due to the physical separation between the TiO_2 catalyst and the m-rGO sheets when suspended in aqueous solution. As illustrated in Fig.4.1b the multicomponent aerogel was conceived to enable good contact and dispersion between the co-catalysts and m-rGO over the entire TiO_2 matrix. However, the addition of the multicomponent aerogel in aqueous solution may contribute to the physical segregation between the inorganic titania matrix and the m-rGO sheets. Hence, the DLS results in Fig. 4.15a indicated a hydrodynamic aerogel size in aqueous solution in the range of 400-600 nm for several

---

[****] Each tested composition was given a capital letter label in order to easily identify them. All labelling details and compositions are shown in table 4.3.

aerogel compositions, which has a relative large size to provide a good contact between the m-rGO and all the TiO_2 particles of the branched network. In this way, most of the charge carries will recombine within the TiO_2 branched network preventing the electrons to reach the m-rGO sheets. Additionally, the higher affinity of the metal nanoparticles to the m-rGO in comparison to TiO_2 should be stressed, because the samples loaded with m-rGO and Pt particles resulted in a significant concentration of metallic NPs adsorbed in the m-rGO to the detriment of low amount into the TiO_2, as illustrated in Fig. 4.14c/d. As a consequence the co-catalyst loading over the TiO_2 semiconductor was decreased reducing in this way the photocatalytic activity.
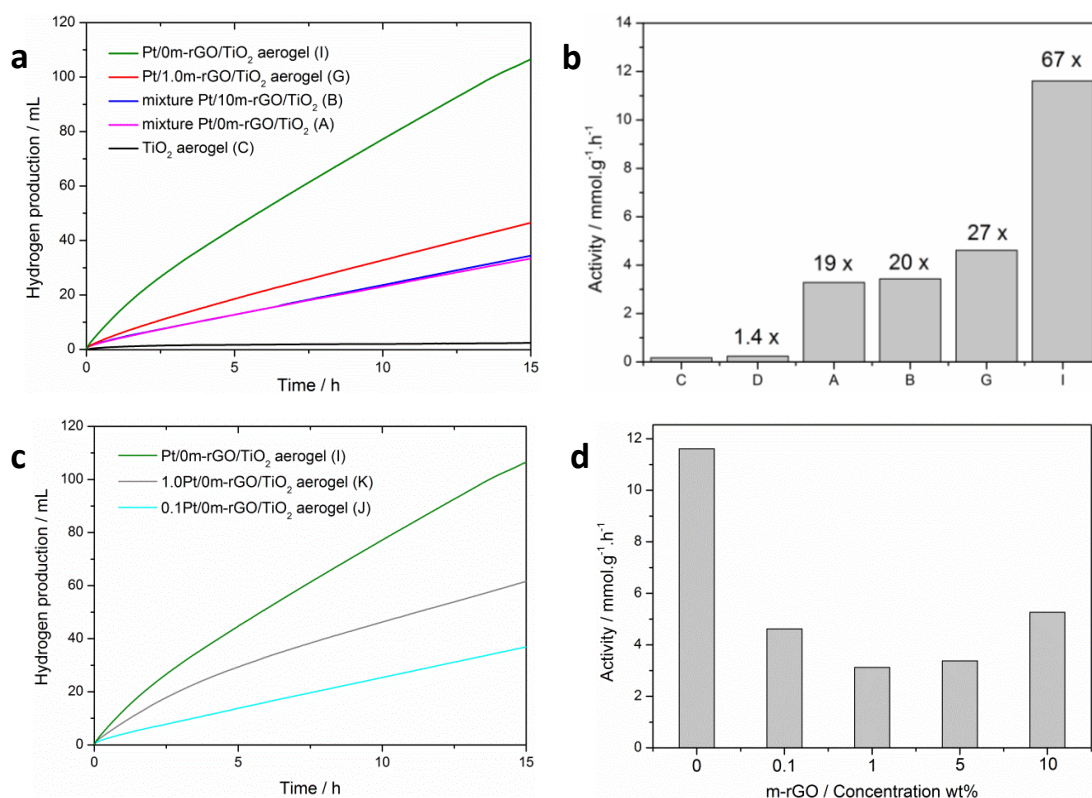
Figure 4.16 Photocatalytic production of hydrogen in aqueous suspension (a) Effect of the aerogel architecture and composition on the respective hydrogen evolution curves. (b) Comparison of the hydrogen evolution rates, expressed in mmol of H_2 produced per gram of catalyst and hour, of the different aerogels compositions and powder mixtures. (c) Influence of the Pt NPs content (wt. %) on the photocalytic production of hydrogen in aqueous suspension. Pt sample content: (I): 0.4 wt. %, (J): 1.0 wt. %, (K): 0.01 wt. %; (d) Influence of the m-rGO concentration on the photocatalytic activities, depicted as mmol H_2 g^{-1} h^{-1}.[††††]

[††††] Experimental conditions for all catalytic tests: 25 mg catalysts, 10 mL MeOH / H_2O (1/1), Lumatec Hg-light source (Lumatec Superlite 400) equipped with a 320-500 nm filter, 7.2 W output, 25°C. Further details are given in Table 2.

Table 4.3 Summary of the photocatalytic activities and the evolved amount of hydrogen for the different aerogels and TiO$_2$ mechanical mixtures

entry	composition [a] %	n_{H2} / h [µmol h^{-1}]	activity [µmol H$_2$ g^{-1} h^{-1}]
A	mixture Pt/0m-rGO/TiO$_2$ [b]	82.1	3283
B	mixture Pt/10m-rGO/TiO$_2$ [b]	85.7	3430
C	TiO$_2$ aerogel [c]	4.3	172
D	1.0m-rGO/TiO$_2$ aerogel [d]	6.0	239
E	Pt/10m-rGO/TiO$_2$ aerogel	131.4	5257
F	Pt/5.0m-rGO/TiO$_2$ aerogel	84.3	3374
G	Pt/1.0m-rGO/TiO$_2$ aerogel	101.3	4051
H	Pt/0.1m-rGO/TiO$_2$ aerogel	115.3	4614
I	Pt/0m-rGO/TiO$_2$ aerogel	290.2	11609
J	0.1Pt/TiO$_2$ aerogel	82	3267
K	1.0Pt/TiO$_2$ aerogel	173.4	6935

[a] The Pt content of 0.4 wt.% is kept constant for all samples. Except for samples C and D that do not present any platinum content and samples J and K that present 0.01 and 1.0 wt.% respectively.
[b] Powder mixture for comparison; [c] represents the blank value of the system; [d] control experiment without metal loading. Given values are the averages of at least two independent measurements with typical differences in between 5 and 21%.

4.6 Aerogel loaded with metallic particles produced by laser ablation synthesis in solution (LASIS): Results and discussion

Since the highest performance was obtained on a m-rGO free aerogel, the influence of noble metal NPs co-loading was investigated. This sub-chapter describes the characterization of the metallic particles produced by laser ablation (Rh, Pt, Ir and Au) that were incorporated into the TiO$_2$

gelation process as described in section 4.5. The TiO$_2$ gels loaded with a very low amount of metallic colloids (0.01 wt. % measured by ICP) produced by LASIS were submitted to the supercritical drying procedure to obtain aerogels and their activity in the photocatalytic hydrogen production were tested.

For LASIS the metallic target or powder is placed in a Beaker or conical bottom flask filled with solvent (maximum height of 1 cm above the target surface) and submitted to laser ablation process during 1 to 5 minutes depending on the target and the desired concentration. The ablated particles are suspended in solution as shown in Fig. 4.17a and Fig. 4.17b. The usage of a conical bottom flask is indicated to keep metallic powders under the focus of the laser beam, which facilitates the ablation process. The choice of solvent is related to its compatibility with the gelation process (solvents such as water, acetone or ethanol are preferred because they are compatible with the TiO$_2$-water suspension), although solvents with very low polarity such as chloroform can keep the nanoparticles stable in solution for months. Fig. 4.17c shows the colloids generated from the ablation process in solution using water as solvent after three cycles of 1 to 5 minutes of laser irradiation time. The laser cycles are done to avoid superheating and fast evaporation of the solvents.
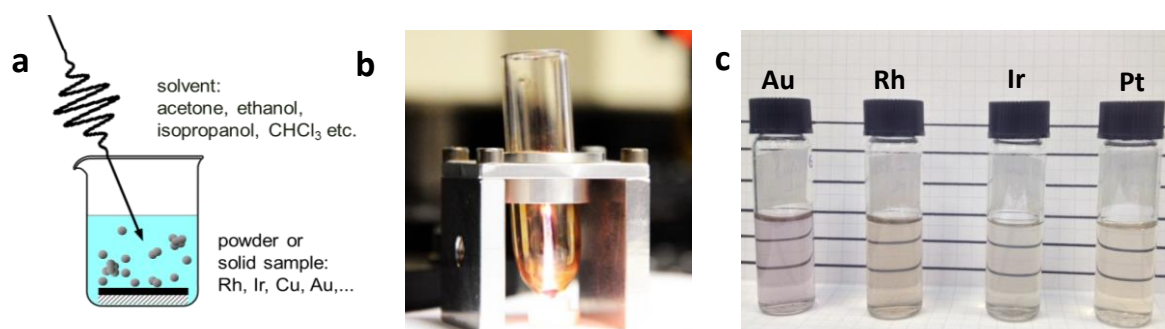
Figure 4.17 (a) Illustration of how a metallic target (plate or powder) is laser ablated in solution, (b) conical flask used for supporting metallic powder filled with solution. After some seconds of ablation is possible to observe particle scattering (Tyndall effect), (c) Metal colloidal solutions produced after 3 minutes laser irradiation with metal content in the range of 0.020 mgmL^{-1} measured by ICP (from left to right: Au, Rh, Ir and Pt).

AFM and TEM analysis were performed on the colloids obtained by LASIS and the results are discussed below. After optimization of the laser parameters such as wavelength, repetition rate, pulse, focus and laser power output, the sizes/concentration ratio of the nanoparticles was maximized   (i.e. to produce the smallest sizes at a reasonable concentration in a few minutes of ablation). The metallic colloid solutions obtained were individually analysed by atomic force microscopy (AFM) by dropping the colloid onto a Si (100) substrate followed by mild evaporation. The advantage of using AFM lies in the fact that it is possible to scan 1 cm^2 of the substrate area that is covered with metal particles in a few minutes. Hence, the multiple images generated can be analysed with digital software to elaborate a size histogram with at least 500 particles counts, in

order to make reliable statistics with the obtained histogram. The images employing transmission electron microscopy were used to exhibit the morphology of the particles obtained by the laser ablation process. It is appropriate to mention that the apparent deviation observed between the particle size distributions using TEM and AFM is consistent in all cases. One feature must be noted regarding the particle agglomerates that cannot be distinguished from the single large particles, as a result the supposed large particles or agglomerates were not counted.

AFM images of Au NP obtained by laser ablation are depicted in Fig. 4.18a. The particle size histogram (Fig. 4.18b) shows a bimodal distribution with maxima at 5.7 and 7.3 nm respectively after counting 856 gold nanoparticles. Additionally, the TEM results on the same sample corroborate the AFM data in terms of morphology. The TEM image in Fig. 4.19a indicates the predominance of small particles over a very few large particles while in the Fig. 4.19b one can observe in high resolution one single Au particle with a size in the range of 20 nm.
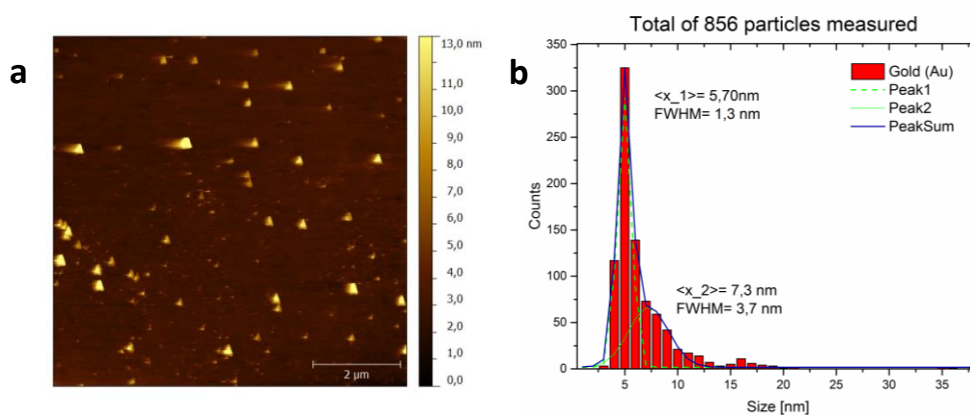
Figure 4.18 (a) AFM image of the gold particles deposited over a silicon substrate, (b) histogram of the gold particles measured by AFM.
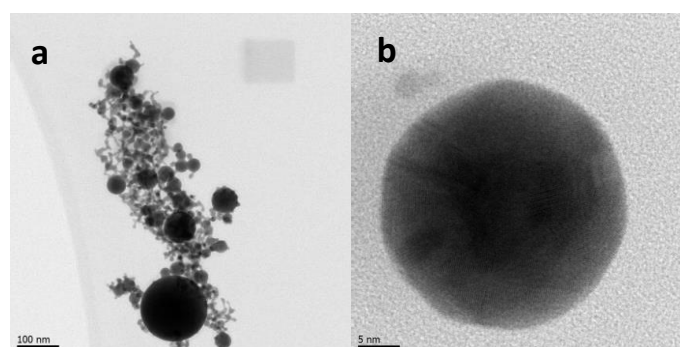
Figure 4.19 (a) TEM overview and (b) HRTEM of the obtained gold particles.

AFM and TEM analysis were performed on the metallic colloids obtained by LASIS and they apparently exhibited different sizes, because with AFM it was not possible to resolve in between one large particle or a large agglomerate of small particles. However, a bimodal distribution was observed

for all the metallic colloids samples. The iridium NP also show a bimodal distribution with maxima at 5.5 and 6.0 nm after 723 particles counts. TEM analysis also shows the predominance of small sizes over large particle sizes. Additionally, using low magnification and high-resolution the TEM image displayed only spherical particles as shown in Figs. 4.20 and 4.21.
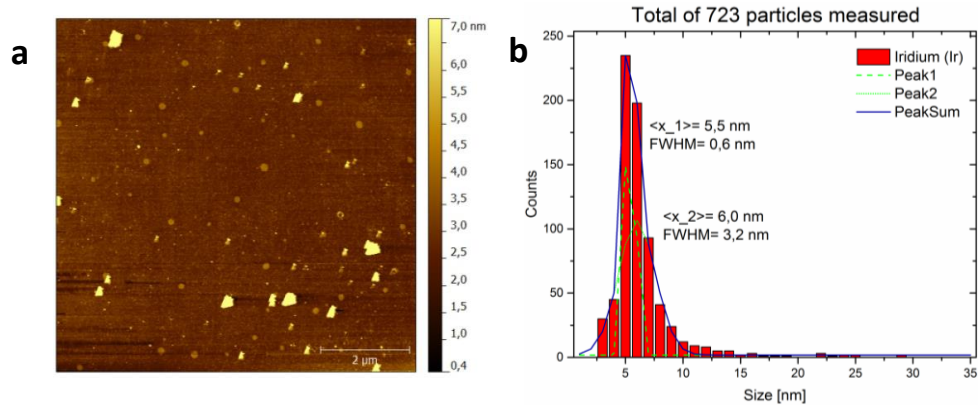
Figure 4.20 (a) AFM image of the Iridium particles deposited over a silicon substrate, (b) histogram of the iridium particles measured by AFM.
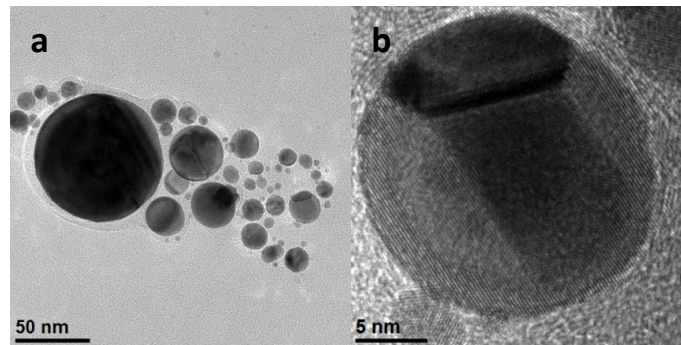
Figure 4.21 (a) TEM overview and (b) HRTEM of the obtained Iridium particles.
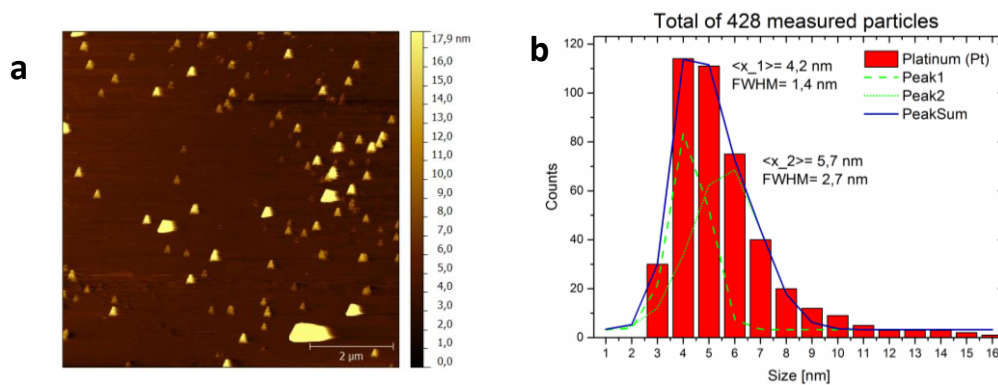
Figure 4.22 (a) AFM image of the Platinum particles deposited over a silicon substrate, (b) histogram of the Platinum particles measured by AFM.

The platinum NP showed a bimodal distribution with maxima at 4.2 and 5.7 nm respectively after 428 particle counts as revealed by the AFM analysis (Fig. 4.22) and the TEM analysis showed spherical particles in the range from 2-20 nm (Fig. 4.23). AFM analysis of the rhodium NP showed a

very dense particle population and also a bimodal size distribution with maxima at 4.6 and 7.4 nm respectively (Fig. 4.24). TEM analysis one the same sample showed typical spherical particles in the range of 3-20nm.
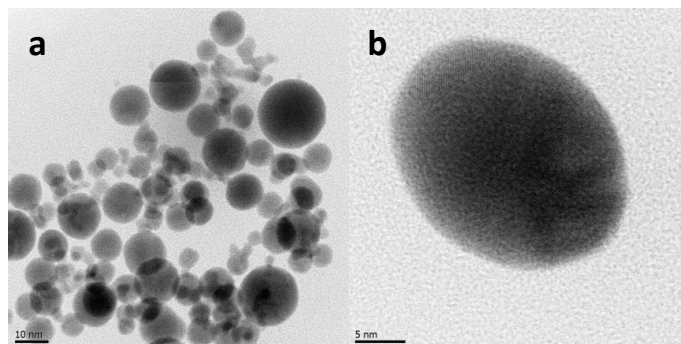
Figure 4.23 (a) TEM overview and (b) HRTEM of the obtained Platinum particles.
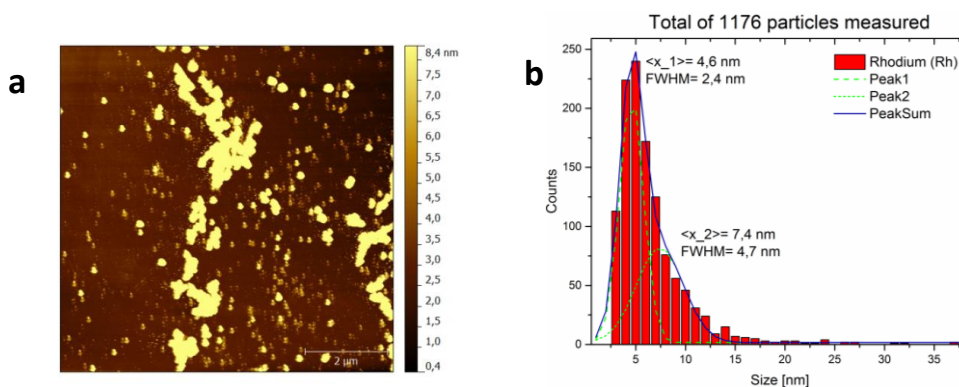
Figure 4.24 (a) AFM image of the Rhodium particles deposited over a silicon substrate, (b) histogram of the Rhodium particles measured by AFM.
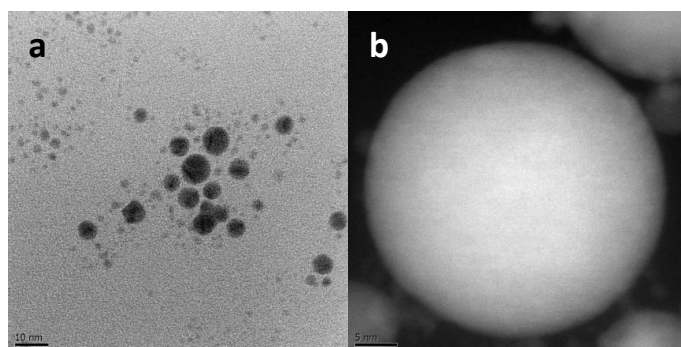
Figure 4.25 (a) TEM overview and (b) HRTEM of the obtained Rhodium particles.

After the characterization of the individual metallic colloids, the aerogel incorporating the metallic species was also analysed by TEM to investigate the structural features. Only the TiO_2 aerogels with rhodium and platinum were analysed. The TiO_2 aerogel loaded with 0.01% rhodium nanoparticles is depicted in Fig. 4.26a. It is clear that the low amount of metal loaded did not change

the aerogel structure, moreover the HRTEM also confirmed the unaltered aerogel structure (Fig. 4.26b). The aerogel loaded with platinum showed the same morphology and structure as observed with low and high magnification (Figs. 4.27a and 4.27b). In spite of the very low amount of platinum used it was possible to identify one platinum particle by atomic contrast in figure 4.27c as indicated by the green arrow.
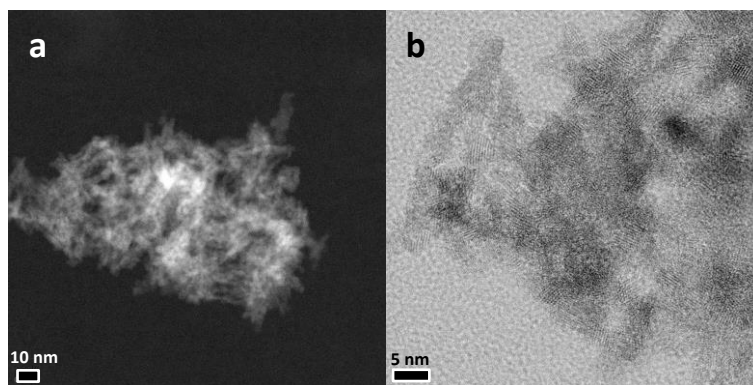
Figure 4.26 (a) TEM overview and (b) HRTEM of the obtained TiO$_2$ aerogel loaded with 0.01% Rh particles.
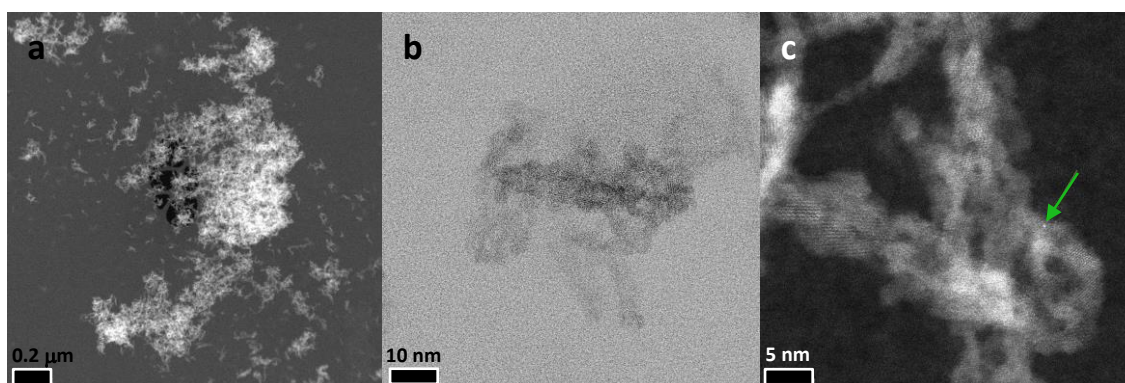
Figure 4.27 (a) TEM overview and (b) HRTEM of the obtained TiO$_2$ aerogel loaded with 0.01% Pt particles, (c) mesoporous structure of the TiO$_2$ aerogel and identification of a single Platinum particle.

Although the observation of one single metal NP into the aerogel structure does not provide enough evidence of the low metallic amount (Fig. 4.27c), more evidence for the presence of the metal NP (0.01 wt. %) in the aerogel was obtained by its photocatalytic activity for hydrogen evolution under UV-vis irradiation using methanol as hole scavenger. In the Fig. 4.28 the green curve shows the HER from the control sample (pristine TiO$_2$ aerogel) while the other curves are assigned to one specific metal loading. The yield of hydrogen was observed to decrease in the order Rh > Ir > Au > Pt > pure TiO$_2$. These experiments clearly show the enhancement effect at the presence of very low amounts (0.01 wt. %) of metallic particles in comparison with bare TiO$_2$ aerogel. The light-to-hydrogen

conversion (η %) for the best photocatalyst (TiO$_2$-Rh aerogel) is approx. 0.08% based on volumetric density for hydrogen at 1 bar.[112]
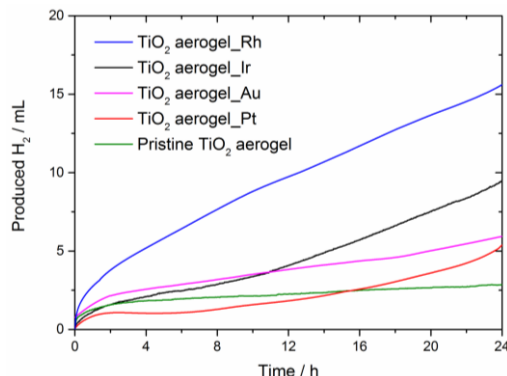
Figure 4.28. Photocatalytic production of hydrogen in aqueous suspension using laser ablated metal particles loaded in TiO$_2$ aerogel. All samples contain 0.01 wt. % of metal particles with exception of the control sample (pristine TiO$_2$ aerogel).

All experiments were performed at least twice to confirm the amount of hydrogen collected and also to determine the experimental error which was between 10 and 15%. The metal loading of the aerogel was chosen to be 0.01 wt. % to take advantage of the as-generated low concentration metal colloids. Additionally, LASIS is able to produce colloids with small sizes and clean surfaces, which is suitable to be used as co-catalysts (e.g. since there is no surfactants or capping agents to interfere or block the reduction catalytic sites).

4.7 Conclusions

A multicomponent photocatalyst was prepared by the assembly of preformed titania, chemically synthesized platinum NP and multilayer reduced graphene oxide. Another approach explored the production of noble metal colloids in water or organic solvents through physical method e.g. LASIS and their incorporation into preformed TiO$_2$ gel using H$_2$O/DMF dispersion followed by gelation and CO$_2$ supercritical drying. The solid and crystalline pure TiO$_2$ aerogel possesses a high surface area with a narrow pore size distribution, around 500 m^{2}g^{-1} and 17 nm, respectively. The addition of either platinum NP (0.01 – 1.0 wt %) or other noble metals (i.e. Rh, Ir and Au) or m-rGO in loading levels up to 10 wt % does not influence the mesoporous aerogel architecture. The best multicomponent catalyst loaded with chemically synthesized platinum NP showed a hydrogen production rate of 290.2 µmol H$_2$ h^{-1} with efficiency close to 1% while the aerogels with very low metal content produced by LASIS showed an inferior hydrogen gas production reaching 29.6 µmol H$_2$ h^{-1} with an efficiency of nearly to 0.10%. However, the metal concentration analysis for the aerogels incorporated with laser ablated NP showed that a reduction in 40 times the amount of metal resulted in a decrease of only 10-15 times on their activity. Moreover a significant

photoactivity loss was observed for the multicomponent aerogel loaded with multilayer reduced graphene oxide (m-rGO) due to physical separation between the TiO_2 network catalyst and the m-rGO sheets while suspended in aqueous solution. Including, a slightly enrichment of Pt NPs deposited on the m-rGO sheets at the cost of a lower loading of the Pt nanoparticles on the TiO_2, resulted in a less effective co-catalyst loading over the TiO_2 semiconductor.

By combining different materials we demonstrated that it is possible to build a more complex aerogel besides enhancing the hydrogen evolution photoactivity. In this way, this work provides the motivation for implementing other multicompenent aerogels compositions applied to the photocatalysis area.

4.8 Experimental Section

4.8.1 Synthesis and materials

Multicomponent aerogels were prepared by the following materials and techniques, which are summarized in scheme 1. In details: (i) chemical synthesis of trizma-functionalized TiO_2 anatase. (ii) synthesis of metallic nanoparticles free of surface ligands or stabilizers. (iii) m-rGO was prepared applying Hummer's method and subsequently reduced by a solvothermal treatment or thermal expansion. (iv) mixing the previously prepared materials to prepare one single dispersion. (v) gelation of the mixed dispersion. (vi) solvent exchange and supercritical drying of the samples.

Aerogel derived catalysts are abbreviated according to the following nomenclature: Pt/Xm-rGO/TiO_2 with: 0.4 wt% Pt and X: wt% m-rGO, both related to the overall mass in the TiO_2 aerogel network (for details, see table 2). Reference catalysts are denoted as mixture *Pt/X*m-rGO/TiO_2.

Chemicals: Titanium (IV) chloride (>99.0%), benzyl alcohol (≥99.0%) and chloroform (≥99.8%) were purchased from Merck. 2-Amino-2-(hydroxymethyl)-1,3-propanediol (trizma ≥99.7%) and graphite powder (< 20 µm) were purchased from Sigma-Aldrich. N,N-Dimethylformamide (DMF 99.8%) and tetrahydrofuran (THF 99.9%) were purchased from Acros. Ethanol (≥99.5%), sulfuric acid (H_2SO_4 96%) and potassium permanganate (KMnO4 ≥99.%) were purchased from Carl Roth. Chloroplatinic acid was isolated after treatment in aqua regia using pure platinum metal >99.99% as precursor. All gases used during the experiments were purchased from Linde and/or Air Liquide. Only deionized water (DI) was used throughout the experiments. All chemicals were used as received.

4.8.1.1 (i) Synthesis of trizma-functionalized TiO_2

The synthesis was adapted from a published synthesis protocol.[8] 6.49 mmol (786 mg) 2-amino-2-(hydroxymethyl)-1,3-propanediol (trizma), was dissolved in 170 ml of benzyl alcohol by heating to 80 °C for 30 min. After cooling to room temperature 77.52 mmol (8.5 ml) of $TiCl_4$ was added drop wise under stirring. The reaction solution was heated to 80°C for 24 h. Afterwards, the solution was

cooled to room temperature and the resulting particles were separated from the solvent by centrifugation. The yellowish supernatant was decanted; the white precipitate was washed with chloroform by re-dispersing the precipitate. The washing step was repeated at least three times with chloroform followed by centrifugation. The wet precipitate was dried in the oven under vacuum (60°C, 12 h), ground and finally redispersed in water. The final concentration of trizma functionalized anatase nanoparticles was 120 mg/ml.

4.8.1.2 (iia) Synthesis of the platinum nanoparticles:

179 mg H_2PtCl_6 were dissolved in 60 ml DMF and stirred for 15 minutes at room temperature. Aliquots of 30 ml were poured into 50 ml Teflon vessels, sealed and heated in a CEM Mars laboratory microwave for 30 s at 220°C with a maximum power of 600 W. The resulting nanoparticle dispersion was used without further treatment. The final solution concentration of 0.94 mg/mL was determined using induced coupled plasma atomic emission spectroscopy (ICP).

4.8.1.3 (iib) Laser ablation synthesis in solution (Rh, Ir, Au and Pt) in water:

Metallic targets with maximum 1 mm thickness and 1 cm^2 area were placed into a Beaker flask with 200 mL volume and covered with deionised water to approx. 1 cm above the target and placed under the laser beam. The laser ablation parameters used for the targets were the following: 343 nm wavelength and 50 W average laser power with 400 kHz repetition rate with scan speed of 1000 mm s^{-1}. Ablation times of 5 minutes were used for all metal targets. After the ablation process, the coloured colloids were transferred to glass vials and analysed by ICP and gravimetric measurements to determine the metal content. The ICP and gravimetric values for the laser ablated metal targets were in the range of 0.015-0.025 mg mL^{-1}.

4.8.1.4 (iii) Synthesis of multilayer reduced graphene oxide (m-rGO)

Graphite powder was exfoliated and oxidized using a modified Hummer's method.[115] In detail, 5.0 g graphite and 2.5 g $NaNO_3$ were added to 120 mL concentrated H_2SO_4 and the mixture was cooled to 0°C. $KMnO_4$ (15.0 g) was added slowly under stirring in order to keep the reaction below 30°C. Afterwards, the slurry was stirred at 35°C for 0.5 h and then 230 mL water were added slowly in order to keep the reaction temperature around 98°C for 15 minutes. The suspension was quenched by adding 700 mL of water and the remaining unreacted $KMnO_4$ was consumed by adding 12 mL of H_2O_2 (30%). After cooling to room temperature the black slurry was purified as follows. The filtrate was centrifuged (4000 rpm for 1 h) and its supernatant decanted and discarded. The remaining solid was washed extensively with water (1.5 L), two times with HCl (30%) solution (200 mL each) and with ethanol and with acetone afterwards (200 mL each). For every washing cycle centrifugation was used

to collect the precipitate (4000 rpm / 15 minutes) except for the washing with ethanol and acetone (10000 rpm / 0.5 h). The brown solid precipitate that was obtained was dried overnight at 40°C. For the reduction step, 1.0 g of the dried GO was dispersed into 100 mL of 99.5% ethanol and sonicated for 0.5 h prior to pouring the solution into a Teflon autoclave after which it was submitted to a to solvothermal treatment at 150°C for 24 hours.

Thermal expansion of graphene oxide was also used during the experiments according to a previous published protocol.[109] The thermal expansion and exfoliation consist of heating up the as prepared graphene oxide at 1050°C under argon and hydrogen flow for at least 30 seconds until the carbonaceous material is violently expanded inside the quartz tube.

4.8.1.5 (iv) Pre-mixing of nanoparticle dispersions for aerogel preparation

For the preparation of a mixture of Pt and TiO_2 nanoparticles, the aqueous TiO_2 anatase dispersion is mixed with the platinum dispersion in DMF in a volumetric ratio of 2 to 1. For dispersions containing m-rGO, the proportional amount of m-rGO powder is dispersed in the as synthesized platinum colloid dispersion and sonicated for 30 minutes. Then, the TiO_2 dispersion is added in a volume ratio of 2 to 1. For the preparation of dispersions without platinum, pure DMF is used instead.

4.8.1.6 (v) Preparation of particles mixture (*Pt/X*m-rGO/TiO$_2$)

As a control experiment, the photocatalyst was also prepared without supercritical drying and the same procedure was performed as described above (item iv). The as prepared mixed dispersions were stirred and afterwards sonicated for 10 minutes and dried in vacuum overnight at 60°C. A fine powder was obtained after grinding the dry product.

4.8.1.7 (vi) Gelation of the nanoparticle dispersions (*Pt/X*m-rGO/TiO$_2$)

After pouring the dispersions in a Teflon container, the container is sealed and the gelation is induced by heating the containers to 90 °C for 30 min in an oven. The final gels can be removed from the container after cooling to room temperature.

4.8.1.8 (vii) Supercritical drying

The DMF-water pore liquid of the TiO_2 gels is stepwise exchanged to acetone, by increments amounts of acetone in water (e.g. 20/80, 40/60, 60/40, 80/20 and 100 vol. % of acetone). Subsequently, the resulting solvent-exchanged wet gel is then placed in an autoclave which is filled with acetone and submitted to supercritical drying. The CO_2 supercritical drying was performed with a Leica CPD 030 or Emitech K850. The gels obtained can be stored in acetone or can be immediately

transferred in the CO_2 supercritical dry equipment chamber. At first the chamber was pre-cooled to 5°C and purged with CO_2. Then the sample was left to soak in CO_2 for 30 minutes and after this period the gas was released and another purging step was repeated (in general this procedure was performed 3x or until checking with filter paper at outlet of exhaust of the equipment for damp patch indicating solvent exchange conditions). After the solvent exchange was completed the heating was turned on until the temperature reached 40°C and the pressure in the chamber rose to nearly 80 bar. Normally the supercritical drying conditions are achieved around 31°C and 74 bar.

4.8.2 Characterization

Powder X-ray diffraction (XRD) was carried out on a STADI P automated transmission diffractometer from STOE (Darmstadt, Germany) with an incident beam curved germanium monochromator selecting Cu K-alpha radiation (I = 1.5406 Å, 40 kV, 40 mA) and a 6° linear position sensitive detector (PSD). The alignment was checked by use of a silicon standard. The data were collected in the 2 Theta range from 5 – 60 ° with a step size of 0.5 ° and a measurement time of 50 seconds per step.

Brunauer-Emmett-Teller (BET) surface area and Barrett-Joyner-Halenda (BJH) pore size distribution were determined on a Quantachrome Nova 4200 or Quantachrome autosorb IQ instruments with nitrogen as the sorption gas.

Transmission electron microscopy (TEM) measurements were performed at 200 kV on a JEM-ARM200F instrument (JEOL, Japan), aberration-corrected by a CESCOR (CEOS) for STEM applications. The samples were prepared by adding the solid ground aerogels directly on a holey carbon-supported grid (mesh 300) and transferred to the instrument. The measurements for Fig. 4.11 performed on a Philips Tecnai F30 operated at 300 kV. For sample preparation the platinum nanoparticles in DMF were dropped as synthesised on a carbon coated copper grid on a filter paper to absorb excess liquid and dried at 60 °C.

For the AFM characterization, the THF dispersion of the m-rGO was dripped onto a fresh cleaved mica substrate. The measurement was performed using Nanosurf Easyscan 2 equipment. The characterization of the metal particles was performed using AFM XE-100 from Parksystems in non-contact mode. The generated metal colloid solution was dropped on a Si (100) substrate.

Dynamic Light scattering (DLS) measurements were performed with a Malvern Instrument Zetasizer 3000HSA equipped with a He-Ne laser (λ = 633 nm, max 5 mW) and operated at a scattering angle of 90°. In all measurements, 1 mL of particle suspensions was employed and placed in a 10 mm × 10 mm quartz cuvette at 25°C. Samples were prepared in the same way as prepared for the photocatalysis experiments.

Uv-vis spectroscopy (UV-vis) spectra were recorded with an AvaSpec 2048 fiber optical spectrometer (Avantes B.V., Netherlands) equipped with an AvaLight-DHS light source and a FCR-7UV200-2-45-ME 45° reflection probe using barium sulfate as reference.

Inductively coupled plasma optical emission spectrometry (ICP-OES) using a Varian 715-ES ICP- emission spectrometer was carried out, in order to quantify the amount of platinum in the aerogel samples. C, H, N, and S analysis was performed by using a TruSpec CHNS Micro analyser (Leco) to quantify the amount of carbon and hydrogen in the m-GO and m-rGO samples.

4.8.3 Laser ablation experiment

The metal targets (Rh, Ir, Au and Pt) were ablated by an industrial picosecond laser (TRUMPF TruMicro 5x50) with 6 ps pulses at 343 nm and average laser power of 50 W, with pulse energies up to 125 µJ and repetition rate of 400 kHz and scan speed of 1000 mm s^{-1}.

4.8.4 Photocatalytic measurements

All catalytic experiments were carried out under argon atmosphere with freshly distilled solvents. In a standard reaction a double-walled and thermostatically controlled (25°C) reaction vessel was connected to an automatic gas burette and several times flushed with argon. Then, the solid catalyst sample (25 mg) was introduced in a Teflon crucible, followed by the addition of methanol and water (10 ml MeOH/H$_2$O in the volume ratio of 1/1). The photocatalytic reaction was started by irradiating the stirred (300 rpm) reaction mixture with light (Hg-light source, Lumatec Superlite 400, equipped with a 320-500 nm filter, 7.2 W output). The gas evolution was quantitatively measured by means of an automatic gas burette, while the gas composition was further analyzed by GC (HP 6890N, carboxen 1000, TCD detector). Further details on the equipment and experimental setup have been published previously.[116]

4.9 References

1.   Meyer, T.; Priebe, J. B.; da Silva, R. O.; Peppel, T.; Junge, H.; Beller, M.; Brueckner, A.; Wohlrab, S., Advanced Charge Utilization from NaTaO$_3$ Photocatalysts by Multilayer Reduced Graphene Oxide. *Chem. Mat.* **2014,** *26* (16), 4705-4711.
2.   DeSario, P. A.; Pietron, J. J.; DeVantier, D. E.; Brintlinger, T. H.; Stroud, R. M.; Rolison, D. R., Plasmonic enhancement of visible-light water splitting with Au-TiO$_2$ composite aerogels. *Nanoscale* **2013,** *5* (17), 8073-8083.
3.   Pierre, A. C.; Pajonk, G. M., Chemistry of aerogels and their applications. *Chem. Rev.* **2002,** *102* (11), 4243-4265.
4.   Gesser, H. D.; Goswami, P. C., Aerogels and Related Porous Materials. *Chem. Rev.* **1989,** *89* (4), 765-788.
5.   Pajonk, G. M., Aerogel Catalysts. *Appl Catal* **1991,** *72* (2), 217-266.
6.   Pajonk, G. M., Catalytic aerogels. *Catal. Today* **1997,** *35* (3), 319-337.
7.   Pietron, J. J.; Stroud, R. M.; Rolison, D. R., Using three dimensions in catalytic mesoporous nanoarchitectures. *Nano Lett* **2002,** *2* (5), 545-549.

8.   Heiligtag, F. J.; Rossell, M. D.; Suess, M. J.; Niederberger, M., Template-free co-assembly of preformed Au and TiO_2 nanoparticles into multicomponent 3D aerogels. *J. Mater. Chem.* **2011,** *21* (42), 16893-16899.

9.   da Silva, R. O.; Heiligtag, F. J.; Karnahl, M.; Junge, H.; Niederberger, M.; Wohlrab, S., Design of multicomponent aerogels and their performance in photocatalytic hydrogen production. *Catal. Today* **2015,** *246*, 101-107.

10.   Hoffmann, M. R.; Martin, S. T.; Choi, W. Y.; Bahnemann, D. W., Environmental applications of semiconductor photocatalysis *Chem. Rev.* **1995,** *95* (1), 69-96.

11.   Diebold, U., The surface science of titanium dioxide. *Surf. Sci. Rep.* **2003,** *48* (5-8), 53-229.

12.   Ni, M.; Leung, M. K. H.; Leung, D. Y. C.; Sumathy, K., A review and recent developments in photocatalytic water-splitting using TiO_2 for hydrogen production. *Renewable & Sustainable Energy Reviews* **2007,** *11* (3), 401-425.

13.   Chen, X.; Mao, S. S., Titanium dioxide nanomaterials: Synthesis, properties, modifications, and applications. *Chem. Rev.* **2007,** *107* (7), 2891-2959.

14.   Fujishima, A.; Zhang, X. T.; Tryk, D. A., TiO_2 photocatalysis and related surface phenomena. *Surf. Sci. Rep.* **2008,** *63* (12), 515-582.

15.   Zhang, H. Z.; Banfield, J. F., Understanding polymorphic phase transformation behavior during growth of nanocrystalline aggregates: Insights from TiO_2. *Journal of Physical Chemistry B* **2000,** *104* (15), 3481-3487.

16.   Fresno, F.; Portela, R.; Suarez, S.; Coronado, J. M., Photocatalytic materials: recent achievements and near future trends. *Journal of Materials Chemistry A* **2014,** *2* (9), 2863-2884.

17.   Kasuga, T.; Hiramatsu, M.; Hoson, A.; Sekino, T.; Niihara, K., Formation of titanium oxide nanotube. *Langmuir* **1998,** *14* (12), 3160-3163.

18.   Trentler, T. J.; Denler, T. E.; Bertone, J. F.; Agrawal, A.; Colvin, V. L., Synthesis of TiO_2 nanocrystals by nonhydrolytic solution-based reactions. *J. Am. Chem. Soc.* **1999,** *121* (7), 1613-1614.

19.   Alberius, P. C. A.; Frindell, K. L.; Hayward, R. C.; Kramer, E. J.; Stucky, G. D.; Chmelka, B. F., General predictive syntheses of cubic, hexagonal, and lamellar silica and titania mesostructured thin films. *Chem. Mat.* **2002,** *14* (8), 3284-3294.

20.   Jiang, X. C.; Herricks, T.; Xia, Y. N., Monodispersed spherical colloids of titania: Synthesis, characterization, and crystallization. *Adv. Mater.* **2003,** *15* (14), 1205-+.

21.   Armstrong, A. R.; Armstrong, G.; Canales, J.; Bruce, P. G., TiO_2-B nanowires. *Angew. Chem.-Int. Edit.* **2004,** *43* (17), 2286-2288.

22.   Yuan, Z. Y.; Su, B. L., Titanium oxide nanotubes, nanofibers and nanowires. *Colloids and Surfaces a-Physicochemical and Engineering Aspects* **2004,** *241* (1-3), 173-183.

23.   Feng, X.; Shankar, K.; Varghese, O. K.; Paulose, M.; Latempa, T. J.; Grimes, C. A., Vertically Aligned Single Crystal TiO_2 Nanowire Arrays Grown Directly on Transparent Conducting Oxide Coated Glass: Synthesis Details and Applications. *Nano Lett* **2008,** *8* (11), 3781-3786.

24.   Livage, J.; Henry, M.; Sanchez, C., Sol-Gel chemistry of transition metal oxides. *Prog. Solid State Chem.* **1988,** *18* (4), 259-341.

25.   Vioux, A., Nonhydrolytic sol-gel routes to oxides. *Chem. Mat.* **1997,** *9* (11), 2292-2299.

26.   Yoo, K. S.; Choi, H.; Dionysiou, D. D., Synthesis of anatase nanostructured TiO_2 particles at low temperature using ionic liquid for photocatalysis. *Catalysis Communications* **2005,** *6* (4), 259-262.

27.   Ritala, M.; Leskela, M.; Nykanen, E.; Soininen, P.; Niinisto, L., Growth of titanium dioxide thin films by atomic layer epitaxy. *Thin Solid Films* **1993,** *225* (1-2), 288-295.

28.   Natarajan, C.; Nogami, G., Cathodic electrodeposition of nanocrystalline titanium dioxide thin films. *J. Electrochem. Soc.* **1996,** *143* (5), 1547-1550.

29.   Yu, J. C.; Yu, J. G.; Ho, W. K.; Zhang, L. Z., Preparation of highly photocatalytic active nano-sized TiO_2 particles via ultrasonic irradiation. *Chem. Commun.* **2001,** (19), 1942-1943.

30.   Yamamoto, T.; Wada, Y.; Yin, H. B.; Sakata, T.; Mori, H.; Yanagida, S., Microwave-driven polyol method for preparation of TiO_2 nanocrystallites. *Chemistry Letters* **2002,** (10), 964-965.

31.   Mutin, P. H.; Vioux, A., Nonhydrolytic Processing of Oxide-Based Materials: Simple Routes to Control Homogeneity, Morphology, and Nanostructure. *Chem. Mat.* **2009,** *21* (4), 582-596.

32.   Niederberger, M.; Garnweitner, G., Organic reaction pathways in the nonaqueous synthesis of metal oxide nanoparticles. *Chem.-Eur. J.* **2006,** *12* (28), 7282-7302.

33.   Ranade, M. R.; Navrotsky, A.; Zhang, H. Z.; Banfield, J. F.; Elder, S. H.; Zaban, A.; Borse, P. H.; Kulkarni, S. K.; Doran, G. S.; Whitfield, H. J., Energetics of nanocrystalline TiO_2. *Proc. Natl. Acad. Sci. U. S. A.* **2002,** *99*, 6476-6481.

34.   Fox, M. A.; Dulay, M. T., Heterogeneous Photocatalysis *Chem. Rev.* **1993,** *93* (1), 341-357.

35.   Oregan, B.; Gratzel, M., A low-cost, high-efficiency solar cell based on dye-sensitized colloidal TiO_2 films. *Nature* **1991,** *353* (6346), 737-740.

36.   Bamwenda, G. R.; Tsubota, S.; Nakamura, T.; Haruta, M., Photoassisted hydrogen production from a water-ethanol solution: a comparison of activities of Au-TiO$_2$ and Pt-TiO$_2$. *Journal of Photochemistry and Photobiology a-Chemistry* **1995,** *89* (2), 177-189.

37.   Tseng, I. H.; Chang, W. C.; Wu, J. C. S., Photoreduction of CO2 using sol-gel derived titania and titania-supported copper catalysts. *Applied Catalysis B-Environmental* **2002,** *37* (1), 37-48.

38.   Liu, S. X.; Qu, Z. P.; Han, X. W.; Sun, C. L., A mechanism for enhanced photocatalytic activity of silver-loaded titanium dioxide. *Catal. Today* **2004,** *93-5*, 877-884.

39.   Wu, N. L.; Lee, M. S., Enhanced TiO2 photocatalysis by Cu in hydrogen production from aqueous methanol solution. *Int. J. Hydrog. Energy* **2004,** *29* (15), 1601-1605.

40.   Sakthivel, S.; Shankar, M. V.; Palanichamy, M.; Arabindoo, B.; Bahnemann, D. W.; Murugesan, V., Enhancement of photocatalytic activity by metal deposition: characterisation and photonic efficiency of Pt, Au and Pd deposited on TiO$_2$ catalyst. *Water Res.* **2004,** *38* (13), 3001-3008.

41.   Golabiewska, A.; Lisowski, W.; Jarek, M.; Nowaczyk, G.; Zielinska-Jurek, A.; Zaleska, A., Visible light photoactivity of TiO$_2$ loaded with monometallic (Au or Pt) and bimetallic (Au/Pt) nanoparticles. *Applied Surface Science* **2014,** *317*, 1131-1142.

42.   Su, R.; Tiruvalam, R.; Logsdail, A. J.; He, Q.; Downing, C. A.; Jensen, M. T.; Dimitratos, N.; Kesavan, L.; Wells, P. P.; Bechstein, R.; Jensen, H. H.; Wendt, S.; Catlow, C. R. A.; Kiely, C. J.; Hutchings, G. J.; Besenbacher, F., Designer Titania-Supported Au-Pd Nanoparticles for Efficient Photocatalytic Hydrogen Production. *ACS Nano* **2014,** *8* (4), 3490-3497.

43.   Sugano, Y.; Shiraishi, Y.; Tsukamoto, D.; Ichikawa, S.; Tanaka, S.; Hirai, T., Supported Au–Cu Bimetallic Alloy Nanoparticles: An Aerobic Oxidation Catalyst with Regenerable Activity by Visible-Light Irradiation. *Angewandte Chemie International Edition* **2013,** *52* (20), 5295-5299.

44.   Shiraishi, Y.; Sakamoto, H.; Sugano, Y.; Ichikawa, S.; Hirai, T., Pt–Cu Bimetallic Alloy Nanoparticles Supported on Anatase TiO$_2$: Highly Active Catalysts for Aerobic Oxidation Driven by Visible Light. *ACS Nano* **2013,** *7* (10), 9287-9297.

45.   Lee, S. G.; Lee, S.; Lee, H. I., Photocatalytic production of hydrogen from aqueous solution containing CN$^-$ as a hole scavenger. *Applied Catalysis a-General* **2001,** *207* (1-2), 173-181.

46.   Kida, T.; Guan, G. Q.; Yamada, N.; Ma, T. L.; Kimura, K.; Yoshida, A., Hydrogen production from sewage sludge solubilized in hot-compressed water using photocatalyst under light irradiation. *Int. J. Hydrog. Energy* **2004,** *29* (3), 269-274.

47.   Gimbert-Surinach, C.; Albero, J.; Stoll, T.; Fortage, J.; Collomb, M. N.; Deronzier, A.; Palomares, E.; Llobet, A., Efficient and Limiting Reactions in Aqueous Light-Induced Hydrogen Evolution Systems using Molecular Catalysts and Quantum Dots. *J. Am. Chem. Soc.* **2014,** *136* (21), 7655-7661.

48.   Kawai, T.; Sakata, T., Photocatalytic hydrogen production from liquid methanol and water *J. Chem. Soc.-Chem. Commun.* **1980,** (15), 694-695.

49.   Chen, J.; Ollis, D. F.; Rulkens, W. H.; Bruning, H., Photocatalyzed oxidation of alcohols and organochlorides in the presence of native TiO$_2$ and metallized TiO$_2$ suspensions. Part (I): Photocatalytic activity and pH influence. *Water Res.* **1999,** *33* (3), 661-668.

50.   Chen, J.; Ollis, D. F.; Rulkens, W. H.; Bruning, H., Photocatalyzed oxidation of alcohols and organochlorides in the presence of native TiO$_2$ and metallized TiO$_2$ suspensions. Part (II): Photocatalytic mechanisms. *Water Res.* **1999,** *33* (3), 669-676.

51.   Wang, C. Y.; Rabani, J.; Bahnemann, D. W.; Dohrmann, J. K., Photonic efficiency and quantum yield of formaldehyde formation from methanol in the presence of various TiO$_2$ photocatalysts. *Journal of Photochemistry and Photobiology a-Chemistry* **2002,** *148* (1-3), 169-176.

52.   Guo, Q.; Xu, C. B.; Ren, Z. F.; Yang, W. S.; Ma, Z. B.; Dai, D. X.; Fan, H. J.; Minton, T. K.; Yang, X. M., Stepwise Photocatalytic Dissociation of Methanol and Water on TiO$_2$(110). *J. Am. Chem. Soc.* **2012,** *134* (32), 13366-13373.

53.   Xu, C.; Yang, W.; Guo, Q.; Dai, D.; Chen, M.; Yang, X., Molecular Hydrogen Formation from Photocatalysis of Methanol on TiO$_2$(110). *J. Am. Chem. Soc.* **2013,** *135* (28), 10206-10209.

54.   Yang, H. G.; Sun, C. H.; Qiao, S. Z.; Zou, J.; Liu, G.; Smith, S. C.; Cheng, H. M.; Lu, G. Q., Anatase TiO$_2$ single crystals with a large percentage of reactive facets. *Nature* **2008,** *453* (7195), 638-U4.

55.   (a) Lazzeri, M.; Vittadini, A.; Selloni, A., Structure and energetics of stoichiometric TiO2 anatase surfaces. *Physical Review B* **2001,** *63* (15); (b) Lazzeri, M.; Vittadini, A.; Selloni, A., Structure and energetics of stoichiometric TiO2 anatase surfaces (vol 63, art no 155409, 2001). *Physical Review B* **2002,** *65* (11).

56.   Han, X.; Kuang, Q.; Jin, M.; Xie, Z.; Zheng, L., Synthesis of Titania Nanosheets with a High Percentage of Exposed (001) Facets and Related Photocatalytic Properties. *J. Am. Chem. Soc.* **2009,** *131* (9), 3152-3153.

57.   Gurunathan, K.; Maruthamuthu, P.; Sastri, M. V. C., Photocatalytic hydrogen production by dye-sensitized Pt/SnO$_2$ and Pt/SnO$_2$/RuO$_2$ in aqueous methyl viologen solution. *Int. J. Hydrog. Energy* **1997,** *22* (1), 57-62.

58.   Dhanalakshmi, K. B.; Latha, S.; Anandan, S.; Maruthamuthu, P., Dye sensitized hydrogen evolution from water. *Int. J. Hydrog. Energy* **2001,** *26* (7), 669-674.

59.   Polo, A. S.; Itokazu, M. K.; Iha, N. Y. M., Metal complex sensitizers in dye-sensitized solar cells. *Coord. Chem. Rev.* **2004,** *248* (13-14), 1343-1361.

60.   Youngblood, W. J.; Lee, S. H. A.; Kobayashi, Y.; Hernandez-Pagan, E. A.; Hoertz, P. G.; Moore, T. A.; Moore, A. L.; Gust, D.; Mallouk, T. E., Photoassisted Overall Water Splitting in a Visible Light-Absorbing Dye-Sensitized Photoelectrochemical Cell. *J. Am. Chem. Soc.* **2009,** *131* (3), 926-+.

61.   Jarosz, P.; Du, P.; Schneider, J.; Lee, S.-H.; McCamant, D.; Eisenberg, R., Platinum(II) Terpyridyl Acetylide Complexes on Platinized TiO$_2$: Toward the Photogeneration of H$_2$ in Aqueous Media. *Inorganic Chemistry* **2009,** *48* (20), 9653-9663.

62.   Kim, W.; Tachikawa, T.; Majima, T.; Li, C.; Kim, H.-J.; Choi, W., Tin-porphyrin sensitized TiO$_2$ for the production of H$_2$ under visible light. *Energy Environ. Sci.* **2010,** *3* (11), 1789-1795.

63.   Takanabe, K.; Kamata, K.; Wang, X.; Antonietti, M.; Kubota, J.; Domen, K., Photocatalytic hydrogen evolution on dye-sensitized mesoporous carbon nitride photocatalyst with magnesium phthalocyanine. *Phys. Chem. Chem. Phys.* **2010,** *12* (40), 13020-13025.

64.   Libanori, R.; da Silva, R. O.; Ribeiro, C.; Ari-Gur, P.; Leite, E. R., Improved Photocatalytic Activity of Anisotropic Rutile/Anatase TiO$_2$ Nanoparticles Synthesized by the Ti-Peroxo Complex Method. *Journal of Nanoscience and Nanotechnology* **2012,** *12* (6), 4678-4684.

65.   Zhang, X.; Jin, Z.; Li, Y.; Li, S.; Lu, G., Efficient Photocatalytic Hydrogen Evolution from Water without an Electron Mediator over Pt–Rose Bengal Catalysts. *The Journal of Physical Chemistry C* **2009,** *113* (6), 2630-2635.

66.   Abe, R.; Shinmei, K.; Hara, K.; Ohtani, B., Robust dye-sensitized overall water splitting system with two-step photoexcitation of coumarin dyes and metal oxide semiconductors. *Chem. Commun.* **2009,** (24), 3577-3579.

67.   Hirano, K.; Suzuki, E.; Ishikawa, A.; Moroi, T.; Shiroishi, H.; Kaneko, M., Sensitization of TiO$_2$ particles by dyes to achieve H$_2$ evolution by visible light. *Journal of Photochemistry and Photobiology a-Chemistry* **2000,** *136* (3), 157-161.

68.   Ikeda, S.; Abe, C.; Torimoto, T.; Ohtani, B., Photochemical hydrogen evolution from aqueous triethanolamine solutions sensitized by binaphthol-modified titanium(IV) oxide under visible-light irradiation. *Journal of Photochemistry and Photobiology a-Chemistry* **2003,** *160* (1-2), 61-67.

69.   Zhang, X. H.; Veikko, U.; Mao, J.; Cai, P.; Peng, T. Y., Visible-Light-Induced Photocatalytic Hydrogen Production over Binuclear RuII-Bipyridyl Dye-Sensitized TiO$_2$ without Noble Metal Loading. *Chem.-Eur. J.* **2012,** *18* (38), 12103-12111.

70.   Choi, W. Y.; Termin, A.; Hoffmann, M. R., The role of metal ion dopants in quantum sized TiO$_2$ - Correlation between photoreactivity and charge carrier recombination dynamics. *J Phys Chem-Us* **1994,** *98* (51), 13669-13679.

71.   Asahi, R.; Morikawa, T.; Ohwaki, T.; Aoki, K.; Taga, Y., Visible-Light Photocatalysis in Nitrogen-Doped Titanium Oxides. *Science* **2001,** *293* (5528), 269-271.

72.   Khan, S. U. M.; Al-Shahry, M.; Ingler, W. B., Efficient photochemical water splitting by a chemically modified n-TiO$_2$. *Science* **2002,** *297* (5590), 2243-2245.

73.   Chen, X. B.; Liu, L.; Yu, P. Y.; Mao, S. S., Increasing Solar Absorption for Photocatalysis with Black Hydrogenated Titanium Dioxide Nanocrystals. *Science* **2011,** *331* (6018), 746-750.

74.   Hoang, S.; Berglund, S. P.; Hahn, N. T.; Bard, A. J.; Mullins, C. B., Enhancing Visible Light Photo-oxidation of Water with TiO$_2$ Nanowire Arrays via Cotreatment with H$_2$ and NH$_3$: Synergistic Effects between Ti^{3+} and N. *J. Am. Chem. Soc.* **2012,** *134* (8), 3659-3662.

75.   Zheng, Z.; Huang, B.; Lu, J.; Wang, Z.; Qin, X.; Zhang, X.; Dai, Y.; Whangbo, M.-H., Hydrogenated titania: synergy of surface modification and morphology improvement for enhanced photocatalytic activity. *Chem. Commun.* **2012,** *48* (46), 5733-5735.

76.   Wang, G.; Wang, H.; Ling, Y.; Tang, Y.; Yang, X.; Fitzmorris, R. C.; Wang, C.; Zhang, J. Z.; Li, Y., Hydrogen-Treated TiO$_2$ Nanowire Arrays for Photoelectrochemical Water Splitting. *Nano Lett* **2011,** *11* (7), 3026-3033.

77.   Zhang, Z.; Hedhili, M. N.; Zhu, H.; Wang, P., Electrochemical reduction induced self-doping of Ti^{3+} for efficient water splitting performance on TiO$_2$ based photoelectrodes. *Phys. Chem. Chem. Phys.* **2013,** *15* (37), 15637-15644.

78.   (a) Kistler, S. S., Coherent Expanded-Aerogels. *The Journal of Physical Chemistry* **1931,** *36* (1), 52-64; (b) Kistler, S. S., Coherent Expanded Aerogels and Jellies. *Nature* **1931,** *127*, 741.

79.		Schmidt, M.; Schwertfeger, F., Applications for silica aerogel products. *J Non-Cryst Solids* **1998,** *225* (1), 364-368.

80.		Fricke, J.; Tillotson, T., Aerogels: Production, characterization, and applications. *Thin Solid Films* **1997,** *297* (1-2), 212-223.

81.		Mohanan, J. L.; Arachchige, I. U.; Brock, S. L., Porous semiconductor chalcogenide aerogels. *Science* **2005,** *307* (5708), 397-400.

82.		Leventis, N.; Rawashdeh, A.-M. M.; Elder, I. A.; Yang, J.; Dass, A.; Sotiriou-Leventis, C., Synthesis and Characterization of Ru(II) Tris(1,10-phenanthroline)-Electron Acceptor Dyads Incorporating the 4-Benzoyl-N-methylpyridinium Cation or N-Benzyl-N'-methyl Viologen. Improving the Dynamic Range, Sensitivity, and Response Time of Sol–Gel-Based Optical Oxygen Sensors. *Chem. Mat.* **2004,** *16* (8), 1493-1506.

83.		Hrubesh, L. W.; Pekala, R. W., Thermal properties of organic and inorganic aerogels. *J. Mater. Res.* **1994,** *9* (3), 731-738.

84.		Schwertfeger, F.; Glaubitt, W.; Schubert, U., Hydrophobic aerogels from $Si(OMe)_4$/$MeSi(OMe)_3$ mixtures. *J Non-Cryst Solids* **1992,** *145* (1-3), 85-89.

85.		Jin, H.; Kettunen, M.; Laiho, A.; Pynnonen, H.; Paltakari, J.; Marmur, A.; Ikkala, O.; Ras, R. H. A., Superhydrophobic and Superoleophobic Nanocellulose Aerogel Membranes as Bioinspired Cargo Carriers on Water and Oil. *Langmuir* **2011,** *27* (5), 1930-1934.

86.		Tsou, P., Silica aerogel captures cosmic dust intact. *J Non-Cryst Solids* **1995,** *186*, 415-427.

87.		Sumiyoshi, T.; Adachi, I.; Enomoto, R.; Iijima, T.; Suda, R.; Yokoyama, M.; Yokogawa, H., Silica aerogels in high energy physics. *J Non-Cryst Solids* **1998,** *225* (1), 369-374.

88.		da Cunha, J. P.; Neves, P.; Lopes, M. I., On the reconstruction of Cherenkov rings from aerogel radiators. *Nuclear Instruments & Methods in Physics Research Section a-Accelerators Spectrometers Detectors and Associated Equipment* **2000,** *452* (3), 401-421.

89.		Coles, M. P.; Lugmair, C. G.; Terry, K. W.; Tilley, T. D., Titania-silica materials from the molecular precursor Ti OSi((OBu)-Bu-t)(3) (4): Selective epoxidation catalysts. *Chem. Mat.* **2000,** *12* (1), 122-131.

90.		Fabrizioli, P.; Burgi, T.; Baiker, A., Environmental catalysis on iron oxide-silica aerogels: Selective oxidation of NH3 and reduction of NO by NH_3. *J Catal* **2002,** *206* (1), 143-154.

91.		Rolison, D. R., Catalytic nanoarchitectures - The importance of nothing and the unimportance of periodicity. *Science* **2003,** *299* (5613), 1698-1701.

92.		Wang, J.; Uma, S.; Klabunde, K. J., Visible light photocatalysis in transition metal incorporated titania-silica aerogels. *Applied Catalysis B-Environmental* **2004,** *48* (2), 151-154.

93.		Moreno-Castilla, C.; Maldonado-Hodar, F. J., Carbon aerogels for catalysis applications: An overview. *Carbon* **2005,** *43* (3), 455-465.

94.		Fricke, J., Aerogels: Highly tenuous solids with fascinating properties. *J Non-Cryst Solids* **1988,** *100* (1-3), 169-173.

95.		(a) Pekala, R. W., Organic aerogels from the polycondensation of resorcinol with formaldehyde. *Journal of Materials Science* **1989,** *24* (9), 3221-3227; (b) Pekala, R. W.; Alviso, C. T.; Kong, F. M.; Hulsey, S. S., Aerogels derived from multifunctional organic monomers. *J Non-Cryst Solids* **1992,** *145* (1-3), 90-98.

96.		(a) Jin, H.; Nishiyama, Y.; Wada, M.; Kuga, S., Nanofibrillar cellulose aerogels. *Colloids and Surfaces a-Physicochemical and Engineering Aspects* **2004,** *240* (1-3), 63-67; (b) Cai, J.; Kimura, S.; Wada, M.; Kuga, S.; Zhang, L., Cellulose aerogels from aqueous alkali hydroxide-urea solution. *Chemsuschem* **2008,** *1* (1-2), 149-154; (c) Olsson, R. T.; Samir, M. A. S. A.; Salazar-Alvarez, G.; Belova, L.; Strom, V.; Berglund, L. A.; Ikkala, O.; Nogues, J.; Gedde, U. W., Making flexible magnetic aerogels and stiff magnetic nanopaper using cellulose nanofibrils as templates. *Nat. Nanotechnol.* **2010,** *5* (8), 584-588.

97.		(a) Pekala, R. W.; Farmer, J. C.; Alviso, C. T.; Tran, T. D.; Mayer, S. T.; Miller, J. M.; Dunn, B., Carbon aerogels for electrochemical applications. *J Non-Cryst Solids* **1998,** *225* (1), 74-80; (b) Saliger, R.; Fischer, U.; Herta, C.; Fricke, J., High surface area carbon aerogels for supercapacitors. *J Non-Cryst Solids* **1998,** *225* (1), 81-85; (c) Sun, H.; Xu, Z.; Gao, C., Multifunctional, Ultra-Flyweight, Synergistically Assembled Carbon Aerogels. *Adv. Mater.* **2013,** *25* (18), 2554-2560.

98.		(a) Bag, S.; Arachchige, I. U.; Kanatzidis, M. G., Aerogels from metal chalcogenides and their emerging unique properties. *J. Mater. Chem.* **2008,** *18* (31), 3628-3632; (b) Gaponik, N.; Wolf, A.; Marx, R.; Lesnyak, V.; Schilling, K.; Eychmueller, A., Three-Dimensional Self-Assembly of Thiol-Capped CdTe Nanocrystals: Gels and Aerogels as Building Blocks for Nanotechnology. *Adv. Mater.* **2008,** *20* (22), 4257-4262.

99.		(a) Liu, W.; Herrmann, A.-K.; Geiger, D.; Borchardt, L.; Simon, F.; Kaskel, S.; Gaponik, N.; Eychmueller, A., High-Performance Electrocatalysis on Palladium Aerogels. *Angew. Chem.-Int. Edit.* **2012,** *51* (23), 5743-5747; (b) Herrmann, A.-K.; Formanek, P.; Borchardt, L.; Klose, M.; Giebeler, L.; Eckert, J.; Kaskel, S.; Gaponik, N.; Eychmueller, A., Multimetallic Aerogels by Template-Free Self-Assembly of Au, Ag, Pt, and Pd Nanoparticles. *Chem. Mat.* **2014,** *26* (2), 1074-1083.

100.   (a) Suh, D. J.; Park, T. J.; Lee, S. H.; Kim, K. L., Nickel-alumina composite aerogels as liquid-phase hydrogenation catalysts. *J Non-Cryst Solids* **2001,** *285* (1-3), 309-316; (b) Moreno-Castilla, C.; Maldonado-Hodar, F. J.; Carrasco-Marin, F.; Rodriguez-Castellon, E., Surface characteristics of titania/carbon composite aerogels. *Langmuir* **2002,** *18* (6), 2295-2299; (c) Biener, J.; Baumann, T. F.; Wang, Y.; Nelson, E. J.; Kucheyev, S. O.; Hamza, A. V.; Kemell, M.; Ritala, M.; Leskela, M., Ruthenium/aerogel nanocomposites via atomic layer deposition. *Nanotechnology* **2007,** *18* (5); (d) Leventis, N.; Chandrasekaran, N.; Sadekar, A. G.; Sotiriou-Leventis, C.; Lu, H., One-Pot Synthesis of Interpenetrating Inorganic/Organic Networks of CuO/Resorcinol-Formaldehyde Aerogels: Nanostructured Energetic Materials. *J. Am. Chem. Soc.* **2009,** *131* (13), 4576-+; (e) Shobe, A. M.; Gill, S. K.; Hope-Weeks, L. J., Monolithic CuO-NiO aerogels via an epoxide addition route. *J Non-Cryst Solids* **2010,** *356* (25-27), 1337-1343; (f) Zhang, X.; Liu, J.; Xu, B.; Su, Y.; Luo, Y., Ultralight conducting polymer/carbon nanotube composite aerogels. *Carbon* **2011,** *49* (6), 1884-1893; (g) Davis, M.; Zhang, K.; Wang, S.; Hope-Weeks, L. J., Enhanced electrical conductivity in mesoporous 3D indium-tin oxide materials. *J. Mater. Chem.* **2012,** *22* (38), 20163-20165.

101.   (a) Teichner, S. J.; Nicolaon, G. A.; Vicarini, M. A.; Gardes, G. E. E., Inorganic Oxide Aerogels. *Adv Colloid Interfac* **1976,** *5* (3), 245-273; (b) Schneider, M.; Baiker, A., Aerogels in catalysis *Catal. Rev.-Sci. Eng.* **1995,** *37* (4), 515-556; (c) Schneider, M.; Baiker, A., Titania-based aerogels. *Catal. Today* **1997,** *35* (3), 339-365.

102.   Arnal, P.; Corriu, R. J. P.; Leclercq, D.; Mutin, P. H.; Vioux, A., A solution chemistry study of nonhydrolytic sol-gel routes to titania. *Chem. Mat.* **1997,** *9* (3), 694-698.

103.   Ridge, D.; Todd, M., Studies in the formation mechanisms of alkyl orthosilicates. *Journal of the Chemical Society (Resumed)* **1949,** (0), 2637-2640.

104.   Scherer, G. W.; Smith, D. M., Cavitation during drying of a gel. *J Non-Cryst Solids* **1995,** *189* (3), 197-211.

105.   Garcia-Gonzalez, C. A.; Camino-Rey, M. C.; Alnaief, M.; Zetzl, C.; Smirnova, I., Supercritical drying of aerogels using CO_2: Effect of extraction time on the end material textural properties. *J. Supercrit. Fluids* **2012,** *66*, 297-306.

106.   *Aerogels Handbook*. 1 ed.; Springer New York: 2001.

107.   Gash, A. E.; Tillotson, T. M.; Satcher, J. H.; Hrubesh, L. W.; Simpson, R. L., New sol-gel synthetic route to transition and main-group metal oxide aerogels using inorganic salt precursors. *J Non-Cryst Solids* **2001,** *285* (1-3), 22-28.

108.   Amendola, V.; Meneghetti, M., Laser ablation synthesis in solution and size manipulation of noble metal nanoparticles. *Phys. Chem. Chem. Phys.* **2009,** *11* (20), 3805-3821.

109.   McAllister, M. J.; Li, J.-L.; Adamson, D. H.; Schniepp, H. C.; Abdala, A. A.; Liu, J.; Herrera-Alonso, M.; Milius, D. L.; Car, R.; Prud'homme, R. K.; Aksay, I. A., Single sheet functionalized graphene by oxidation and thermal expansion of graphite. *Chem. Mat.* **2007,** *19* (18), 4396-4404.

110.   Hontorialucas, C.; Lopezpeinado, A. J.; Lopezgonzalez, J. D. D.; Rojascervantes, M. L.; Martinaranda, R. M., Study of oxygen-containing groups in a series of graphite oxides - physical and chemical characterization. *Carbon* **1995,** *33* (11), 1585-1592.

111.   Ganguly, A.; Sharma, S.; Papakonstantinou, P.; Hamilton, J., Probing the Thermal Deoxygenation of Graphene Oxide Using High-Resolution In Situ X-ray-Based Spectroscopies. *J. Phys. Chem. C* **2011,** *115* (34), 17009-17019.

112.   Klell, M., Storage of Hydrogen in the Pure Form. In *Handbook of Hydrogen Storage*, Wiley-VCH Verlag GmbH & Co. KGaA: 2010; pp 1-37.

113.   Kim, H. I.; Moon, G. H.; Monllor-Satoca, D.; Park, Y.; Choi, W., Solar Photoconversion Using Graphene/TiO_2 Composites: Nanographene Shell on TiO_2 Core versus TiO_2 Nanoparticles on Graphene Sheet. *J. Phys. Chem. C* **2012,** *116* (1), 1535-1543.

114.   Yeh, T. F.; Syu, J. M.; Cheng, C.; Chang, T. H.; Teng, H. S., Graphite Oxide as a Photocatalyst for Hydrogen Production from Water. *Adv. Funct. Mater.* **2010,** *20* (14), 2255-2262.

115.   (a) Hummers, W. S.; Offeman, R. E., Preparation of Graphitic Oxide. *J. Am. Chem. Soc.* **1958,** *80* (6), 1339-1339; (b) Marcano, D. C.; Kosynkin, D. V.; Berlin, J. M.; Sinitskii, A.; Sun, Z.; Slesarev, A.; Alemany, L. B.; Lu, W.; Tour, J. M., Improved Synthesis of Graphene Oxide. *ACS Nano* **2010,** *4* (8), 4806-4814.

116.   Junge, H.; Marquet, N.; Kammer, A.; Denurra, S.; Bauer, M.; Wohlrab, S.; Gaertner, F.; Pohl, M.-M.; Spannenberg, A.; Gladiali, S.; Beller, M., Water Oxidation with Molecularly Defined Iridium Complexes: Insights into Homogeneous versus Heterogeneous Catalysis. *Chem.-Eur. J.* **2012,** *18* (40), 12749-12758.

5. TiO$_2$ electrodes applied to hydrogen evolution reaction (HER)

5.1 Scope of this chapter

It is well known that electrochemical reactions are dependent on the morphology and structure of the selected catalytic electrodes. Thus, nanostructuring the electrode coating may enhance the electrochemically active surface area and facilitate the mass transport diffusion inside the three-dimensional porous electrode.[1] Platinum nanoparticles and multilayer reduced graphene oxide solutions can be suspended in a TiO$_2$ lyogel to prepare thin films with improved electrochemical activity. Identifying efficient electrocatalysts for the hydrogen evolution reaction (HER) is fundamental for the development of solar water splitting devices. The choice of the HER catalysts used as coating layers in electrodes can have a crucial influence on the cathode device cost, lifetime and efficiency.

The main objective was to adapt the strategy used in chapter 4 to produce porous thin film electrodes by wet chemical routes and demonstrate the ability of the as-synthesized electrodes to perform the hydrogen evolution reaction (HER). Figure 5.1 illustrates the flexibility and strength of the employed non-hydrolytic sol-gel method to obtain different structural features such as lyogels, xerogels, aerogels and thin films resulting in materials that can be applied either as particle suspension or electrocatalysis. Briefly, the aims can be described as follows: (i) demonstrate that TiO$_2$ lyo-gels loaded with (ii) co-catalysts such as platinum NP and/or (iii) m-rGO can be used to obtain homogeneous coatings on substrates to prepare mesoporous thin films by spin coating followed by annealing treatment and (iv) test the as-synthesized electrodes for HER using standard three-electrode setup[*] for electrocatalytic measurements.

Nowadays the HER catalysts research and development is divided into two categories: a) catalysts employing Pt-group metals and b) non-precious and earth abundant materials such as metal sulfides (MoS$_2$, CoS$_2$, FeCoS$_2$), carbides (Mo$_2$C) and phosphides (Ni$_2$P and CoP). Although many of these materials perform well in the HER,[2,3] the most effective HER electrocalysts are still the Pt-group metals.[4] However, its high price[†] with limited availability restricts its use for large scale H$_2$ production. One approach to overcome these limitations of the platinum catalyst is to increase its surface to bulk atomic ratio in order to lower the amount of metal without compromising the electrolysis efficiency.[5] Additionally, a platinum colloid can be dispersed into a high surface area porous material such as TiO$_2$. It is also possible to combine it with other additives such as conductive

---

[*] Working electrode (cathode), counter electrode (anode) and the reference electrode (reference hydrogen electrode- RHE).

[†] Platinum average price in the year of 2015 was around 38 USD/g according to the Johnson Matthey Plc. Platinum prices and other precious metals are available at: http://www.platinum.matthey.com/prices/price-charts.

carbon layers such m-rGO (as described in the chapters 3 and 4), which are known to facilitate eletrocatalysis.[6]
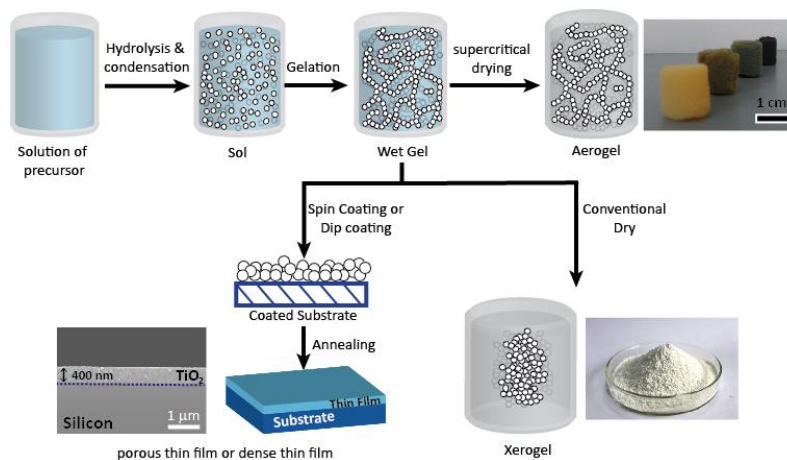

Figure 5.1 Overview of processes and methods involved in the preparation of xerogels, aerogels and thin films.

5.2 Cyclic Voltammetry (CV) and the Rotating Disk Electrode (RDE)

The cyclic voltammetry consists of a time dependent potential applied to an electrochemical cell and it measures the resulting current as a function of that potential. The obtained plot of the current vs. the applied potential is called voltammogram and can provide rather quantitative or qualitative information about chemical species involved in oxidation or reduction reactions.[7] Various different forms of voltammetry have been developed and are well described in the Bard and Falkner textbook.[7] In particular, cyclic voltammetry is one of the most frequently used electrochemical measurement method, where the electrode potential is swept at defined speed (e.g. scan rate) repeatedly back and forth between two defined potentials.

In voltammetry techniques it is common to designate the type of electrode being used as part of the technique name, like in the case of the rotating disk electrode (RDE) voltammetry. In this technique, the rotation rate is held constant as the electrode is swept from one potential to another potential at a constant scan rate. Moreover, in electrochemical measurements it is a common practice to sweep the potential to at least 200 mV on either side of the standard electrode potential, and rotation rates are usually between 100 rpm and 2400 rpm. The theory describing the RDE was developed by V. G. Levich and consists of a forced convection method to assist the chemical species (analyte) to reach the electrode.[8] The rotation of the electrode disk drags the electrolyte (analyte) to the electrode surface where it can react, as far as the rotation speed is kept within the limits that laminar flow is maintained. Thus, even though the analyte reaches the electrode surface by a combination of convection and diffusion, it is the latter vehicle–diffusion that ultimately determines the current observed at the electrode. For practical reasons if we perform a RDE voltammetry for a simple and reversible half-reaction (such as the proton reduction, eq. 5.1), then the shapes of the

mass-transport controlled voltammograms will resemble a sigmoidal curve independent of the rotation rate as illustrated in Fig.5.2a. A typical arrangement for a RDE voltammetric electrochemical cell is composed by the working electrode (WE), the reference electrode (RE), and the counter electrode (CE) that are connected to a potentiostat, additionally the cell also includes a N_2-purge line for removing dissolved O_2, as illustrated in Fig.5.2b.
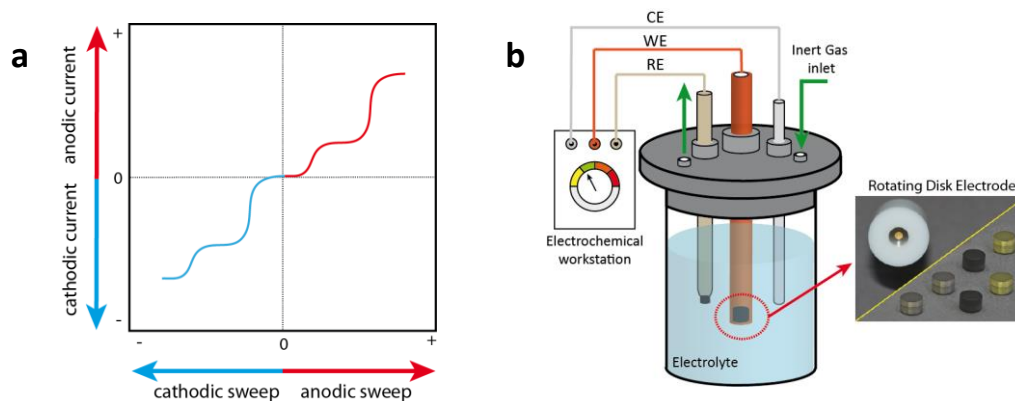
Figure 5.2 Typical rotating disk electrode voltammogram obtained after applying cyclic potential sweep (a). Scheme of the electrochemical RDE voltammogram setup used to obtain the current density as a function of the applied potential (b).

5.3 Platinum group and non-precious abundant metals applied in electrocatalysis

The fundamental step in water splitting is the hydrogen evolution reaction, i.e. the reduction of two protons to generate one hydrogen molecule as illustrated in equation 5.1 below. This reaction presents a thermodynamic potential of 0 V vs. the standard hydrogen electrode (SHE).

$$\text{Reduction:} \qquad 2\,H^+ \; + \; 2\,e^- \longrightarrow H_2 \qquad\qquad (5.1)$$
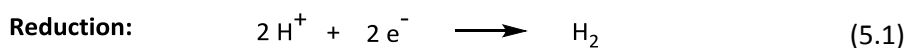
The reaction above can occur without catalyst but needs high overpotentials (η) to achieve a significant hydrogen rate production. The overpotential represents the voltage in excess of the thermodynamic voltage, required to overcome the losses in the cell and obtain the desired output in terms of current density or amount of hydrogen from the cell. Slow electrode/electrolyte reactions and large resistive losses necessitate high overpotentials.[9] Therefore, to lower the overpotential and consequently improve the energy efficiency one must develop active HER catalysts. In general, the developed catalysts or the cathode can be employed under acidic or neutral conditions and the platinum group metals are the best catalysts for this specific reaction until now,[4] because they are able to generate high current densities at low overpotentials. However the platinum metal group is limited by their availability and their elevated prices, which makes large scale applications impracticable. As a result a steady growing number of catalysts based on non-precious and abundant metals have been developed in particular with respect to three classes of materials: sulfides (MoS_2)[3, 6, 10] carbides (Mo_2C)[11,12] and phosphides (Ni_2P, NiP_2, $NiPSe$)[13,14,15]. Among all these new HER

95

heterogeneous catalysts based on abundant and non-precious metals the highest current densities are achieved by MoS_2 reaching approx. 8 mA cm^{-2} at an overpotential of 0.1 V (vs. RHE).[3,10c,16] One very innovative approach was reported by Chen et al. where was developed a low cost HER catalyst based on a platinum atomic monolayer deposited onto tungsten carbide. The Pt atomic monolayer is a good method to increase the surface to bulk atomic ratio of platinum allowing in this way a much lower metal loading without compromising the electrocatalytic efficiency. By using this approach it was possible to mimic current densities of bulk platinum using a greatly reduced amount of platinum in the electrocatalysis tests.[5]

5.4 TiO₂ mesoporous thin films loaded with co-catalyst and additives and their application as electrodes in HER

Using Fig. 5.1 as a guideline, three kinds of TiO_2 thin films were produced using this approach: i) pure TiO_2 as control; ii) TiO_2 loaded with 1 wt. % of platinum particles with a size distribution between 2-3 nm (labelled as 1.0-Pt/TiO₂) and iii) TiO_2 loaded with 1 wt.% of platinum particles and additional 2 wt. % of m-rGO (labelled as 1.0-Pt/TiO₂/m-rGO). The viscous titania wet gel resulting from the gelation process is suitable to be applied as a coating material onto several substrates such as glass, transparent conductive oxides, silicon and polished titanium metal plates. Glass substrates are used as non-conductive supports to evaluate the coating conductivity, whereas ITO and silicon substrates are good to analyse the morphology and thickness of the deposited layer(s) using scanning electron microscopy. The polished titanium substrate is corrosion resistant and can be used as a cathode in an electrochemical cell. We will employ a lyo-gel comprised of TiO_2, platinum particles and m-rGO sheets (i.e. as viscous solution) to fabricate coated layers. The functional and morphological characterization of these components were already presented in the previous chapter and will be not repeated here. Briefly, the preformed TiO_2 particles consist of single phase anatase (Fig. 4.8a) and has diameters of nearly 3 nm (Fig. 4.9a, b). Metallic platinum particles with sizes ranging between 1-2 nm (Fig. 4.9c, d and Fig. 4.11). The multilayer carbom material (m-rGO) showed a graphitic sheet within 2-4 microns as suggested by TEM and AFM. This multilayer material is composed of approx. of 90% carbon and 10% oxygen identified mainly as C-C sp^2, C-O and C=O bonds, as revelead by elemental analysis and XPS. The graphitic material was arranged in a stack between 3-20 layers measured by AFM and TEM. Fig. 5.3a shows the top view of pure TiO_2 with uniform coating and porous superficial structure deposited onto a silicon wafer. At higher magnification the porous structure is more evident and pores of nearly 10 nm are observed. The cross section of this material is shown in Fig. 5.4a. A thickness of 400 nm was determined with the aid of a digital software (ImageJ). A higher magnification of the cross section reveals the uniformity of the film (Fig. 5.4b).
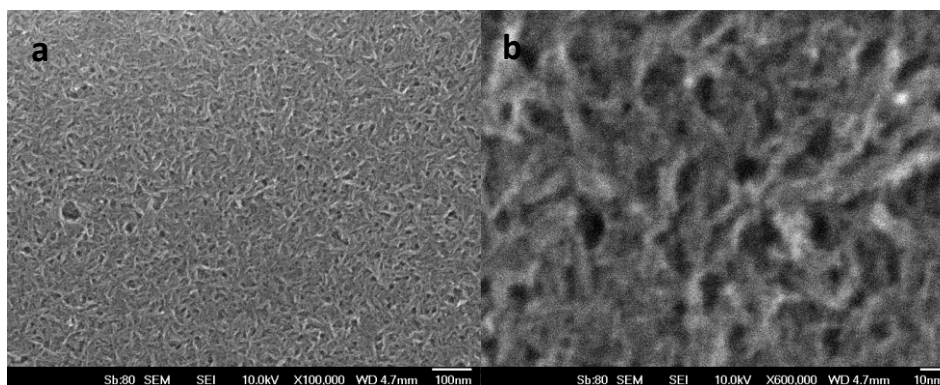
Figure 5.3 SEM top view from the bare TiO$_2$ thin film, scale bar = 100 nm (a) and with higher magnification displaying the superficial porous structure of the deposited film, scale bar = 10 nm (b).
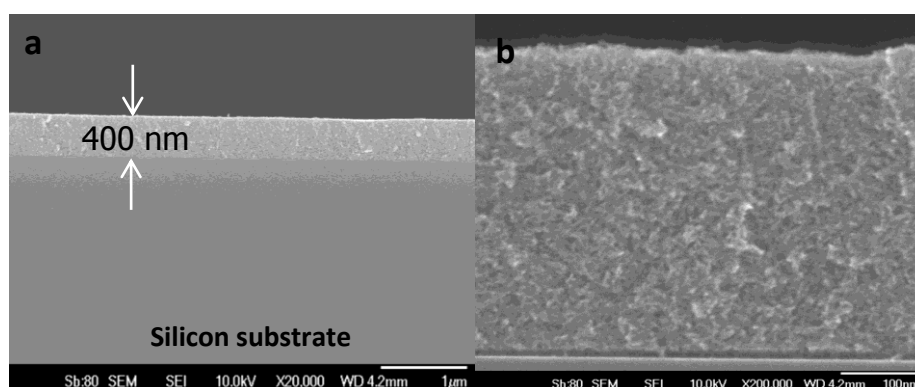
Figure 5.4 SEM cross section from bare TiO$_2$ showing a 400 nm film thickness, scale bar = 1 micron (a) and higher magnification displaying the deposited mesoporous film, scale bar = 100 nm (b).

The same features that were observed with the pure TiO$_2$ can also be observed with the TiO$_2$ loaded with platinum particles with the exception of a few white regions that can be seen in Fig. 5.5a, which are platinum particle agglomerates larger than 100 nm located on the surface of the titania coating. Fig. 5.5b reveals morphology that is similar as pure TiO$_2$ without agglomerated platinum particles.
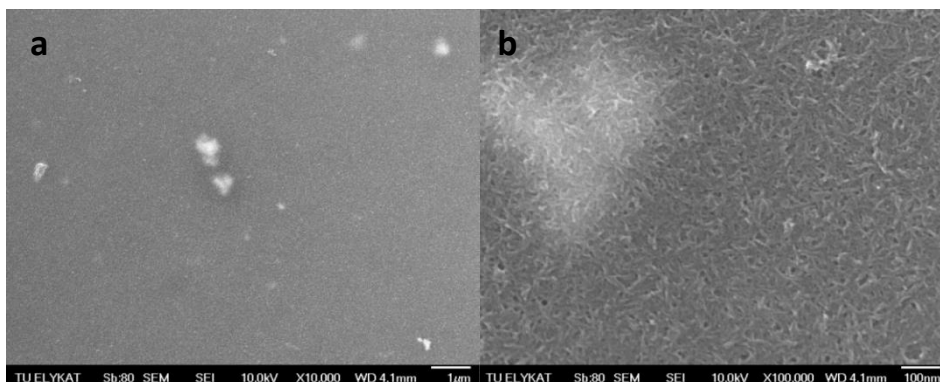
Figure 5.5 (a) SEM top view from the TiO$_2$ loaded with platinum particles (1 wt. %) thin film and (b) higher magnification displaying porous structure of the deposited film.

However, TiO_2 loaded with platinum (1 wt. %) and multilayer reduced graphene oxide had a completely different morphology in comparison with the last two compositions. A general top view is shown in Fig. 5.6a and considerable amount of inhomogeneity is detected as a result of agglomerates of m-rGO larger than 10 μm. A closer look in one of these agglomerates revealed the m-rGO structure embedded in the TiO_2 deposited layer, as shown in Fig. 5.6b. A more detailed magnification reveals a TiO_2 morphology that still resembles the pristine titania material as shown in Fig. 5.6c.
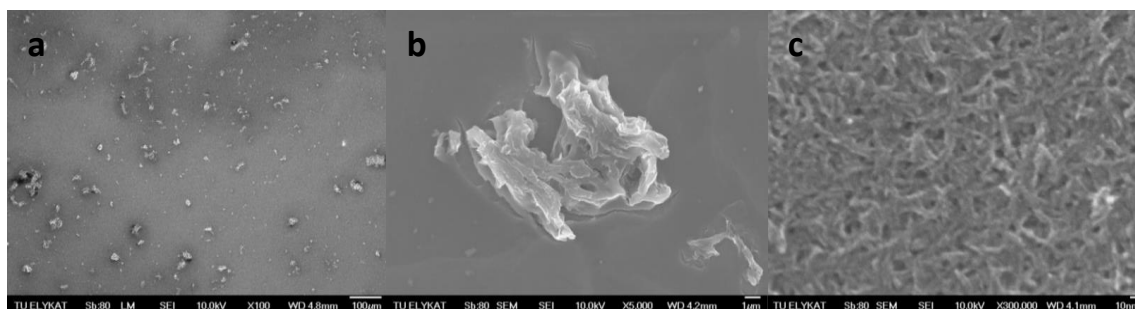
Figure 5.6 (a) SEM top overview from the TiO_2 loaded with platinum particles (1 wt. %) and also with m-rGO (10 wt. %) thin film, (b) top view of a m-rGO aggregate embedded in the thin film layer, (c) higher magnification displaying the porous structure of the as deposited film.

The hydrogen half-reaction as represented by the eq. 5.1 (HER) was submitted to an electrochemical potential to measure the generated current densities for several prepared electrodes. Electrodes with the following compositions: (i) 1.0-Pt/TiO₂ and (ii) 1.0-Pt/TiO₂/m-rGO were tested and compared with a commercial benchmark material composed of 10 % platinum impregnated in carbon vulcan (i.e. 10 wt. % platinum particles supported on conductive carbon). The nanostructured films were measured using a standard three-electrode setup in 0.5 M H_2SO_4 as illustrated in Fig. 5.2b and further details are given in the experimental section. All data were *i*R corrected and the ohmic losses oscillated between 5.3 and 5.7 Ω for the 1.0-Pt/TiO₂ sample and between 3.3 and 3.7 Ω for the 1.0-Pt/TiO₂/m-rGO material. The cyclic voltammetry curves, as shown in Fig. 5.7a exhibit the overpotentials necessary for the deposited layer materials to achieve a certain catalytic current density (vs. reversible hydrogen potential (RHE)). The standard material, Pt/vulcan, displayed a density current of approx. 8 mA cm^{-2} at 0.05 V (vs. RHE) which is considered a high activity value whereas the titania electrodes showed negligible density currents after two cycles. The long term stability of the electrodes was measured and the result after performing 50 cycles is displayed in Fig. 5.7b. Therefore, a comparison between both titania electrodes resulted in 40% higher density current for 1.0-Pt/TiO₂/m-rGO in relation to 1.0-Pt/TiO₂ after two cycles and the 1.0-Pt/TiO₂/m-rGO presented a slight deactivation after 50 cycles as shown in Fig. 5.7b. This result might indicate that the platinum particles are not well distributed over the titania electrodes as depicted in Fig 5.5a or that they can not be accessed by the electrolyte during the HER measurement. Moreover,

some sort of contamination such as the organic solvent used to suspend the platinum particles, chloride or byproduct from the reaction between $HPtCl_6$ with benzyl alcohol to produce the Pt NP[‡] might be hindering the platinum and m-rGO sites.
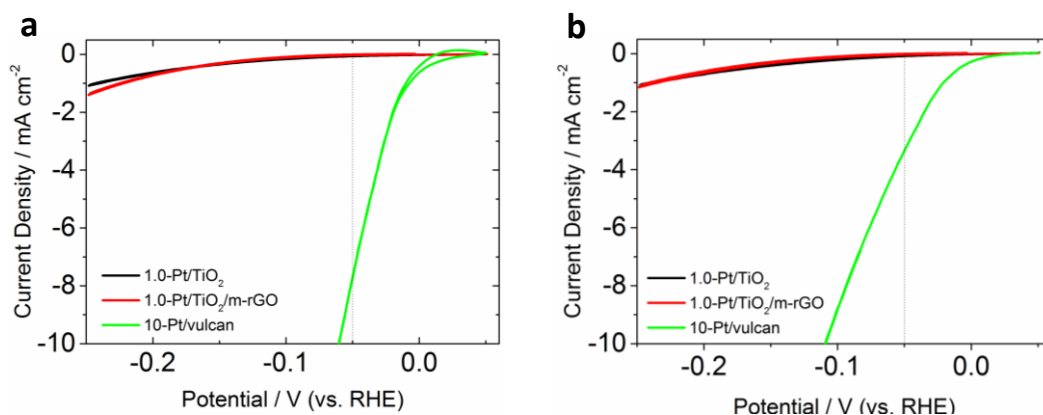
Figure 5.7 Electrochemical characterization of 1.0-Pt/TiO₂ and 1.0-Pt/TiO₂/m-rGO compared to 10-Pt/Vulcan benchmark material. (a) Cyclic voltammetry curve after 2 cycles in HER region and (b) after 50 cycles.

An additional electrochemical characterization was performed after submitting the electrodes to cyclic voltammetry under oxidizing conditions or after applying electrochemically active surface area (ECSA). The ECSA procedure cleans the platinum surface from contaminants and carbon deposits facilitating in this manner the access to the catalytic sites by electrooxidation. Fig. 5.8a shows the significant improvement of the density current obtained with the titania electrodes of approx. 0.2 and 0.5 mA cm^{-2} at 0.05 V (vs. RHE) while the density current obtained with the benchmark material is slighted reduced to 6 mA cm^{-2}. At overpotentials of 0.2 V (vs. RHE) current densities of approx. 2 mA cm^{-2} for 1.0-Pt/TiO₂ and 6 mA cm^{-2} for 1.0-Pt/TiO₂/m-rGO are observed. Long term stability measurement revealed deactivation of all electrodes under investigation after 50 cycles. Fig. 5.8b displays the current densities of 0.15, 0.3 and 3 mA cm^{-2} at 0.05 V overpotential for 1.0-Pt/TiO₂, 1.0-Pt/TiO₂/m-rGO and Pt/Vulcan respectively. At 0.2 V overpotential the 1.0-Pt/TiO₂/m-rGO is nearly 3 times more active than 1.0-Pt/TiO₂, which illustrates nicely the electron collector-transport effect of the conductive m-rGO material. All measurements indicate that the activity is mainly influenced by the concentration of platinum and how well distributed it is over the entire electrode surface.

[‡] Note that: The platinum colloidal solution was loaded into the lyogel without previous washing or purification.
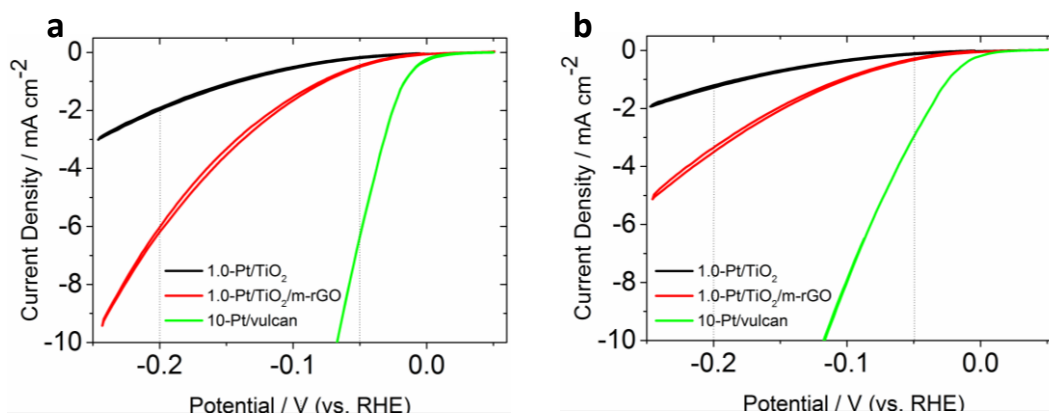
Figure 5.8 Electrochemical characterization of Pt/TiO₂ and Pt/TiO₂/m-rGO compared to Pt/Vulcan benchmark material after applying electrochemically active surface area (ECSA) or after oxidizing conditions. (a) Cyclic voltammetry curve after 2 cycles in HER region and (b) after 50 cycles (b).

5.5 Conclusions

In summary, we have used the non-hydrolitic sol-gel method for the preparation of thin films of TiO₂ that can be used as electrodes for hydrogen evolution. The method is highly flexible and allows the incorporation of co-catalysts, such as Pt nanoparticles and reduced graphene oxide. In spite of this, the performance of the electrodes in hydrogen generation was below the standard material used as benchmark. Important aspects were the following: i) contamination is an issue that affects the catalytic performance for instance of the platinum nanoparticles. A clear indication for this was the fact that oxidizing conditions significantly improved the density currents by approx. 200% and 600% at 0.2 V (vs. RHE) for 1.0-Pt/TiO₂ and 1.0-Pt/TiO₂/m-rGO respectively; ii) Addition of m-rGO is beneficial for increasing the density current by nearly 3 times, and iii) the Pt nanoparticle concentration of 1 wt.% was not enough to reach a high density current as displayed by the standard Pt-vulcan material.

5.6 Experimental Section

5.6.1 Experimental and characterization

All electrocatalytic testing was performed by using a three-electrode rotating disc setup using a RHE (Gaskatel, HydroFlex) as a reference and Pt gauze (Chempur, 1024 mesh cm⁻², 0.06 mm wire diameter, 99.9%) as a counter electrode. All potentials in this work are referenced to the reversible hydrogen electrode. Small discs with a diameter of 6 mm were pierced out from the coated substrates. These homogeneously coated discs were mounted on a rotating disk shaft and served as a working electrode (n = 2000 rpm) using 0.5 M H₂SO₄ as the supporting electrolyte (Fixanal, Fluka Analytical) and a BioLogic SP-200 as the potentiostat. The electrolyte solution was purged for at least 30 minutes with nitrogen before the catalytic tests. The activity in the hydrogen evolution reaction was investigated by cyclic voltammetry in a potential window of 50 to -210 mV vs. RHE with a scan

rate of 20 mV s^{-1}. Impedance spectroscopy was measured to correct the ohmic losses. The reference catalyst was prepared by dissolving 5 mg of Pt/Vulcan (10wt %) in 3.98 ml of water. 20 µl of Nafion solution (5%) was carefully added. After addition of 1 ml of isopropanol the mixture was sonicated for 15 min with 6 W output power with a Branson sonic bath. The resulting ink was immediately employed for film deposition via drop-casting and subsequent drying at 60 °C. The resulting reference catalyst film had a geometric Pt loading of 1 ng/mm². SEM images were recorded on a JEOL 7401F instrument operating at 10 kV.

5.6.2 Synthesis of trizma-functionalized TiO₂

The synthesis of the TiO₂ used in the substrate coating it is described in the section 4.8.1.1 in chapter 4.

5.6.3 Synthesis of the platinum nanoparticles

The synthesis of the platinum colloid solution loaded into the TiO₂ lyo-gel it is described in the section 4.8.1.2 in chapter 4.

5.6.4 Synthesis of multilayer reduced graphene oxide (m-rGO)

The synthesis of the m-rGO colloid solution loaded into the TiO₂ lyo-gel it is described in the section 4.8.1.4 in chapter 4.

5.6.5 Preparation of the 1.0 Pt/TiO₂ and 0.1 Pt/TiO₂/m-rGO

For the preparation of 1 wt. % platinum in TiO₂ (1.0 Pt/TiO₂), it was used 178.2 mg of functionalized TiO₂ and 1.9 mL of the as synthesized platinum NP stock solution with concentration determined by ICP [0.935 mg/mL]. The fine TiO₂ powder was first suspended in 4 mL of deionized water and stirred to obtain an homogeneous particle suspension, followed by the addition of 1.9 mL of Pt NP stock solution. The 1.0 Pt/TiO₂ particle suspension was also stirred to obtain homogenous mixture. For the case of 0.1 Pt/TiO₂/m-rGO the same procedure was performed. 174.6 mg of functionalized TiO₂ and 1.9 mL of the Pt NP and 3.6 mg of m-rGO were used. First a homogeneous mixture between TiO₂ and Pt NPs is obtained as described above, followed by the addition of 3.6 mg of the m-rGO and stirred until a homogeneous particle suspension was achieved. Finally, both particle suspensions were placed in pre-heated oven and heated at 90°C for 5-10 minutes until the viscosity was increased.

5.6.6 Thin film deposition and processing

After a viscous suspension was obtained for both desired compositions the thin film deposition process was performed. For the deposition of a substrate with surface area of approx. 1 cm^2, 300 µl of the viscous suspension mentioned above were used for each composition (1.0-Pt/TiO$_2$ and 1.0-Pt/TiO$_2$/m-rGO). The thin film deposition process is based on the following: the substrate (glass, ITO, silicon or titanium) is placed in the spin coater, rinsed with clean ethanol and rotated for 10 seconds at 3500 rpm speed. Then, 300 microliters of the viscous solution is spread above the substrate surface. A period of 30 seconds is awaited to cover the whole flat surface of the substrate, then the spin coating process is started. The spin parameter is the following: 3500 rpm speed for 20 seconds. Finally, the deposited thin films are placed in a ceramic vessel and inserted into a pre-heated quartz tube at 400°C under argon flow for 20 minutes. After 20 minutes the oven is turned off and the thin films are removed when the oven is close to room temperature.

5.7 References

1.   Menzel, N.; Ortel, E.; Kraehnert, R.; Strasser, P., Electrocatalysis Using Porous Nanostructured Materials. *ChemPhysChem* **2012,** *13* (6), 1385-1394.

2.   Faber, M. S.; Jin, S., Earth-abundant inorganic electrocatalysts and their nanostructures for energy conversion applications. *Energy Environ. Sci.* **2014,** *7* (11), 3519-3542.

3.   Morales-Guio, C. G.; Hu, X., Amorphous Molybdenum Sulfides as Hydrogen Evolution Catalysts. *Accounts Chem. Res.* **2014,** *47* (8), 2671-2681.

4.   Trasatti, S., Work function, electronegativity, and electrochemical behaviour of metals: III. Electrolytic hydrogen evolution in acid solutions. *Journal of Electroanalytical Chemistry and Interfacial Electrochemistry* **1972,** *39* (1), 163-184.

5.   Esposito, D. V.; Hunt, S. T.; Stottlemyer, A. L.; Dobson, K. D.; McCandless, B. E.; Birkmire, R. W.; Chen, J. G., Low-Cost Hydrogen-Evolution Catalysts Based on Monolayer Platinum on Tungsten Monocarbide Substrates. *Angewandte Chemie* **2010,** *122* (51), 10055-10058.

6.   Li, Y.; Wang, H.; Xie, L.; Liang, Y.; Hong, G.; Dai, H., MoS$_2$ Nanoparticles Grown on Graphene: An Advanced Catalyst for the Hydrogen Evolution Reaction. *J. Am. Chem. Soc.* **2011,** *133* (19), 7296-7299.

7.   Allen J. Bard; Larry R. Faulkner, *Electrochemical Methods: Fundamentals and Applications , Second Edition* John Wiley & Sons, New York (2000)

8.   Levich, V. G., *Physicochemical Hydrodynamics*. Prentice-Hall, Upper Saddle River NJ (1962).

9.   Grimes, C.; Varghese, O.; Ranjan, S., Hydrogen Generation by Water Splitting. In *Light, Water, Hydrogen*, Grimes, C.; Varghese, O.; Ranjan, S., Eds. Springer US: 2008; pp 35-113.

10.   (a) Jaegermann, W.; Tributsch, H., Interfacial properties of semiconducting transition metal chalcogenides. *Progress in Surface Science* **1988,** *29* (1–2), 1-167; (b) Hinnemann, B.; Moses, P. G.; Bonde, J.; Jørgensen, K. P.; Nielsen, J. H.; Horch, S.; Chorkendorff, I.; Nørskov, J. K., Biomimetic Hydrogen Evolution: MoS$_2$ Nanoparticles as Catalyst for Hydrogen Evolution. *J. Am. Chem. Soc.* **2005,** *127* (15), 5308-5309; (c) Jaramillo, T. F.; Jørgensen, K. P.; Bonde, J.; Nielsen, J. H.; Horch, S.; Chorkendorff, I., Identification of Active Edge Sites for Electrochemical H$_2$ Evolution from MoS$_2$ Nanocatalysts. *Science* **2007,** *317* (5834), 100-102.

11.   Vrubel, H.; Hu, X., Molybdenum Boride and Carbide Catalyze Hydrogen Evolution in both Acidic and Basic Solutions. *Angewandte Chemie International Edition* **2012,** *51* (51), 12703-12706.

12.   Chen, W. F.; Wang, C. H.; Sasaki, K.; Marinkovic, N.; Xu, W.; Muckerman, J. T.; Zhu, Y.; Adzic, R. R., Highly active and durable nanostructured molybdenum carbide electrocatalysts for hydrogen production. *Energy Environ. Sci.* **2013,** *6* (3), 943-951.

13.   Zhuo, J.; Cabán-Acevedo, M.; Liang, H.; Samad, L.; Ding, Q.; Fu, Y.; Li, M.; Jin, S., High-Performance Electrocatalysis for Hydrogen Evolution Reaction Using Se-Doped Pyrite-Phase Nickel Diphosphide Nanostructures. *ACS Catalysis* **2015,** *5* (11), 6355-6361.

14.   Feng, L.; Vrubel, H.; Bensimon, M.; Hu, X., Easily-prepared dinickel phosphide (Ni₂P) nanoparticles as an efficient and robust electrocatalyst for hydrogen evolution. *Phys. Chem. Chem. Phys.* **2014,** *16* (13), 5917-5921.

15.   Popczun, E. J.; McKone, J. R.; Read, C. G.; Biacchi, A. J.; Wiltrout, A. M.; Lewis, N. S.; Schaak, R. E., Nanostructured Nickel Phosphide as an Electrocatalyst for the Hydrogen Evolution Reaction. *J. Am. Chem. Soc.* **2013,** *135* (25), 9267-9270.

16.   Vesborg, P. C. K.; Seger, B.; Chorkendorff, I., Recent Development in Hydrogen Evolution Reaction Catalysts and Their Practical Implementation. *The Journal of Physical Chemistry Letters* **2015,** *6* (6), 951-957.

6.   Summary and Outlook

In summary, it was demonstrated that graphene (e.g. multilayer reduced graphene oxide with few μm^2 area and with ca. 3-16 layers thickness) can be employed to enhance the hydrogen evolution reaction (HER). However, its effectiveness is case sensitive and dependent on the physical configuration and spatial arrangement between the photocatalyst components.

First, it was shown in chapter 3 that the obtained semiconductor ($NaTaO_3$) particle sizes in the range of 20- 25 nm were essential to achieve optimum physical contact between all components. In contrast, the same semiconductor produced by solid state reaction exhibited crystallite sizes similar to the multilayer graphene sizes in the range of a few microns, which restricted their physical contact. This demonstrated that the photocatalyst components such as the semiconductor, co-catalyst and the multilayer graphene even suspended in aqueous solution are in intimate physical contact. In this way, the graphene based material assisted the photocatalytic reaction as an electron collector and transporter, in addition to acting as an additional active surface for the hydrogen evolution reaction (HER).

The concept of using graphene based materials to promote high charge mobility was transferred to the multicomponent aerogel approach in order to take advantage of the co-catalyst and multilayer graphene embedded into a semiconductor with a high surface area, as described in chapter 4. Several crystalline mesoporous multicomponent aerogels were successfully obtained. However, a significant photoactivity loss was observed for the multicomponent aerogel loaded with multilayer reduced graphene oxide (m-rGO) due to two reasons: (i) the physical separation between the TiO_2 catalyst and the m-rGO sheets when the aerogel is suspended in aqueous solution, which prevented the electron transfer from the semiconductor to the electron collector and transporter (i.e. m-rGO); (ii) it was observed an enrichment of Pt nanoparticles adsorbed on the m-rGO sheets at the cost of a lower loading of the Pt nanoparticles on the TiO_2, resulting in a less effective co-catalyst loading over the TiO_2 semiconductor.

Finally in chapter 5, in addition to employing the gels to produce the aforementioned multicomponent aerogels we demonstrated that lyo-gels can also be used as coating layers to prepare xerogel thin film electrodes. The electrodes were tested for the hydrogen evolution reaction, which resulted in enhanced performance for the electrodes loaded with the multilayer reduced graphene oxide in comparison to films containing only Pt and TiO_2. Therefore, we proved that the fixation of the multicomponent aerogel as a xerogel electrode enhanced the performance of the HER, by providing more intimate physical contact between all the components deposited over the electrode, in comparison to electrodes containing only Pt and TiO_2.

The multicomponent aerogel architecture proved to be a versatile material as heterogeneous catalyst or electrocatalyst for the hydrogen evolution reaction. As further steps it would be useful to

extend the aerogel concept beyond TiO_2 compositions by obtaining semiconductor-semiconductor heterojunctions such as TiO_2/Cu_2O, $TiO_2/SrTiO_3$ and TiO_2/CdS. The addition of heterostructures and/or novel semiconductor phases would enhance the sun light absorption, which is currently limited to the UV region. Moreover, considering the several functional groups present in the chemically produced graphene, it would be feasible to functionalize the multilayer graphene with sensitizers such as organic dyes or inorganic quantum dots in order to enhance the sun light absorption and increase the catalytic efficiency.